Nuclear Instruments and Methods in Physics Research A275 (1989) 1–48
North-Holland, Amsterdam

ARGUS: A UNIVERSAL DETECTOR AT DORIS II

The ARGUS Collaboration

H. ALBRECHT, U. BINDER [1], P. BÖCKMANN, G. DREWS, R. GLÄSER, G. HARDER, H. HASEMANN, A. KROLZIG [2], E. MICHEL, W. REINSCH, W. SCHMIDT-PARZEFALL, H. SCHRÖDER, H.D. SCHULZ, F. SELONKE, E. STEINMANN [3] and R. WURTH

DESY, Hamburg, FRG

A. DRESCHER, B. GRÄWE [4], W. HOFMANN [5], D. KAMP, A. MARKEES [6], U. MATTHIESEN, H. SCHECK, B. SPAAN, J. SPENGLER [7] and D. WEGENER

Institut für Physik, Universität Dortmund [8], FRG

R. HELLER [9], K.R. SCHUBERT [10], J. STIEWE, K. STRAHL, R. WALDI and S. WESELER [11]

Institut für Hochenergiephysik, Universität Heidelberg [8], FRG

K.W. EDWARDS [12], W.R. FRISKEN [13], Ch. FUKUNAGA [14], D.J. GILKINSON [15], D.M. GINGRICH [16], M. GODDARD [13], H. KAPITZA [12], P.C.H. KIM [17], R. KUTSCHKE [18], D.B. MacFARLANE [15], J.A. McKENNA [19], K.W. McLEAN [15], A.W. NILSSON [15], R.S. ORR [18], B.P. PADLEY [20], P.M. PATEL [15], J.D. PRENTICE [18], H.C.J. SEYWERD [21], J.D. SWAIN [18], G. TSIPOLITIS [15], T.S. YOON [18] and J.C. YUN [22]

Institute of Particle Physics [23], Canada

R. AMMAR, D. COPPAGE, R. DAVIS, S. KANEKAL and N. KWAK

University of Kansas [24], Lawrence, KS, USA

L. JÖNSSON

Institute of Physics, University of Lund [25], Sweden

A. AREFIEV, A. BABAEV, M. DANILOV, A. GOLUTVIN, V. LUBIMOV, V. MATVEEV, V. NAGOVITSIN, V. RYLTSOV, A. SEMENOV, Yu. SEMENOV, V. SHEVCHENKO, V. SOLOSHENKO, V. TCHISTILIN, I. TICHOMIROV and Yu. ZAITSEV

[1] Now at CERN, Geneva, Switzerland.
[2] Deceased.
[3] Now at Bundeswehr, Kiel, FRG.
[4] Now at Hösch AG, Dortmund, FRG.
[5] Now at University of California, Berkeley, CA, USA.
[6] Now at Swiss Administration, Bern, Switzerland.
[7] Now at DESY, Hamburg, FRG.
[8] Supported by the Bundesministerium für Forschung und Technologie, FRG.
[9] Now at Kernforschungszentrum Karlsruhe, FRG.
[10] Now at Institut für Experimentelle Kernphysik, Universität Karlsruhe, FRG.
[11] Now at University of California, Santa Cruz, CA, USA.
[12] Carleton University, Ottawa, Ontario, Canada.
[13] York University, Downsview, Ontario, Canada.
[14] Now at University of Tokyo, Japan.
[15] McGill University, Montreal, Quebec, Canada.
[16] Now at University of Oxford, UK.
[17] Now at SLAC, Stanford University, CA, USA.
[18] University of Toronto, Ontario, Canada.
[19] Now at California Institute of Technology, Pasadena, CA, USA.
[20] Now at TRIUMF, Vancouver, BC, Canada.
[21] Now at Universität Siegen, FRG.
[22] Now at FNAL, Batavia, IL, USA.
[23] Supported by the Natural Sciences and Engineering Research Council, Canada.
[24] Supported by the US National Science Foundation.
[25] Supported by the Swedish Research Council.

0168-9002/89/$03.50

Institute of Theoretical and Experimental Physics, Moscow, USSR

R. CHILDERS, C.W. DARDEN, H. GENNOW and Y. OKU [26]

University of South Carolina [27], Columbia, SC, USA

Received 25 July 1988

The detector ARGUS has been designed as a universal tool to investigate final states from e^+e^- annihilation processes in the energy range of the Υ resonances. ARGUS started operation in October 1982 and has since successfully taken data at the $\Upsilon(1S)$, $\Upsilon(2S)$ and $\Upsilon(4S)$ energies, and in the nearby continuum. The detector combines excellent charged particle identification and good photon energy resolution over more than 90% of the full solid angle. A particle originating from the interaction vertex and leaving the beam tube traverses the following components: the vertex drift chamber, the main drift chamber which determines its momentum and specific ionization, the time-of-flight system through which its velocity is determined, and the electromagnetic calorimeter. Muons pass through the magnet coils and the flux return yoke and finally hit the muon chamber system which surrounds the detector. The momentum resolution of ARGUS is $\sigma(p_T)/p_T = (0.01^2 + (0.009 p_T[\mathrm{GeV}/c])^2)^{1/2}$, and the photon energy resolution in the barrel shower counters is $\sigma(E)/E = (0.072^2 + 0.065^2/E[\mathrm{GeV}])^{1/2}$. Combining the information from all particle identification devices, more than 80% of all charged hadrons can be recognized unambiguously. The electron–hadron and muon–hadron rejection rates are 1 : 200 and 1 · 50 respectively.

1. Introduction

This paper describes the magnetic detector ARGUS, installed at the storage ring DORIS II at DESY, and operating since October 1982. The detector was designed as a universal tool to analyse final states from electron positron annihilations in the energy range of the Υ resonances. The investigation of decays of B mesons produced from the $\Upsilon(4S)$ resonance was expected to be a major analysis topic. The reconstruction of these high multiplicity decays is faced with serious combinatorial background problems unless one knows the identity of the decay particles. Hence ARGUS was optimized for charged particle identification.

Charged hadrons can be identified both by the measurement of the specific ionization in the main drift chamber and by the measurement of the velocity in the time-of-flight system. The momentum measurement performed using the drift chamber is supported by the improved vertex reconstruction capability of the vertex drift chamber. Electrons from certain momentum regions can be identified with the drift chamber and, at momenta lower than 230 MeV/c, also by the time-of-flight system. The discrimination between electrons and hadrons is performed mainly by the shower counter system, which is mounted inside the magnet coil. This also allows photons with energies as low as 50 MeV to be measured. Muons are identified by the muon chamber system which covers the detector in three layers. The magnet coils, the flux return yoke, and the shower counters serve as hadron absorbers.

[26] Now at Deutsche Forschungs- und Versuchsanstalt für Luft- und Raumfahrt, Oberpfaffenhofen, FRG.

[27] Supported by the US Department of Energy, under contract DE-AS09-80ER10690.

The paper is organized as follows: section 2 will review the criteria which were used to define boundary conditions for the design of ARGUS. Section 3 describes the detector components in detail. Section 4 is devoted to the ARGUS trigger system. The on line data acquisition is described in section 5. Section 6 will sketch the off line data analysis scheme. Finally, we will summarize our experience with ARGUS in the first four years of operation, and demonstrate the interplay of detector capabilities and the physics results achieved so far.

2. Design criteria

ARGUS has been designed as a universal tool for research work in the energy range of the Υ resonances, at centre of mass energies around 10 GeV [1]. In this energy range one encounters a variety of physical phenomena:

(1) Direct Υ decays as well as transitions between different S- and P-states allow for the determination of fundamental parameters of QCD. Three gluon decays of the Υ resonances lead to events with a nearly isotropic structure.

(2) Quark–antiquark production in the continuum underlying the Υ resonances gives rise to two-jet events. Jets from primary charmed quarks are of particular interest. New charmed states and new decay modes of charmed particles can be measured. Efficient reconstruction of charmed mesons and baryons is, therefore, an important requirement.

(3) Crossing the open beauty threshold at the $\Upsilon(4S)$, one is faced with the new physics of B meson decays. Fundamental weak interaction parameters can be measured. Among these are the ratio of the

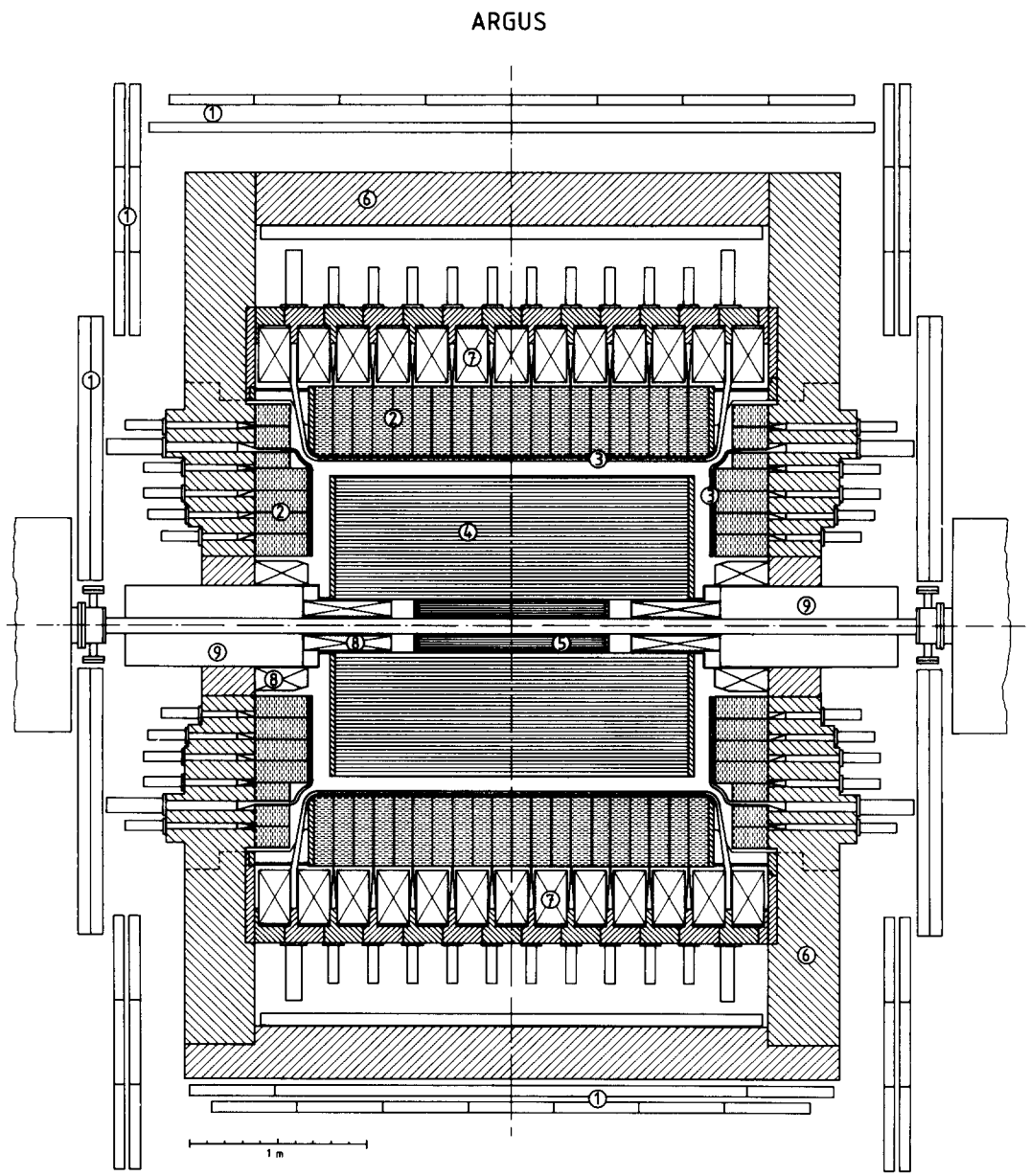

Fig. 1. Section through the detector ARGUS parallel to the beam axis. 1: Muon chambers; 2: shower counters; 3: TOF counters; 4: drift chamber; 5: vertex chamber; 6: iron yoke; 7: solenoid coils; 8: compensation coils; 9: mini-β-quadrupole.

decay rates of the b quark to u and c quarks and the degree of B^0–$\bar{B}^0$ mixing. For such investigations the identification of leptons over a large momentum range is mandatory.

(4) The above requirement holds for studies of τ leptons, which are copiously produced and easily tagged at energies around 10 GeV. New τ decay modes and an improvement of the knowledge of the ν_τ mass are of special interest.

(5) Finally, $\gamma\gamma$ interactions occur at a high rate, along with electron positron annihilation events, and it is worthwhile to search for new states accessible through photon photon scattering processes.

A detector devoted to the study of these physics topics must fulfill some basic requirements:

(a) It must be able to resolve complex events with both isotropic and jetlike topologies.

(b) It must be able to measure charged particles' momenta, and neutral particles' energies, with high precision, over a large solid angle.

(c) To ensure reliable reconstruction, acceptance calculation, and background determination, it should be as homogeneous as possible.
(d) It must provide excellent particle identification over a wide momentum range, in order to extract the physics of interest.

These differing demands require that compromises must be made on the details of the design.

ARGUS is a magnetic spectrometer with cylindrical symmetry (see fig. 1). Its axial length was fixed by the distance between the horizontal focusing quadrupoles of the storage ring. Increasing their spacing would have led to an undesirable reduction in luminosity. Although a larger detector would have led to improved performance, achieving the maximum luminosity was considered more important.

The transverse size of ARGUS was determined so as to obtain good detector performance over a large solid angle. This requirement is best fulfilled if the diameter of the spectrometer is approximately equal to its length.

The choice of the magnetic field strength was a compromise between good momentum resolution, given by a high field, and loss of low momentum particles, which would curl up in a high field. A field of 0.8 T allows for the reconstruction of tracks with transverse momenta above 30 MeV/c and provides adequate momentum resolution. This is about the maximum field which can be achieved with normal conducting coils, at an affordable power consumption of approximately 2 MW.

Charged particle identification is the most important requirement in this field of physics. It is best realized by two independent methods, implemented over the largest possible range of solid angle. For ARGUS, identification by measurement of specific energy loss in the drift chamber ($\mathrm{d}E/\mathrm{d}x$), and of velocity using the time-of-flight (TOF) system were chosen.

The drift chamber is the heart of the detector and has a twofold purpose. It serves as the track detector, and as a device to identify charged particles by their specific energy loss due to ionization of the chamber gas. For a track detector one aims at homogeneity which is essential for the efficient reconstruction of tracks not coming from the main vertex. Another obvious requirement is good spatial resolution which, with the help of the magnetic field, results in good momentum resolution. Consequently good spatial resolution is necessary, in each drift cell. The cells must be small enough to allow good multitrack resolution. The number of hits per track is determined by the number of cell layers and must be large enough to give a sufficient number of pulse height samples for $\mathrm{d}E/\mathrm{d}x$ measurements. On the other hand, multiple scattering on the wires should be kept low, and the number of electronics channels should stay within acceptable limits. The solution found for the ARGUS drift chamber appears to be a reasonable compromise.

The design of the TOF system aimed at a time resolution of less than 300 ps [1]. This is sufficient to obtain a three standard deviation separation of pions from kaons at momenta of up to 600 MeV/c, and a separation of kaons from protons up to 900 MeV/c. This seemed adequate because, e.g., in B decays the bulk of secondaries occurs at momenta well below 1 GeV/c.

The electromagnetic calorimeter of a detector designed to operate at energies about the Υ resonances must fulfill two tasks: Firstly it must measure the energy of photons and secondly it must support discrimination between electrons and hadrons.

The energy resolution of electromagnetic calorimeters is constrained by technical and financial limits. The performance of a medium quality calorimeter can be improved by placing the components such that the amount of matter between them and the interaction region is minimized. In the case of a magnetic spectrometer this may be done by mounting the calorimeter inside of the magnet coils, which improves the energy resolution and keeps the threshold energy for the detection of photons low.

The ARGUS electromagnetic calorimeter was designed to give good single photon energy resolution, with a granularity high enough to achieve a spatial resolution for photons of 10 to 15 mm.

The detection of muons is of special importance in B and τ physics, therefore a large muon chamber system, covering about 90% of the full solid angle, was designed to complete the ARGUS particle detection capability.

An element not considered in the initial design was the vertex drift chamber, which was installed in 1984. This device considerably improves the accuracy of the measurement of track parameters and vertices.

3. The detector and its components

An overview of the detector components is given in table 1. The coordinate system used throughout this paper is a right-handed Cartesian coordinate system (x, y, z) with its origin at the interaction point. The z-axis points along the beam line, in the flight direction of the positrons, and the y-axis points upwards. Alternatively a polar coordinate system (r, ϕ, θ) is used. The x–y-plane is then referred to as r–ϕ-plane, and θ denotes the polar angle with respect to the z-axis.

3.1. Storage ring elements at the ARGUS interaction region

DORIS II, with a single beam pipe, was constructed using components of the older double storage ring,

Table 1
Summary of detector components

Component	Property	Value
Drift chamber	# channels	5940 TDCs and ADCs
	acceptance for minimal tracks	$\|\cos\theta\| < 0.96$
	acceptance for full tracks	$\|\cos\theta\| < 0.76$
	minimum p_T	30 MeV/c
	momentum resolution	$\sigma(p_T)/p_T = \sqrt{0.01^2 + (0.009 p_T[\mathrm{GeV}/c])^2}$
	dE/dx resolution	$\sigma(dE/dx)/(dE/dx) = 4.5$–$5.5\%$
Vertex drift chamber	# channels	594 TDCs
	acceptance for full tracks	$\|\cos\theta\| < 0.95$
	momentum resolution if used together with DC	$\sigma(p_T)/p_T = \sqrt{0.01^2 + (0.006 p_T[\mathrm{GeV}/c])^2}$
TOF counters	# channels, barrel	128 TDCs and ADCs
	# channels, end cap	96 TDCs and ADCs
	acceptance, barrel	$\|\cos\theta\| < 0.75$
	acceptance, end cap	$0.78 < \|\cos\theta\| < 0.95$
	time resolution	σ(TOF) = 220 ps
Shower counters	# channels, barrel	1280 ADCs
	# channels, end cap	480 ADCs
	acceptance, barrel	$\|\cos\theta\| < 0.75$
	acceptance, end cap	$0.7 < \|\cos\theta\| < 0.96$
	cutoff energy	50 MeV
	energy resolution, barrel	$\sigma(E)/E = \sqrt{0.072^2 + 0.065^2/E[\mathrm{GeV}]}$
	energy resolution, end cap	$\sigma(E)/E = \sqrt{0.075^2 + 0.076^2/E[\mathrm{GeV}]}$
	spatial resolution, barrel	13 mrad at 5 GeV 24 mrad at 0.5 GeV
μ chambers	# channels	1744
	acceptance, inner layer	$0.43 \times 4\pi$
	acceptance, outer layer	$0.87 \times 4\pi$

DORIS. This re-assembly was aimed at increasing the beam energy and luminosity, while reducing power consumption [2].

The desired luminosity of $L > 10^{31}\,\mathrm{cm}^{-2}\,\mathrm{s}^{-1}$, at the Υ energies, was reached by introducing vertical strong focusing quadrupoles of 1 m focal length at distances of 1.23 m from the interaction points (so-called "mini-β quadrupoles"). With their help, the β functions were reduced to 3 cm vertically and 40 cm horizontally. The limit is due mainly to the resulting chromaticity for both planes.

The luminosity is roughly proportional to the inverse of the square of the distance between the centre of the mini-β quadrupole and the interaction point. To minimize this distance, it was necessary to place mini-β quadrupoles in a position where they penetrated the DORIS detectors. For ARGUS, they had to be integrated into the magnet system and were installed inside of the front end plates of the iron flux return yoke. Roughly one third of each quadrupole extends inside the detector (see fig. 2).

Since the longitudinal field of the ARGUS spectrometer magnet could not be allowed to leak into the quadrupoles, compensation coils were placed around

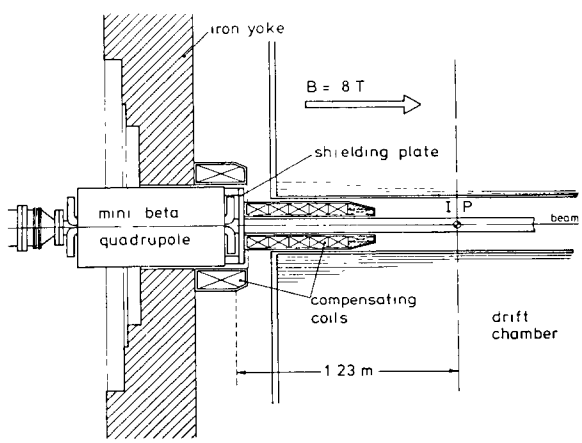

Fig. 2. Mini-β quadrupole inserted into ARGUS.

Table 2
Material between the beam line and the inner volume of the drift chamber. If no thickness in cm is given the thickness in g/cm^2 was determined from the weight and the area of the object. The radiation length L_R for carbon fibre epoxy was determined using the PEGS program. The material of the VDC wires is concentrated in a cylindrical shell of uniform thickness at $r = 9.5$ cm. The use of the γ-converters was optional

Part	Material	L_R [g/cm^2]	Density [g/cm^3]	Thickness		
				[cm]	[g/cm^2]	[%L_R]
DC inner wall	C-epoxy	42.0	1.57	0.33	0.518	1.23
	Ag-paint	8.97	10.50	0.002	0.021	0.23
VDC outer wall	C-epoxy	42.0	1.57	–	0.205	0.49
	stainl.steel	13.84	7.87	0.005	0 039	0.28
VDC volume	CO_2 at 1.5 bar	36.2	$2\,97\times10^{-3}$	9.0	0.027	0.07
	W-wires	6.76	19.3	–	0.0006	0.009
	CuBe-wires	12.86	8.96	–	0.026	0.20
VDC inner wall	C-epoxy	42.0	1.57	–	0.136	0.32
(γ-converter)	Cu	12.86	8.96	0.01/0.04/0.05	0.090/0.358/0.448	(0.70/2.79/3.48)
beam tube	Al	24.01	2.70	0.1	0.27	1.12
	Pb-paint	6.37	11.35	–	0.008	0.13

them and they were shielded by 3 cm thick iron plates at their front faces. Another set of coils, mounted in front to the quadrupoles, compensates for the influence of the ARGUS magnet on the beam. The mini-β quadrupoles are provided with additional current to correct for the decreased field strength due to the saturation of the iron of their yokes, as a result of the residual detector field. This current is adjusted empirically so that the machine tune is independent of the ARGUS field. Measurements of the β functions and luminosity prove that DORIS II remains symmetric, independent of the ARGUS field condition.

The DORIS I synchrotron radiation ports could not be moved from their original positions, hence the bending magnets had to remain in their positions too. There are still vertical bends on either side of the interaction

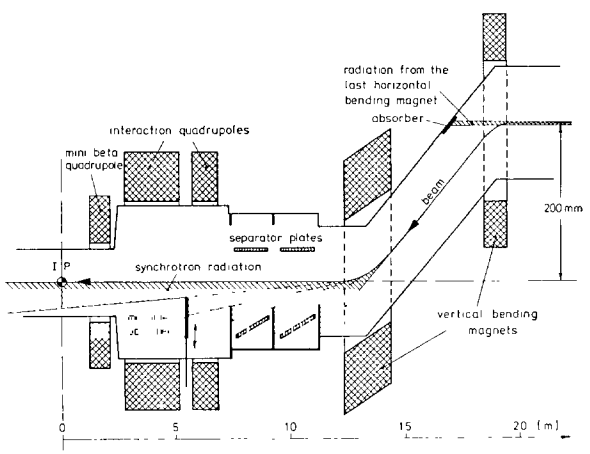

Fig. 3. Vertical bend in DORIS II with synchrotron radiation absorbers.

region in order to prevent it from being illuminated by synchrotron radiation from the last horizontal bending magnets. The low intensity synchrotron radiation from these vertical bends is easily shielded by fixed and movable absorbers ("scrapers"), see fig. 3. The synchrotron radiation background can thus be kept at an acceptable level in the ARGUS interaction region.

The beam pipe at the ARGUS interaction region is an aluminium tube with an inner radius of 40 mm and a 1 mm thick wall, corresponding to 1.12% of a radiation length. It is covered with a layer of lead paint which corresponds to roughly 0.1% of a radiation length. This attenuates the residual synchrotron radiation penetrating into the vertex and main drift chamber.

There are two movable converters made of copper foil (0.1 and 0.4 mm thick), which can be pulled into position around the interaction point. These were used during some data taking periods to increase the photon conversion probability.

The materials between the beam line and the inner volume of the drift chamber are listed in table 2.

3.2. The ARGUS magnet and its field measurements

The magnet system of ARGUS consists of the main solenoid, the mini-β quadrupoles, and the inner and outer compensation coils (see section 3.1). The main field is generated by 13 separate 3 m diameter coils. The maximum current of 4500 A produces a field of 0.8 T. Stable long term running conditions were obtained at 4250 A, corresponding to a field of 0.755 T. The power consumption, including the compensation coils, is then 1.8 MW.

The magnetic field in the interior of the detector was measured in April 1982, prior to the installation of the

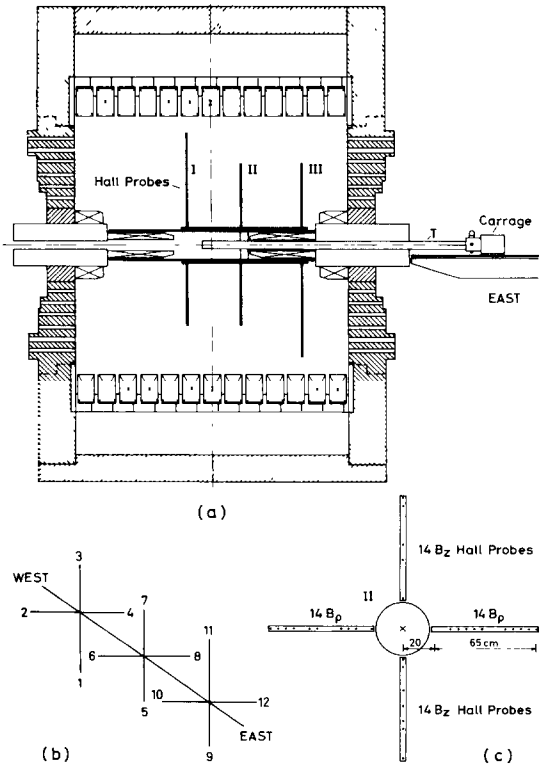

Fig. 4. Apparatus used to measure the magnetic field inside ARGUS: (a) overall view, (b) schematic drawing of probe support arms, (c) end view of one support.

detector components [3]. Most of the measurements were performed in the volume to be occupied by the main drift chamber (see fig. 1). Here the field must be known to a precision of better than 0.1% in order to convert the good spatial resolution of the drift chamber to a good momentum resolution. In the regions occupied by time-of-flight and shower counters, the field was extrapolated to an accuracy of a few percent, which is sufficient.

The BEBC field mapping system from CERN was used to perform and record the measurements. The mechanical scheme for holding and moving the Hall probes is sketched in fig. 4. The supports I, II and III where the Hall probes were mounted were fixed with respect to each other and could be moved, as a whole, along the z-axis by means of the hollow tube T. Measurements were made for the axial (B_z), the radial (B_ρ), and, to a lesser extent, the tangential (B_ϕ) components. This was done for three different inner compensation coil field intensities, corresponding to zero, 50%, and 100% compensation. The spacing between the measured points was 50 mm in the z and radial directions, and 30° in ϕ.

The probes were calibrated at CERN with a nuclear magnetic resonance (NMR) probe. Fig. 5 displays the measured B_z values for zero compensation. The drop in the field values at small ρ and large z is due to the influence of the outer compensation coils.

The symmetry properties of the field have been investigated with respect to ϕ and the plane $z = 0$. Within the measurement uncertainty, of the order of 0.1%, the field is symmetric.

Although no ϕ component is expected for a perfectly solenoidal field, there were B_ϕ values observed ranging from -100 to $+200$ G. This can be explained satisfactorily by contributions due to (1) longitudinal currents between the coils and (2) tilted probes, i.e. measurement errors. The first effect was measurable in the region close to the coils but negligible in the volume occupied by the drift chamber.

The measured field values were corrected for an estimated misalignment of the probes, and by requiring that the field obeys Maxwell's equations [3]. This procedure changed the measured field values by less than 0.3%. The corrected values were parametrized, using polynomials, for each of the 36 drift chamber layers. The number of parameters is less than eight for each layer. The error of the magnetic field values calculated from the parametrization is less than 0.2%. This is the main contribution to the systematic uncertainty of the momentum measurement in the drift chamber (see section 3.3.5).

3.3. The drift chamber

The drift chamber is the central track detector of ARGUS. It has been designed to facilitate track recognition and to measure the momentum and specific

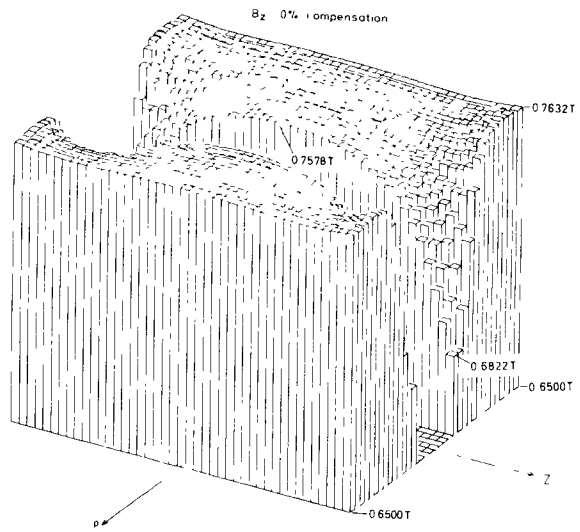

Fig. 5. Magnetic field component B_z measured inside ARGUS for $I = 4275$ A, without compensation.

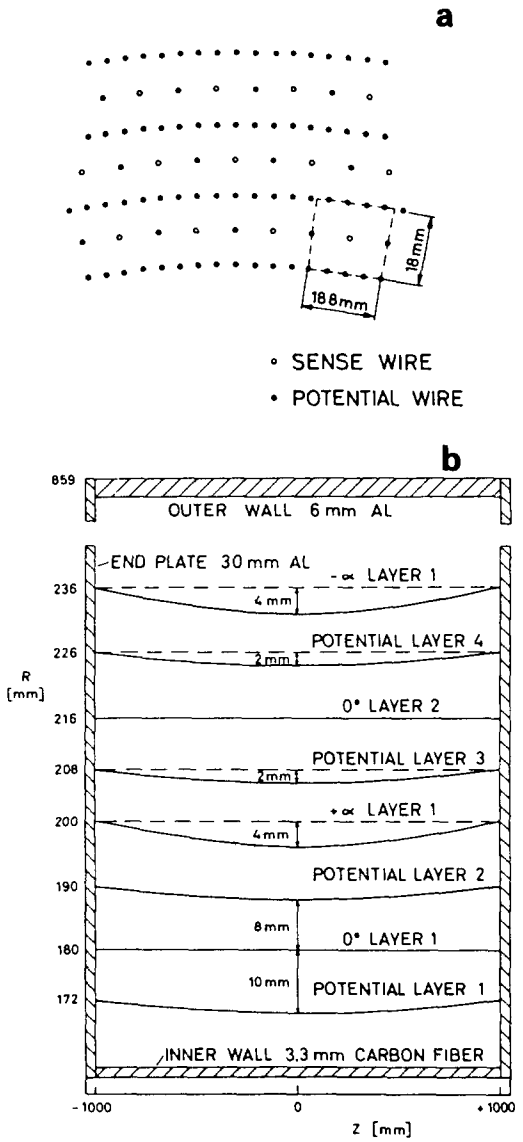

Fig. 6. Schematic drift chamber cross sections (a) perpendicular to and (b) parallel to the beam axis.

ionization of individual tracks. A detailed description of the drift chamber is given in ref. [4].

3.3.1. Geometrical and mechanical data

The cross sections of the drift chamber perpendicular to and parallel to the beam axis are shown schematically in fig. 6. The chamber is 2 m long, with inner and outer diameters of 30 and 172 cm, respectively. The mechanical structure of the chamber consists of an inner wall made of an epoxy carbon fibre material 3.3 mm thick, coated, on the inside, with silver spray, and a 6 mm aluminium outer wall glued to the 30 mm thick aluminium end plates. The end plates contain the holes for the sense and potential wire feedthroughs, with diameters of 5.5 mm and 2 mm respectively. The material between the beam line and the active volume of the drift chamber is listed in table 2.

The 5940 sense and 24588 potential wires form 5940 rectangular drift cells with a cross section of 18.0×18.8 mm^2. The copper–beryllium potential wires have a diameter of 75 μm and are under a tension of 1.1 N. To position and fix them in the end plates, they are crimped in copper feedthroughs with an inner diameter of 150 μm. The sense wires are made of gold-plated tungsten and have a diameter of 30 μm. They are strung with a tension of 0.7 N. The feed through for a sense wire consists of a plastic part * which is inserted into the end plate and positions the wire by a 120 μm hole. The sense wires are crimped in copper tubes similar to those used for the potential wires, which are inserted into the plastic parts from the rear end. The overall mechanical tolerance for the sense wires is less than 100 μm.

The cell size has been chosen to optimize the dE/dx resolution [5]. For an organic gas, such as propane at atmospheric pressure, this is achieved if the energy loss is sampled approximately every 15 mm. A finer sampling does not noticeably improve the resolution. The ARGUS sampling step size of 18 mm is close to optimal.

The drift cells are arranged in 36 concentric layers. The stereo angle sequence is 0°, $+\alpha$, 0°, $-\alpha$, and so on. The stereo angles α increase as $\sqrt{r}$ from 40 mrad at the inner layer to 80 mrad at the outermost layer. Their values are selected by limiting the maximum displacement of a sense wire from the centre of a cell to 1 mm. This displacement occurs because of the hyperboloidal structure of the chamber layers (see fig. 6). The sense wire distance from the layer boundary depends on z. A maximum displacement of 1 mm results in isochrones which are almost circular for all z values, and keeps changes in the gas amplification to less than 10%. In order to allow for large stereo angles, with minimum sense wire displacement, all of the potential wires are also tilted.

Tracks which hit at least four 0° wires and three stereo wires (the minimum requirement for the track fit) can be measured in a region of solid angle $\Delta\Omega/4\pi = 0.96$. The acceptance for tracks which traverse all layers is $\Delta\Omega/4\pi = 0.76$.

Initially the chamber was operated with a 97% propane (C_3H_8) and 3% methylal ($CH_2(OCH_3)_2$) mixture (for a later change see section 3.3.3). Propane has a large radiation length of 45.2 g/cm^2 and small diffusion, thus providing good momentum resolution. The active drift chamber volume represents a thickness of only 0.55% of a radiation length, wires included. Pro-

* Hostaform, Hoechst GmbH.

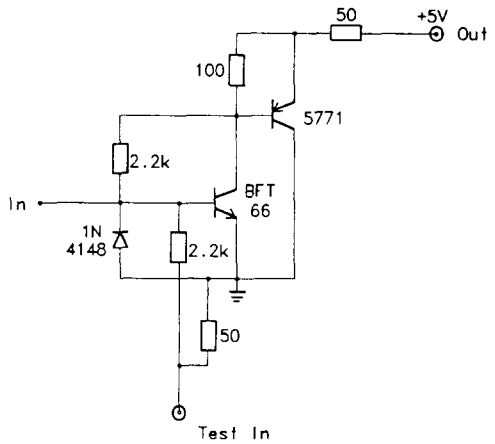

Fig. 7. Circuit diagram of a drift chamber preamplifier.

pane has a much narrower Landau distribution, and hence much better dE/dx resolution than argon, a very common drift chamber gas. On the other hand, the relativistic rise in propane is smaller than in argon so that only a small improvement can be expected for the separation of high momentum particles.

The chamber is operated at a constant pressure of 1035 mbar. It has a gas circulation flow of 12 m^3/h to ensure homogeneous gas distribution and to avoid temperature gradients. The fresh gas consumption is, however, only 30 l/h. The oxygen concentration is kept below 5 ppm.

3.3.2. Readout electronics

The cathode wires, together with the chamber housing, are kept at ground potential. The 2930 V high voltage is fed to the sense wires via a 1 MΩ resistor. This voltage applies for propane with a gas amplification of 10^4 and results in a cathode wire surface field of 25 kV/cm. A regulation unit keeps the voltage stable to ± 0.5 V. The signals are fed out through 470 pF capacitors.

The preamplifiers are mounted directly on the chamber end plates to minimize pickup noise. Each preamplifier channel consists of an input transistor and emitter follower with bootstrap and feedback circuits and has an amplification of 2 mV/μA. The preamplifier circuit diagram is shown in fig. 7. The output signal is transported to the main amplifier, at supply voltage level, via a 31 m (29 m for stereo wires) RG 174 U cable. The rise time is 6 ns for a 30 m cable.

The wire layers are read out so that the electronic components for the 0° layers are located at one end plate, while those for the stereo wires are located on the opposite end plate of the chamber.

For the time measurement, the active element of each main amplifier channel is an amplifier/discriminator chip with ECL output *. The discriminator threshold is adjusted so as to allow wire signals of 0.5 μA to be recognized. The ECL signals are used to start TDCs ** which operate in the COMMON STOP mode. The TDCs are stopped by the delayed event trigger. For charge measurement, the analog signal from the preamplifier is amplified by another factor of 20, delayed by 270 ns, and then sent to an ADC ***.

3.3.3. Operating the chamber with a water vapour additive

After roughly one and a half years of data taking, problems developed while operating the drift chamber. These problems occurred while DORIS was running, but not when DORIS was off and ARGUS was used to take cosmic ray data. A sector of the chamber began to draw currents which increased linearly with time. A normal wire draws 1 nA, while wires in the affected sector were typically drawing 1 μA. The phenomenon was observed to spread with time, until a region at least 15 wires wide and 18 layers deep, was affected. Using a movable ^{55}Fe source on top of the chamber, the damaged region was determined to be approximately in the centre. Here the gain was reduced about by a factor of 2.

After a period of about two weeks, it became impossible to run the chamber with the normal gas mixture. About 1% water vapour was added to the gas mixture and then later reduced to 0.2%. There were no further discharges, and the chamber has since been successfully run in this manner. The gain was found to be uniform throughout the chamber, including the bad sector, which again ran with normal gain.

Some sense and field wires were removed from both the bad sector and other regions of the chamber for analysis. The central regions of the field wires from the bad sector were found to be covered by a sheath of material (2.0 ± 0.2) μm thick. Tests examining the X-ray and Auger electron spectra showed strong carbon lines with some oxygen, nitrogen, silicon and chlorine, but no copper or beryllium lines. In contrast, unused wires gave clear copper and beryllium lines, with small carbon signals. Used wires from other regions of the chamber had small islands of deposits, approximately 0.5 μm thick, distributed along the length of the wire and covering a total of about 5% of the surface area.

Given the behaviour of the chamber during discharge, the evidence for deposits on the wires, and the nature of the solution for the discharge problem, the observed phenomenon can be explained by the Malter effect [6]. Charge from drifting positive ions builds up

* LeCroy MVL100.

** LeCroy System 4290 with 1024 ns full scale, 1 ns/count.

*** LeCroy System 2280 with 1024 pC full scale, 0.25 pC/count.

on the outside surface of the nonconducting deposit, until a sufficient potential is reached to enable extraction of electrons from the field wire, through the insulating layer. The electrons produced by this discharge drift to the sense wire where a new avalanche of positive ions is created, which adds to the charge on the field wire surface. Thus, a feedback mechanism is established, so that a region of permanent discharge appears on the field wire. The current from a given wire grows because the area and the thickness of the deposit grows, the disease spreads.

The addition of water to the gas mixture makes the insulating layers on the field wires conducting. Charge is no longer built up, and no further discharges occur. On the other hand, the electronegative water molecules have a large cross section for electron capture, thus removing some of the drifting electrons. This reduces the efficiency for tracks through the outer regions of a drift cell.

In the beginning of operation, optimization of backgrounds from DORIS beams was performed by minimizing the current drawn by the chamber, with high voltage turned on only in the outermost drift layer. After one and a half years of operation this procedure was changed in order to optimize the chamber operation under high background conditions. Four drift tubes were installed between the outside wall of the chamber and the time-of-flight counters. The currents observed in these detectors are now used to achieve a first optimization of background conditions. The drift chamber is turned on only if the currents in these detectors are below a critical value.

Meanwhile, there is evidence from long-term studies with the drift chamber [7] and from ageing investigations using a small test module [8] that the chamber gain decreases very slowly with time, even with the water admixture.

3.3.4. The drift time–space relation

The drift time–space relation (TSR) gives the most probable drift distance as a function of the measured drift time. In the parametrization of the TSR for ARGUS, the measured TDC counts, corrected for the signal propagation time on the sense wire and the trigger time delay are used, instead of the drift time. In COMMON STOP mode, the relation between the drift time t_d and a TDC value is given by

$$t_d = T_0 - T \text{ with } T = \text{TDC} - T_{0L}. \quad (1)$$

The global time offset T_0 is defined by the STOP delay. The individual time offset T_{0L} is determined separately for each chamber layer, containing 60 to 264 sense wires.

The TSR is determined in an iterative way. At least 1000 tracks from Bhabha scattering events are reconstructed using an approximate TSR. An improved TSR

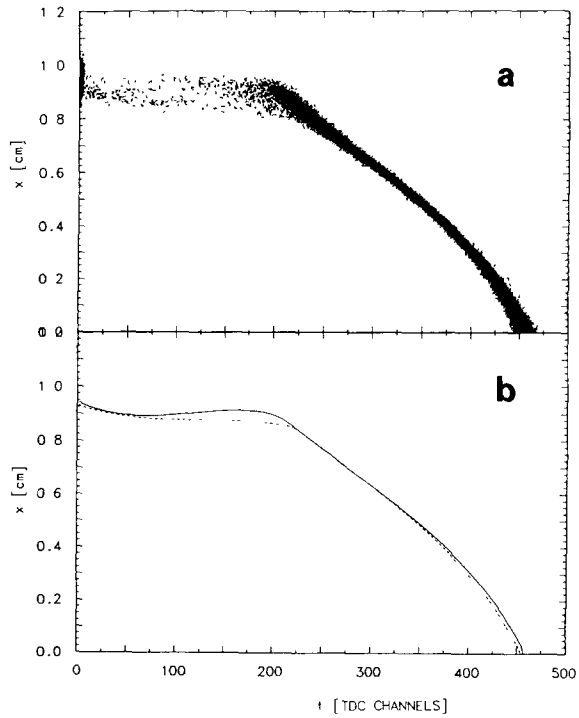

Fig. 8. Drift time–space relation for a 97% propane +3% methylal gas mixture: (a) measured (with water); (b) full line: fit to data shown above, dashed line: fitted drift time–space relation for data without water.

is obtained by smoothing the correlation between the TDC values and the closest distance between a reconstructed track and the signal wire position. In order to parametrize and smooth this correlation the following method is applied:

(1) For drift distances less than 2 mm, the drift distance range is divided into 1000 bins, the mean TDC value in each bin is calculated, and a cubic B-spline with 40 internal knots is used to fit $T(x)$ which is subsequently inverted.
(2) For drift distances greater than 6 mm, the TDC range is divided into 1000 bins and a cubic B-spline with 40 internal knots is used to fit $x(T)$.
(3) In the central region a smooth interpolation between the two parametrizations in used.

The whole procedure is repeated with the new TSR until it converges. The final parametrization of the TSR is provided as a look-up table. Fig. 8a shows the correlation between T and x as given by the reconstruction program. The two curves in fig. 8b show the parametrized TSR for run periods with water (full line), and without (dashed line).

3.3.5. Spatial and momentum resolution

A measure of the spatial resolution is the standard deviation of the distribution of residuals. A residual is

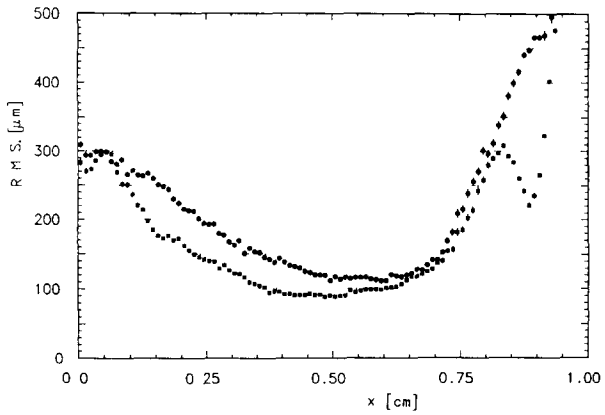

Fig. 9. Spatial resolution for electron tracks from Bhabha scattering events as a function of distance between track and sense wire (squares: with water, circles: without water). The dip at the drift cell boundary is caused by the algorithm.

the difference of the measured and the fitted distance between the track and the sense wire. The residual distributions for electron tracks from Bhabha events and for hadron tracks are different, mainly due to the lower average momenta of hadrons, which suffer more from multiple scattering. The spatial resolution for tracks from Bhabha and hadronic events as a function of the distance between track and sense wire is shown in figs. 9 and 10. At large distances the resolution is bad because here the isochrones deviate strongly from circles, due to the rectangular shape of the drift cell. For tracks close to the wire, the resolution deteriorates because of ionization statistics. A detailed investigation of the spatial resolution of the drift chamber can be found in ref. [9].

For fast particles ($p > 1$ GeV/c), the momentum resolution is dominated by the errors of the track measurement. Fig. 11 shows the distribution of $1/p_T(\mu_1) - 1/p_T(\mu_2)$ for nonradiative QED μ-pairs. The width of the distribution then implies that

$$\frac{\sigma(p_T)}{p_T} = 0.009 p_T[\mathrm{GeV}/c].$$

In Gluckstern's model [10] this corresponds to a mean spatial resolution of $\langle\sigma\rangle = 190$ μm. For momenta below 1 GeV/c the momentum resolution is dominated by multiple scattering

$$\frac{\sigma(p_T)}{p_T} = \sqrt{0.01^2 + (0.009 p_T[\mathrm{GeV}/c])^2}.$$

The absolute momentum scale is determined and monitored by analysing $K^0_S \to \pi^+\pi^-$ decays from secondary vertices. The resulting systematic uncertainty in the mass scale is less than 0.2%.

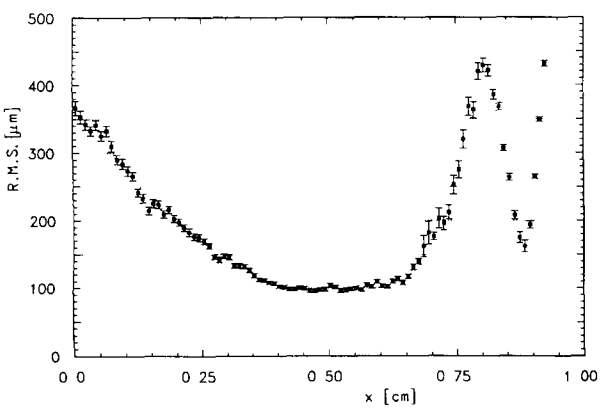

Fig. 10. Spatial resolution for hadron tracks as a function of distance between track and sense wire (with water additive).

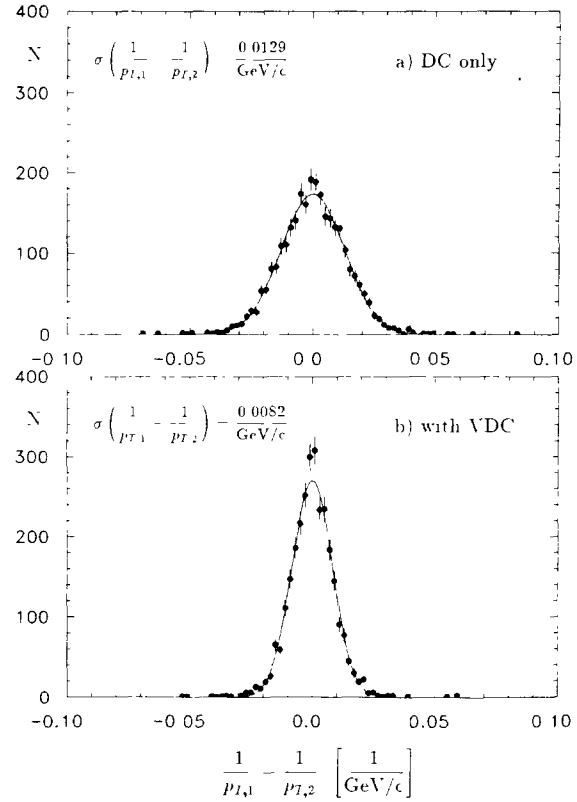

Fig. 11. Distributions of $1/p_T(\mu_1) - 1/p_T(\mu_2)$ for QED μ-pairs. From the observed widths one obtains (a) $\sigma(1/p_T) = 0.009$ (GeV/c)$^{-1}$ if the track fit uses only drift chamber information; (b) $\sigma(1/p_T) = 0.006$ (GeV/c)$^{-1}$ if the track fit uses also vertex drift chamber information.

3.3.6. dE/dx resolution

The energy loss of charged particles moving in a given medium is described by a Landau distribution [11]. The truncated mean method is used to estimate the most probable energy loss. For each track the largest

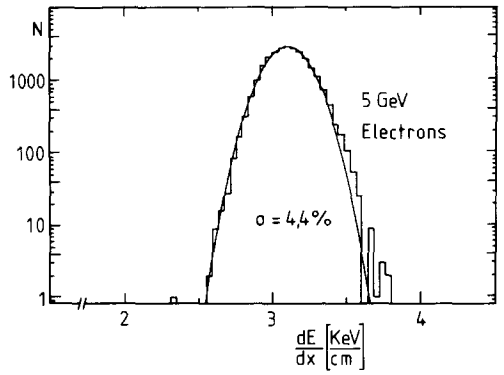

Fig. 12. Specific energy loss for 5 GeV electrons compared to a Gaussian distribution.

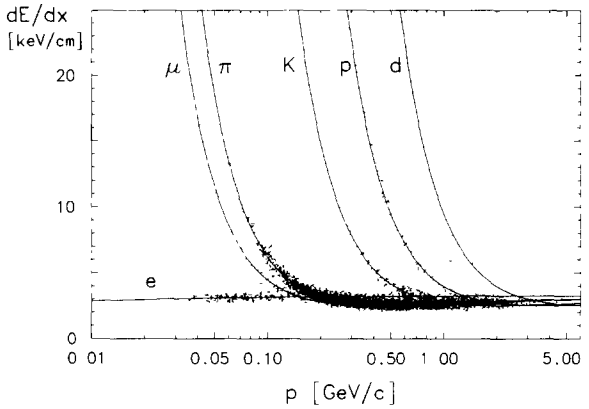

Fig. 13. Specific energy loss vs momentum for approximately 10000 particles of a multihadron data sample.

30% and the smallest 10% of the measured dE/dx values are discarded, and the remaining values averaged. The effect of this method is to make the distribution of the average energy loss closely resemble a Gaussian distribution.

The measured dE/dx values are corrected for space charge saturation effects. For tracks at $\cos\theta \approx 0$ the charge is collected in a very narrow region along a sense wire, and the correction factor can be as large as 1.5. The collected charge also depends on the drift distance, because the ADC sampling gate is provided for all channels at the same time. For long drift distances the pulse tails escape the charge measurement. The corrections due to this effect are less than 15%.

Fig. 12 shows the energy loss distribution for 5 GeV electrons, compared with a Gaussian distribution. There is agreement over roughly three orders of magnitude. The scale is in keV/cm although the experimental data have no absolute calibration and must be scaled by theory [12]. For this data sample, the resolution was 4.4%. The typical resolution achieved was 5%.

Fig. 13 shows a distribution of specific energy loss versus momentum, for approximately 10000 particles. Electrons, muons, pions, kaons and protons are clearly separated, and it is also possible to observe deuterons from beam–gas or beam–wall interactions. The contribution of the dE/dx measurement to the particle separation capability of ARGUS will be discussed in more detail in section 6.4.

3.4. The vertex drift chamber

3.4.1. Chamber design

The ARGUS vertex drift chamber (VDC) is a small cylindrical high resolution drift chamber. The chamber is 1 m long, with outer and inner diameters of 28 cm and 10 cm respectively. It is designed to fit into the space available between the inner shell of the main drift chamber and the beam pipe, and between the two compensation coils. The solid angle coverage for tracks hitting all layers is 95% of 4π. Details of the VDC are described in refs. [13] and [14].

The inner and outer cylindrical walls of the VDC are made of a carbon fibre epoxy composite (0.9 and 1.3 mm thick) in order to reduce multiple scattering. The end plates are made of 2 cm thick G10 (glass fibre epoxy composite). The holes in the end plates for the wire feedthroughs were drilled by a computer controlled machine to an accuracy of 15 μm. The feed throughs were machined from brass stock. The wires are centered in the feed throughs to an accuracy of 5 μm.

There are 594 sense wires (gold-plated tungsten–rhenium, 20 μm diameter) and 1412 field wires (copper–beryllium, 127 μm diameter). They are arranged in a close-packed hexagonal cell pattern to maximize the number of hits per track (see fig. 14). The inscribed radius of a drift cell is 4.5 mm. This small cell size

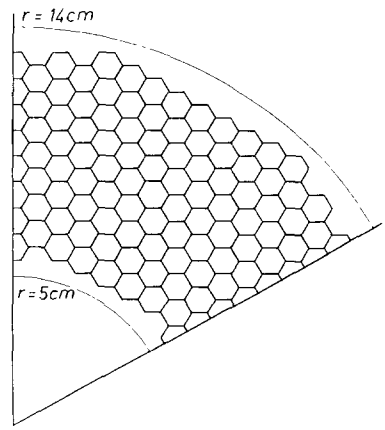

Fig. 14. 60° sector of the close-packed hexagonal cell pattern of the vertex drift chamber. The sense wires are located in the cell centres, the field wires on the corners of the hexagons.

allows the use of single hit electronics despite the high track density experienced for hadronic events at 10 GeV c.m. energy. All wires are placed parallel to the chamber axis, hence the coordinate in the beam direction is not measured.

The VDC is operated with negative high voltage on the field wires, so that voluminous coupling capacitors are not required on the preamplifier inputs. The voltages at the innermost and outermost field wires are adjusted to compensate for distortions of the electric field due to edge effects.

The preamplifiers for the signals from the wires are mounted on the end plates of the VDC. The circuit is the same as that for the main drift chamber preamplifiers except that the output is symmetric (see fig. 7). The total power dissipation is 60 W for a supply voltage of 4.4 V. For cooling purposes a nitrogen flow of about 2 l/s to each end of the chamber is maintained. The preamplified signals are sent via twisted pair cables to the main amplifiers/discriminators * located about 4 m from the chamber. The cables are shielded with 100 μm aluminium foil to reduce the pickup of rf noise. The discriminator ECL outputs drive a TDC system **, operating in the COMMON STOP mode. The time resolution of the TDCs is 1 count/ns with a full scale count of 512 ns. Once a day the entire system is calibrated by means of test pulses sent to all preamplifier inputs.

The absolute pressure in the VDC can be as high as 2 bar. Elevated pressure is essential for obtaining good resolution.

3.4.2. Chamber performance

The VDC has been operated successfully in ARGUS since the spring of 1985. The synchrotron radiation background at the interaction region prevented the use of any gas mixture containing argon. After some tests it was decided to operate the vertex chamber using pure CO_2 at a pressure of 1.5 bar and a high voltage of 3500 V.

The integrated VDC current is used by the DORIS operators to optimize the machine background in the ARGUS interaction region. This was most important during the $\Upsilon(4S)$ running in 1985 when background conditions sometimes were intolerable. A stringent criterion for beam optimization is to keep the total chamber current below 200 μA. The 1986 $\Upsilon(1S)$ running was conducted with much lower levels of background, leading to VDC currents of less than 100 μA.

Since the middle of the 1985 running period we have added 0.3% water vapour to the chamber gas. This has been shown to slow down the degradation of drift chambers caused by deposits on the wires (see section 3.3.3). So far, the innermost sense wires of the VDC have collected a total charge of about 4×10^{16} electrons per millimeter, yet no degradation of chamber performance has been observed. We regularly check the VDC dark current with no stored beam in DORIS, motivated by the expectation that ageing effects would be indicated by an increase of this current. Since the start of VDC operation this current has remained constant at ~ 2 μA.

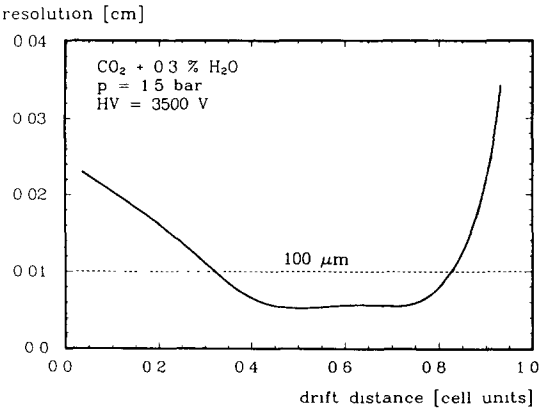

Fig. 15. Spatial resolution vs drift distance obtained from Bhabha scattering events in the VDC.

The drift time–space relation (TSR) for the VDC is determined by a similar procedure as that described for the main drift chamber (see section 3.3.4). For large drift distances, the deviations of the isochrones from circles are taken into account by correcting the TSR values according to the angle at which the track traverses the cell.

The spatial resolution as determined from Bhabha scattering events is shown in fig. 15. There is a plateau of about 50 μm resolution for one third of the total drift length. For about half the cell the resolution is better than 100 μm. Towards the sense wire the resolution deteriorates due to ionization statistics and the linear rise of the drift velocity with the electric field in CO_2. At the outer ends of the drift cell the noncircular isochrones lead to worse resolution. For the reconstruction of hadron tracks the resolution has to be scaled by a factor of 1.4. This is due to the large fraction of low momentum tracks which suffer from multiple scattering.

3.4.3. Improvements due to the VDC

After the VDC was installed it was possible to use the points measured in it as further input for the ARGUS track fitting program, which had formerly used only the points in the main drift chamber. The additional information from the VDC greatly improves the precision of the measured parameters of charged

* LeCroy MVL100 chips mounted on the LeCroy 7791 16-channel card.

** LeCroy System 4290.

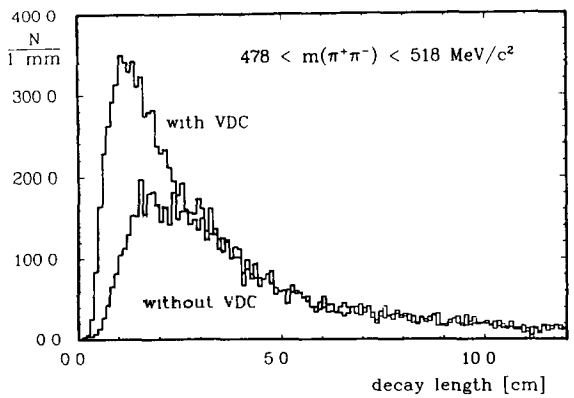

Fig. 16. Decay length d for K_S^0 candidates (unshaded/shaded: track fit with/without VDC).

tracks. Fig. 11 shows that inclusion of the VDC hits in the track fit improves the momentum resolution for 5 GeV/c muons from $\sigma(p_T)/p_T = 0.9\% \cdot p_T$ to $0.6\% \cdot p_T$.

By studying the distance of closest approach between the two tracks in Bhabha events, it was found that single high momentum electron tracks can be extrapolated to the vertex with a precision of (95 ± 5) μm. This accuracy has made possible the measurement of the lifetimes of τ leptons and charmed hadrons [15].

The improved track parameters lead to a considerably higher reconstruction efficiency for secondary vertices from K_S^0 and Λ decays. Fig. 16 shows the distribution of the decay length d between the main vertex and recognized secondary vertices for K_S^0-candidates. There is a clear enhancement in the region $d < 3$ cm if the VDC hits are included in the track fit (unshaded histogram). With the VDC data in the track fit, we detect about 60% more K_S^0 mesons than without. A similar improvement is observed for the reconstruction of Λ baryons.

3.5. *The time-of-flight system*

The ARGUS time-of-flight (TOF) system consists of 160 scintillation counters which surround the track detector. The barrel part contains 64 counters and each of the two end caps contains 48 counters. The light from the barrel scintillators is received by two phototubes, one on each end. The end cap counters have one phototube each. The barrel covers 75%, and the end caps ($0.78 < |\cos\theta| < 0.95$) cover 17% of the full solid angle. A detailed description of the TOF system is given in ref. [16].

The main purpose of the TOF system is to determine the velocities of charged particles by measuring their flight time. Using the momenta measured in the drift chamber, one can identify the particles by their rest mass.

The barrel part of the time-of-flight system is a major component of the fast trigger (see section 4.1). The end cap part is used in the online luminosity monitor (see section 4.3).

3.5.1. *Mechanical layout of the TOF system*

The dimensions of the TOF counters were constrained by the need to lead their light guides through the magnet coils to the field-free regions where phototubes can operate. The holes through the yoke for the light guides must be small enough so that they do not disturb the flux return. The light guide cross section must in turn match the size of the photomultiplier cathode.

The resolution of a TOF system is mainly determined by the number of scintillation photons which reach the photocathode within the integration time of the tube. It is therefore essential to minimize distortions of the initial light front on the way from its origin to the phototube cathode. These distortions depend strongly on the shapes of counter and light guide. According to the prescriptions given in ref. [17], a shape for the one meter long and curved barrel counter light guides was designed which did not deteriorate the resolution when compared to short straight light guides. This was confirmed by tests with cosmic muons. The shape of counters and light guides is sketched in fig. 17.

The counter material is 2 cm thick NE110 *. The barrel counters were cast by the manufacturer. Half of the barrel counters have a rectangular cross section, half of them have a slightly trapezoidal cross section. This solution was chosen to facilitate mounting and to minimize gaps between counters. The end cap counters were cut from scintillator material (also NE110) previously used in the TOF counters of the Double Arm Spectrometer DASP and DORIS [18]. Tests showed that these counters had not suffered any degradation of performance during operation in DASP.

The counters were glued to their light guides with an optical two-component cement **. Tensol + was used for bonds between plexiglass light guide parts. Counters and light guides were covered loosely with aluminium foil and tightly wrapped in black Scotch Wrap. Optical contact between light guide and phototube cathode is made with silicone grease ++. The use of optical grease is preferable to gluing in order to ease the exchange of tubes.

The photomultiplier tubes were originally shielded against residual magnetic fields by μ-metal cylinders and their soft iron housings. It proved, however, that

* Nuclear Enterprises, Inc.
** Stycast 1264, Emerson and Cuming.
\+ ICI Plastics.
++ Rhodorsil B 431, Rhône Poulenc.

this shielding was not sufficient under ARGUS running conditions. Therefore, each photomultiplier housing was covered with an additional soft iron cylinder of 1 cm thickness.

The TOF counters were installed in ARGUS after the shower counters. They are held in position with the help of three large tension rings made of epoxy. The counters are densely packed, and consequently there was no need for an azimuthal support.

3.5.2. Electronic arrangement of the TOF system

The ARGUS TOF system is symmetric with respect to the plane perpendicular to the beam axis at the origin. It is therefore convenient to divide high voltage supply and signal readout into $+z$ and $-z$ hemispheres.

The photomultipliers are RCA 8575 tubes with twelve stages. The high voltage for the phototubes is provided by two power supplies (Heinzinger HNs 3000-025), one for each hemisphere. Each phototube is provided with a separate high voltage source so that their gains may be equalized. These voltages are provided by two distribution boxes which allow that adjustment of each high voltage, in 10 V steps, by means of serial resistors mounted in fuse housings. A similar system serves the shower counter phototubes (see section 3.6.2). The high voltage was adjusted so that the average phototube pulse height is 1 V for minimum ionizing particles. The TOF photomultipliers are monitored by a central laser light source which also monitors the shower counter system (see section 3.6.3).

The analog signals from the phototubes are carried through 25 m coaxial cables (RG 213 U) to passive splitting/delay units which split the signal in the ratio 1 : 4. Eighty percent of the signal is used to trigger a discriminator * whose logical signal, after a cable (RG 213 U) delay of 200 ns, stops the TDC **. All discriminator threshold are fixed at 50 mV and their pulse widths at 70 ns.

A second output of the discriminator is used as an input to the fast trigger logic (see section 4.1).

Twenty percent of the signal, after passing a 250 ns delay line [+] which is part of the splitting unit, is fed to a charge sensitive ADC [++]. The charge measurement of the photomultiplier pulse is used off-line to make a correction to the time measured by the TDC (see section 3.5.3). This is necessary because the discriminator threshold crossing time depends on the pulse height.

* LeCroy 620 BL, modified.
** LeCroy 2228, 1024 counts full scale, 50 ps/count.
[+] TOKO 101 RET.
[++] LeCroy 2282A, 1024 pC full scale, 0.25 pC/count.

The signal starting the TDCs is derived from a coincidence between the fast trigger and the DORIS bunch crossing signal. In order to correct for timing differences between different trigger types, the delayed bunch crossing signal is used directly to stop a special TDC channel. This time difference is used to correct the times measured by the TDCs of the TOF system.

Data from the TOF system are collected by the ADC and TDC processors. The ADC processor (Le Croy 2280) accepts data whose pulse height exceeds a preset digital threshold, and subtracts pedestals. The TDC processors collect data from 16 (barrel) and 12 (end caps) TDC modules respectively, suppress overflows, transfer data and their channel addresses to a memory, and generate Look At Me signals (LAM's).

3.5.3. Calibration of the TOF system

The construction of the TOF system was accompanied by a series of tests with counter prototypes, and finally all counters were precalibrated in an electron beam from the DESY synchrotron [19]. The test runs yielded information on individual counter characteristics, especially on effective speeds of light and attenuation lengths. The average values for the latter quantities are:

$$\langle c_{\mathrm{eff}} \rangle = (15.0 \pm 0.2)\ \mathrm{cm/ns}$$

and

$$\langle z_{\mathrm{att}} \rangle = (209 \pm 30)\ \mathrm{cm}.$$

The attenuation lengths for individual counters vary between 150 cm and 275 cm. The end cap counters exhibit a negative attenuation length, i.e. electrons hitting the end of the counter far from the phototube, produce higher pulses than those particles hitting the near end. This effect is explained by the shape of the counters, which leads to a greater light collection efficiency at the far end.

The flight time of a particle, i.e. the time it takes to travel from the interaction point to the TOF counter, may be extracted from the measured TDC count using a set of calibration constants, and is given by

$$\mathrm{TOF}_{\mathrm{corr}} = \mathrm{TOF}_{\mathrm{unc}} - \kappa\left(\frac{1}{\sqrt{Q}} - \frac{1}{\sqrt{Q_{\mathrm{ref}}}}\right), \tag{2}$$

with

$$\mathrm{TOF}_{\mathrm{unc}} = \epsilon\,\mathrm{TDC} - \frac{l/2 - z}{c_{\mathrm{eff}}} - \Delta \tag{3}$$

and

$$Q_{\mathrm{ref}} = Q_{\mathrm{ref}}(z) = Q(0)\exp\left(\frac{z}{z_{\mathrm{att}}}\right), \tag{4}$$

where

TDC = TDC count,
ϵ = TDC slope (ns/count),

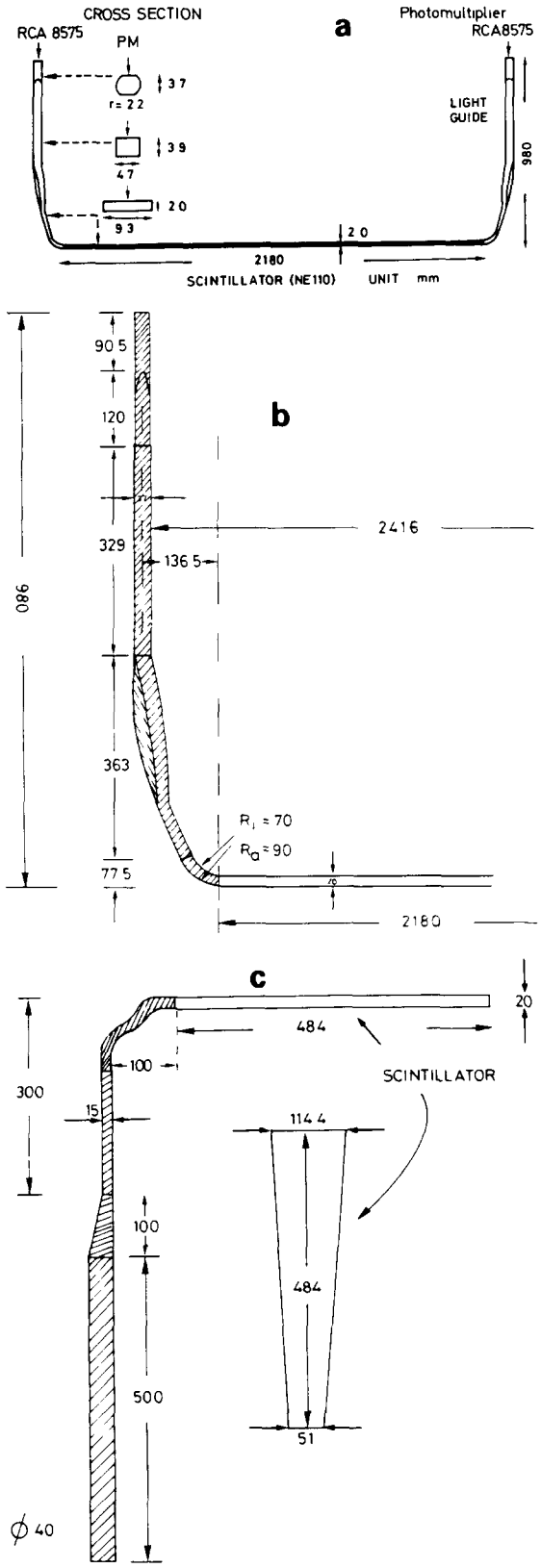

Fig. 17. Sketch of TOF counters and light guides: (a) barrel counter plus light guide, (b) detail of barrel counter light guide, (c) end cap counter plus light guide.

TOF_{corr} = particle's time of flight, pulse height corrected,
TOF_{unc} = time of flight, uncorrected,
l = counter length,
z = coordinate along the counter,
c_{eff} = effective speed of light inside the counter,
κ = slope coefficient for pulse height correction,
Q = charge measured by the ADC,
$Q(0)$ = average charge from the centre of the counter,
z_{att} = attenuation length,
Δ = sum of all additional delays such as cables etc.

These parameters are determined for each counter. The TDC slope is the only parameter which can be measured independently. This is done using a calibrated delay line and the laser monitoring system. The other quantities are strongly correlated and must be determined by fitting them simultaneously.

Calibrating a time-of-flight system requires particles of a well known velocity so that the expected flight time can be calculated from the path length. Muon pairs from e^+e^- annihilations would be ideal for this purpose, but are too rare. Electrons and positrons from Bhabha scattering events are the best second choice. The details of the calibration procedure are described in ref. [16].

3.5.4. The time resolution

An rms TOF resolution of 220 ps is achieved for hadrons. This is exhibited in fig. 18 which shows the distribution TOF(measured) − TOF(expected) for pions at momenta between 300 and 600 MeV/c. The distribution has a Gaussian shape over more than one order of magnitude.

Monte Carlo studies and test runs show that the limiting resolution of the ARGUS TOF counters is of the order of 170 ps [20]. Most of the difference between this value and the observed resolution is explained by the following effects: First, the timing uncertainty of the bunch crossing signal has to be added; secondly, the limited time stability of the phototubes leads to a deterioration of the resolution; and thirdly, the parametrization chosen for the pulse height correction is inaccurate for extremely high and low pulses. A further cause of deterioration in the overall resolution are background effects such as backscattered electrons which make proper timing impossible.

3.5.5. The TOF particle identification analysis

Identification of a particle by time-of-flight is per-

formed by measuring its velocity β and determining its rest mass according to

$$\frac{1}{\beta} = \frac{c\mathrm{TOF}}{l} = \sqrt{1 + \left(\frac{mc^2}{pc}\right)^2}, \tag{5}$$

or

$$m^2 = p^2\left(\frac{1}{v^2} - \frac{1}{c^2}\right). \tag{6}$$

For constant time resolution, the mass resolution varies with the square of the momentum:

$$\sigma(m^2) = 2(p/l)^2\ \mathrm{TOF}\ \sigma(\mathrm{TOF}). \tag{7}$$

For a time resolution of 220 ps, this formula leads to the following three standard deviation limits for particle separation: pion–kaon up to 700 MeV/c, and kaon–proton up to 1200 MeV/c.

The particle identification power of the ARGUS TOF system is shown in a scatter plot of mass squared versus momentum, fig. 19, where mass squared is calculated from momentum and velocity as given above. Only good quality tracks from a multihadron sample were used in this plot. At low momenta, up to 230 MeV/c, it is possible to distinguish the contribution from electrons. In a typical multihadron sample, useful TOF information is available for about 80% of the tracks with transverse momenta $p_T > 120$ MeV/c. For details of the TOF off-line analysis in the context of particle identification, see section 6.4.

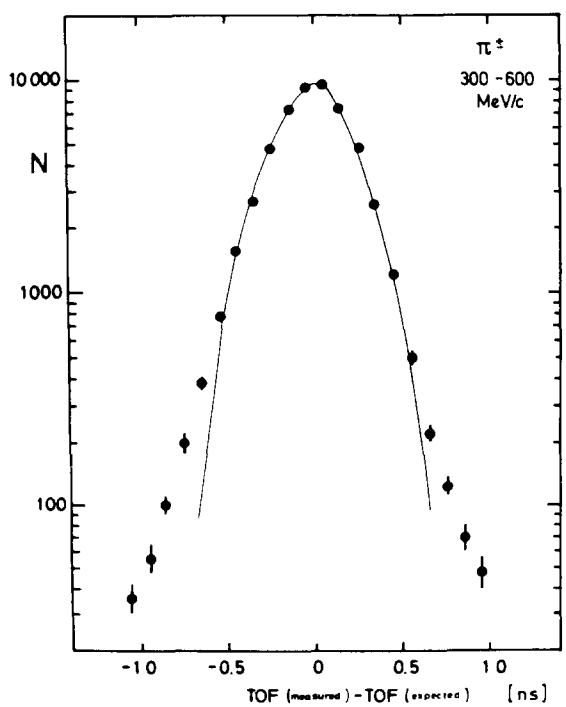

Fig. 18. Distribution of TOF(measured) minus TOF(expected) for pions at momenta between 300 and 600 MeV/c.

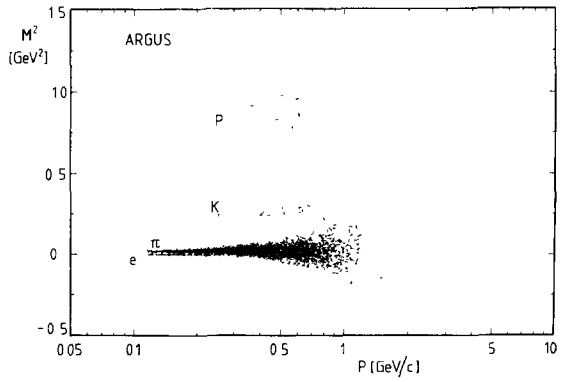

Fig. 19. Mass squared from TOF vs momentum for hadron tracks.

3.6. The electromagnetic shower counters

The ARGUS shower counters fulfill a fourfold purpose:

(1) They measure the energy of electrons, as well as the energy and direction of photons.

(2) The shape of the shower and the amount of energy deposited permit the separation of electrons from muons and hadrons. The characteristic differences of the energy distribution for these different particle species are discussed in section 3.6.5.

(3) They are used to construct a total energy trigger that selects events which deposit an energy above a preset threshold in the calorimeter. In addition, they are used in the trigger for charged particles. Details of the trigger are described in section 4.1.

(4) They allow on- and off-line measurements of luminosity. A hardwired monitor counts Bhabha events hitting the end cap shower counters, thus measuring the luminosity on-line. In the off-line analysis, Bhabha events recorded in the barrel shower counters are used to measure the integrated luminosity with high precision (see section 4.3).

Details of the ARGUS shower counters have been published in refs. [21–24].

3.6.1. Geometrical arrangement

The ARGUS electromagnetic calorimeter consists of two parts (see fig. 1). Particles in the central region ($|\cos\theta| < 0.75$) are detected in the barrel calorimeter, while those travelling in the forward and backward regions ($0.7 \leq |\cos\theta| < 0.96$) hit the end cap calorimeter. The angular acceptance of the electromagnetic calorimeter is 96% of 4π.

The barrel section is divided into 20 rings of 64 counters each. Each end cap consists of five rings of increasing radius with 32, 40, 48, 56, and 64 counters respectively. The total number of counters is: 1280 (barrel) + 2 × 240(end cap) = 1760.

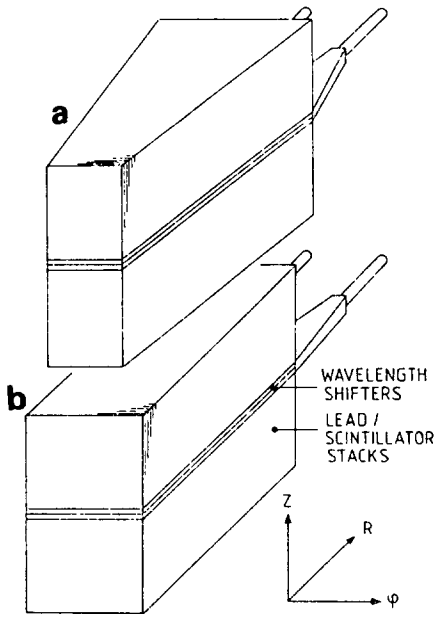

Fig. 20. Calorimeter modules used in the barrel shower counter: (a) "wedge", (b) "parallel".

The shower counters are of the lead-scintillator sandwich type, with 5 mm thick scintillator plates *. The thickness of the lead plates is 1 mm in the barrel region and 1.5 mm in the end cap regions. The overall length of each counter corresponds to 12.5 radiation lengths, and its width to 1.0 (0.9) Molière radius for the barrel (end cap) shower counters. In order to adapt the shape of the counters to the cylindrical geometry of the support structure, plane-parallel and wedge-shaped counters were built (see fig. 20). For each type two counters are combined into one shower counter module which is tightly held together by four layers of a special black thermal shrinking hose **. Each of the two counters is read out by a wavelength shifter bar of 3 mm thickness, placed between the two stacks in the middle of each module. They are coupled to 1 inch phototubes (Valvo XP 2008 UP) via adiabatic light guides (see fig. 21). The wavelength shifters are carefully shielded from each other by aluminized mylar foil to eliminate cross talk. Two 0.3 mm thick nylon threads maintain an air gap between absorber stack and wavelength shifter to ensure total reflection. The whole module and the light guides are wrapped in aluminium foil. Each stack is connected to a quartz fibre light guide to allow laser calibration pulses to reach the photomultiplier. The shower counters are mechanically supported by a structure made of nonmagnetic stainless steel.

The shower counter modules are placed inside the magnet coil. The total amount of material in front of the counters is 0.16 radiation lengths in the region of the barrel calorimeter ($\cos\theta = 0$), and 0.52 radiation lengths in the end cap regions ($\cos\theta = 0.9$). This arrangement allows the detection of photons with energies as low as $E_\gamma \approx 0.05$ GeV with high efficiency and good energy resolution [21].

3.6.2. High voltage and readout system

Because the shower counters are an important part in the fast trigger system, their gain must be adjusted in such a way that the threshold for all trigger groups is about the same. It is necessary to compensate for the gain variations of the photomultipliers as well as variations in the light collection efficiencies from module to module, by a proper high voltage setting. This is achieved by inserting resistors mounted in fuse housings into the high voltage chain. By using resistors with values between 50 kΩ and 1830 kΩ, the high voltage for each individual photomultiplier can be adjusted in steps of

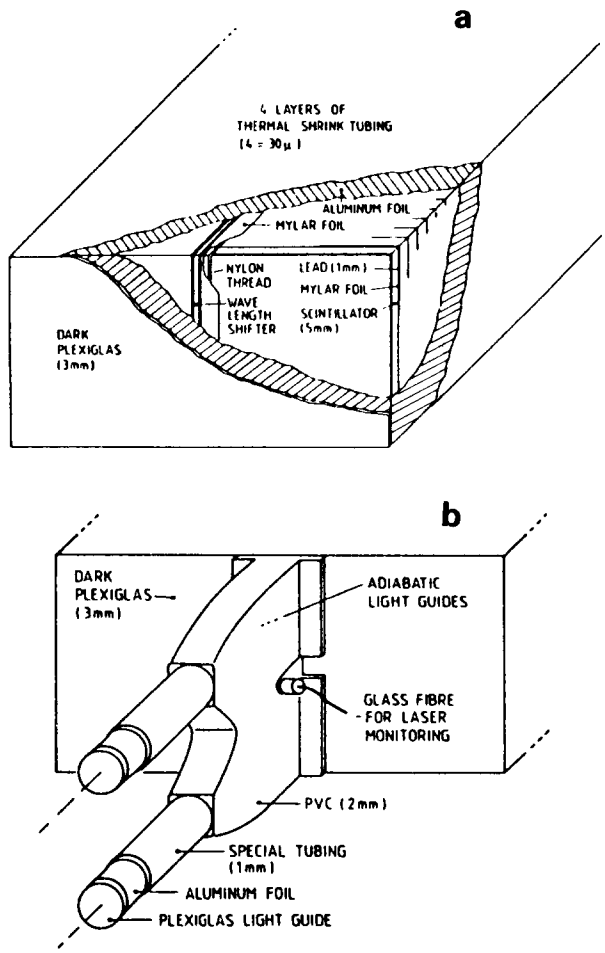

Fig. 21. Construction of a "parallel" shower counter module: One module contains two stacks of lead and scintillator plates which are read out via wavelength shifters. (a) Front end view; (b) rear end with light guides and monitor input.

* ALTUSTIPE UV 15105, Altulor, Paris la Defense, France.
** NALOPHAN, Kalle AG, Wiesbaden, FRG.

about 15 V, which corresponds to a relative gain of 10%. The high voltages are readjusted at least every six months and more frequently when it is necessary.

The counter signals are sent over 35 m long RG 58C/U cables into Split–Delay–Summing (SDS) units with 22 inputs each. Here, each signal is delayed by 240 ns before it is provided to an ADC module. In addition, the SDS units act as linear fan-ins. Signals are added in groups of 22, 14, or 8 channels, these sums being used for the fast pretrigger (see section 4.1). The integral nonlinearity of the SDS units is about 1%, and the long term stability better than 1 dB.

The signals are digitized using the LeCroy 2280 12-bit ADC system. The ADC pedestals are determined three times a day and stored in the memories of the two ADC processors. After digitization, the pedestals are subtracted and all ADCs with a signal of more than two channels above pedestal are read out by the on-line computer. The linearity of the ADC system has been carefully checked. No deviation could be found.

3.6.3. Calibration of the shower counters

The absolute energy calibration of each shower counter module is done using electrons and positrons from Bhabha scattering. The cross section for this process is high enough to allow a calibration of all shower counters based on a data sample corresponding to 7 pb^{-1}, or to roughly 5×10^5 Bhabha events. In total, 30 different sets of calibration constants are available for the data collected during the first four years of ARGUS running, each for a specific running period. In this paper, only the general information concerning the calibration and monitoring procedures is given. These are described in detail elsewhere [24].

Bhabha scattering events are selected by a procedure which minimizes the number of radiative events. The electron and positron energies are known with high precision from the beam energy. The impact points of the tracks at the shower counters are derived from the drift chamber track reconstruction. The ratio of measured shower energy and the energy which should be deposited can be calculated for each track k,

$$r_k = \frac{1}{E_p} \sum_{j=1}^{n} P_j C_1 C_2(E_p, \theta) C_3^j(t) \epsilon_{cal}^j, \tag{8}$$

where

E_p = energy of the electron or positron,
P_j = pulse height of shower counter j,
C_1 = ratio of energy deposited in the counter to energy detected in the scintillator,
$C_2(E_p, \theta)$ = correction factor for angle dependent leakages, losses of shower particles and for variations of light collection with the impact point of the showering particle,
$C_3^j(t)$ = correction factor describing the time dependent gain variation of the jth phototube,
ϵ_{cal}^j = absolute calibration constant of counter j.

Details of the determination of these correction constants are discussed in ref. [24]. The symbol r_k denotes the ratio of measured to deposited energy for the group of counters which have been hit by the electromagnetic shower. The absolute calibration constant ϵ_{cal}^j can be derived from the above equation in the following way:

$$w_k^i = \frac{P_i C_1 C_3^i(t) \epsilon_{cal}^i}{\sum_{j=1}^{n} P_j C_1 C_3^j(t) \epsilon_{cal}^j}, \tag{9}$$

w_k^i being the relative weight of counter i in shower k,

$$\frac{1}{\epsilon_{cal}^i} = \frac{\sum_k r_k w_k^i}{\sum_k w_k^i}. \tag{10}$$

Hence ϵ_{cal}^i is determined from an average over all clusters to which the counter i contributed. The system of eqs. (8), (9) and (10) is solved iteratively, and the process converges quickly.

The stability of $C_3^j(t)$ is checked on a daily basis with a laser monitor system [24]. The laser provides light pulses to the phototubes of TOF and shower counters. During the calibration run 200 pulses are delivered to each counter and the resulting ADC values collected for off-line processing. The monitor system provides a means of compensating for any short term variations in the gain of the photomultiplier tubes and in the readout electronics, whereas any changes due to radiation damage in the scintillator or in the wavelength shifter remain undetected. Therefore the energy measured for electrons from Bhabha scattering has been determined without recalibration ($\epsilon_{cal}^i = 1$). From this we conclude that we do not yet observe any radiation damages in our counters. Measurements with small dosimeters gave a maximum energy deposit of 50 rad during six months in the innermost shower counters near the beam tube. This is far below the critical dose of our scintillator [25]. The observed reduction in gain can be explained as an ageing effect of the photocathode and the dynodes of the photomultiplier [26].

As an example of the reliability of the calibration procedure, fig. 22 shows the ratio of measured energy to the beam energy as function of time. Within a few percent, this ratio is constant.

3.6.4. Energy and angular resolution

The energy resolution at high energies has been determined from the energy distribution of electrons from Bhabha scattering (fig. 23), and that of photons from the process $e^+e^- \to \gamma\gamma$ (fig. 24). The energy reso-

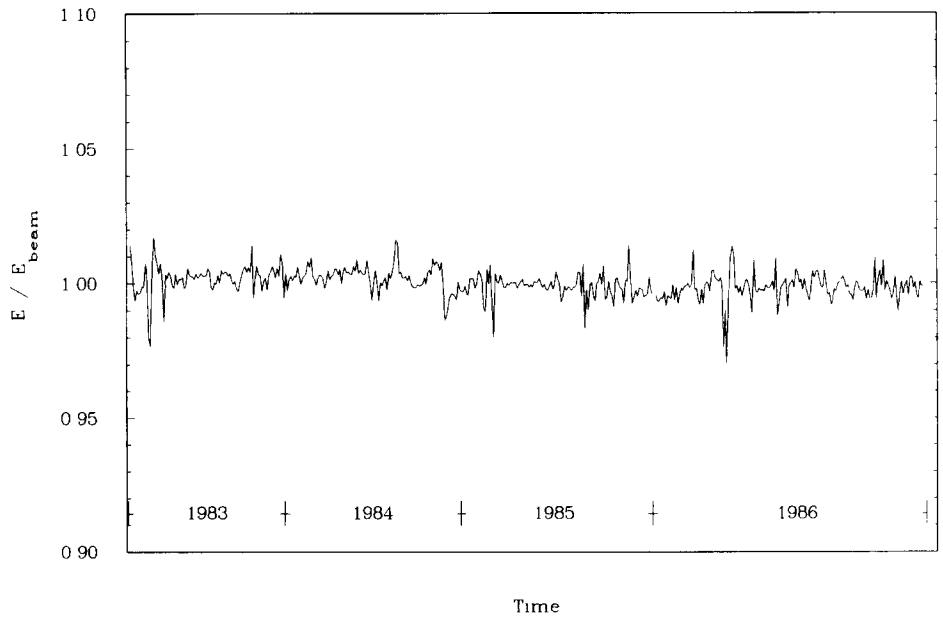

Fig. 22. Ratio of measured energy and beam energy for Bhabha electrons as a function of time.

lution of low energy photons is determined from the mass spectrum of π^0 mesons (fig. 25) and η mesons (fig. 26). The data sample in the case of the π^0 mesons is large enough to analyse only those $\gamma\gamma$ combinations where one of the photons is detected in the shower counters, while the second one converts into an e^+e^- pair either in the beam tube or in the drift chamber wall. Because of the excellent energy resolution of converted photons the π^0 mass distribution directly reflects the resolution achievable for low energy photons.

The resolution obtained can be parametrized by the expression

$$\frac{\sigma(E)}{E} = \sqrt{0.072^2 + \frac{0.065^2}{E[\mathrm{GeV}]}}$$

in the barrel part of the detector, and by

$$\frac{\sigma(E)}{E} = \sqrt{0.075^2 + \frac{0.076^2}{E[\mathrm{GeV}]}}$$

in the end cap regions. Monte Carlo studies show that the constant term is mainly due to contributions from the support structure.

The impact point of a photon and hence its production angle is derived from the centre of gravity of the shower:

$$u_s = \frac{\sum_{i=1}^{n} u_i P_i}{\sum_{i=1}^{n} P_i}. \qquad (11)$$

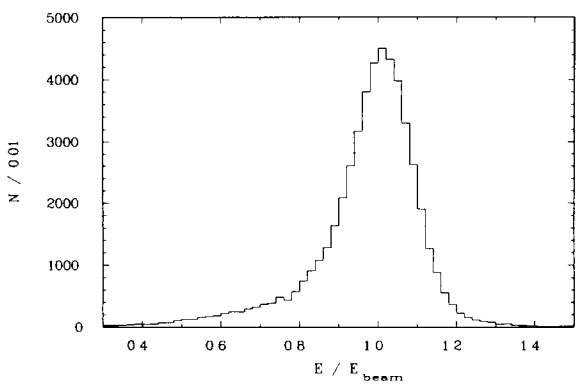

Fig. 23. Energy distribution of electrons from Bhabha scattering.

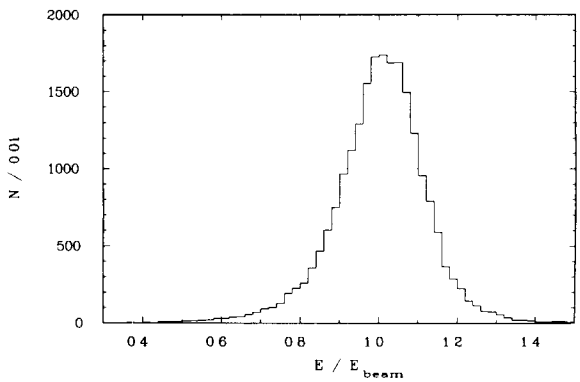

Fig. 24. Energy distribution of photons from the reaction $e^+e^- \to \gamma\gamma$.

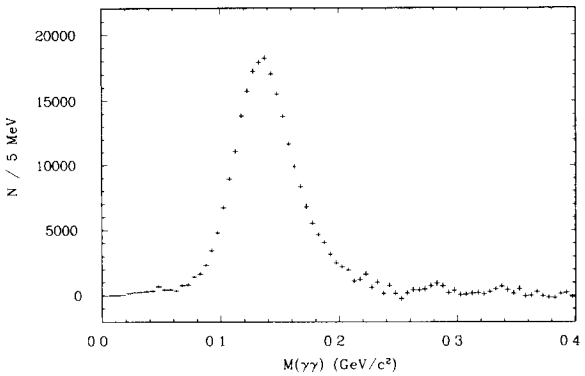

Fig. 25. Invariant mass distribution of π^0's reconstructed from photons detected in the shower counters (after background subtraction).

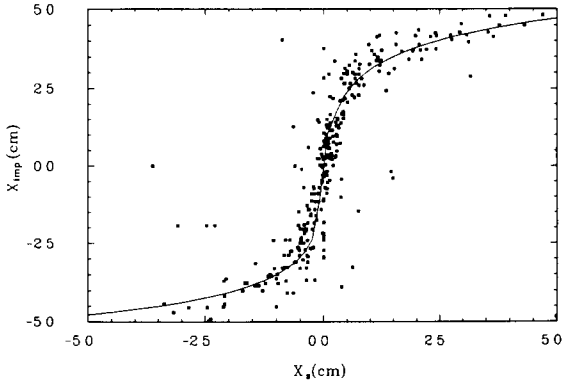

Fig. 27. Relation between real impact point x_{imp} and calculated centre of gravity x_s.

Here, n is the number of counters hit by the photon shower, P_i is the corresponding pulse height recorded in counter i, and u_i is the coordinate of the centre of the ith shower counter. For the barrel shower counters the z-axis, the detector symmetry axis is used ($u_i = z_i$), while for the end cap counters the radial distance r_i from the detector axis is chosen ($u_i = r_i$).

For two energies (0.5 and 5 GeV) the correlation between the real impact point z_{imp} and the calculated centre of gravity z_s was determined in a Monte Carlo simulation. For the analysis it is available in tabulated form. For other energies the corresponding relationship is derived by interpolation (extrapolation), assuming a logarithmic energy dependence.

The azimuthal angle of the photon impact point is derived from the Cartesian coordinate

$$x_s = \frac{\sum_{i=1}^{n} x_i P_i}{\sum_{i=1}^{n} P_i}, \qquad (12)$$

where x_i is measured in the front plane of a shower counter module perpendicular to the z-direction. The value $x = 0$ corresponds to the centre of that counter module in the cluster which has the maximum pulse height. The relation between x_s and the real photon impact point x_{imp} is again derived from Monte Carlo calculations. The corresponding function is to good approximation energy independent. For the barrel shower counters it is shown in fig. 27.

To determine the angular resolution, the impact point of electrons and positrons from Bhabha scattering events has been reconstructed by the algorithm used for photons. The opening angle between the electron and the "photon" is plotted in fig. 28 for the barrel region. The angular resolution at high energies is 13 mrad, which corresponds to a spatial resolution of 1.5 cm averaged over the barrel region. For the end cap calorimeter the resolution is slightly better (10 mrad, 1.2 cm) which is due to the smaller dimensions of the counters. The angular resolution deteriorates with decreasing energy (24 mrad at 0.5 GeV in the barrel region) and is for small energies limited by the geometrical dimensions of the shower counter modules.

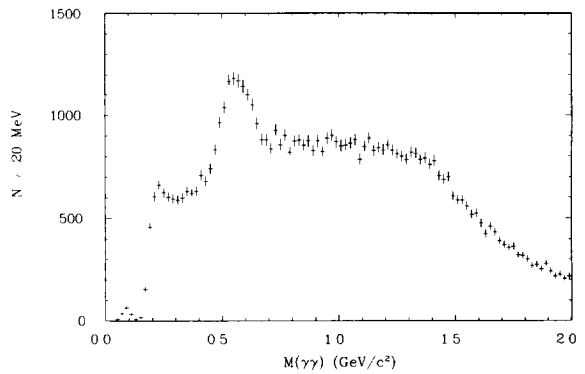

Fig. 26. Invariant mass distribution of η's reconstructed from photons detected in the shower counters.

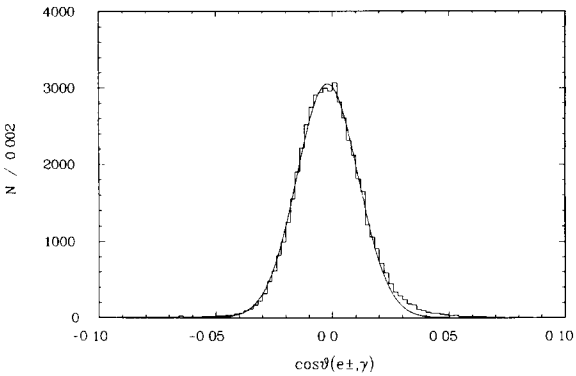

Fig. 28. Angular difference of impact points derived from track and shower reconstruction for Bhabha electrons.

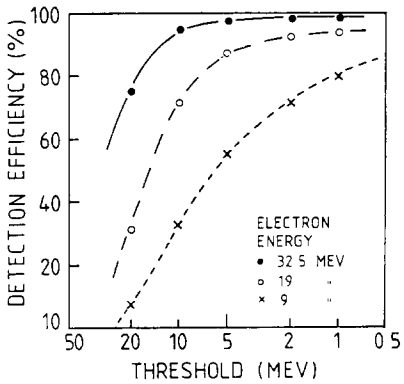

Fig. 29. Detection efficiency for 9, 19 and 32.5 MeV electrons as a function of a software threshold: An electron is "detected" if the energy deposition in at least one absorber stack exceeds the threshold. Since especially the 9 MeV data include a few percent of fake triggers, the efficiencies shown should be regarded as lower limits. The data are averaged over impact points and angles.

The shower counters of the detector ARGUS are set up inside the magnet coil in order to minimize the amount of material in front of them. In this way a very good low energy detection threshold for photons is achieved. The detection efficiency was determined with a low energy electron beam (9 MeV $\leq E_e \leq$ 40 MeV) at three different electron energies. It is plotted in fig. 29 as a function of the energy threshold applied to a single counter [21]. A particle is detected when the energy deposited in at least one counter exceeds this threshold. The pulse height cut applied in the experiment corresponds to a threshold of 6 MeV, resulting in a detection efficiency of $\geq$ 98% for 50 MeV photons. In the analysis, only photons with an energy $E_\gamma \geq 50$ MeV are considered. The systematic underestimation of the photon energy due to the cut applied to the pulse height of each counter has been determined from the difference between the table value and the π^0 mass measured with low energy photons, where the second photon has been reconstructed from a conversion e^+e^- pair (see fig. 30).

3.6.5. Particle identification performance

The separation of electrons, muons and hadrons with the help of the shower counters is based on the different lateral energy deposit and the fact that only electrons deposit almost all their energy in the calorimeter.

The energy deposit of electrons and hadrons in the shower counters for different particle momenta is compared in fig. 31. While for electrons the deposited energy and the particle momentum are strongly correlated, no correlation is observed for hadrons. A cut $|E - |cp|| \leq N\sigma$ (with $\sigma^2 = \sigma_p^2 + \sigma_E^2$ and $N = 3$–4) already rejects an appreciable fraction of hadrons, while the detection efficiency for electrons remains at 86% for $N = 3$.

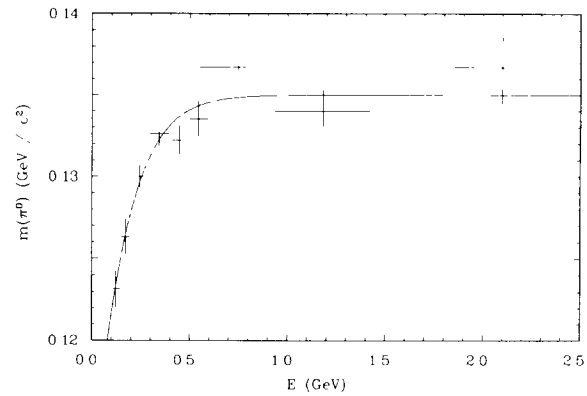

Fig. 30. Reconstructed π^0 mass as a function of the photon energy measured in the shower counters. A correction for this effect is derived from the fitted solid curve.

Furthermore, the lateral energy deposits of electrons and interacting hadrons differ drastically. For hadrons the energy is shared by more counters and is distributed

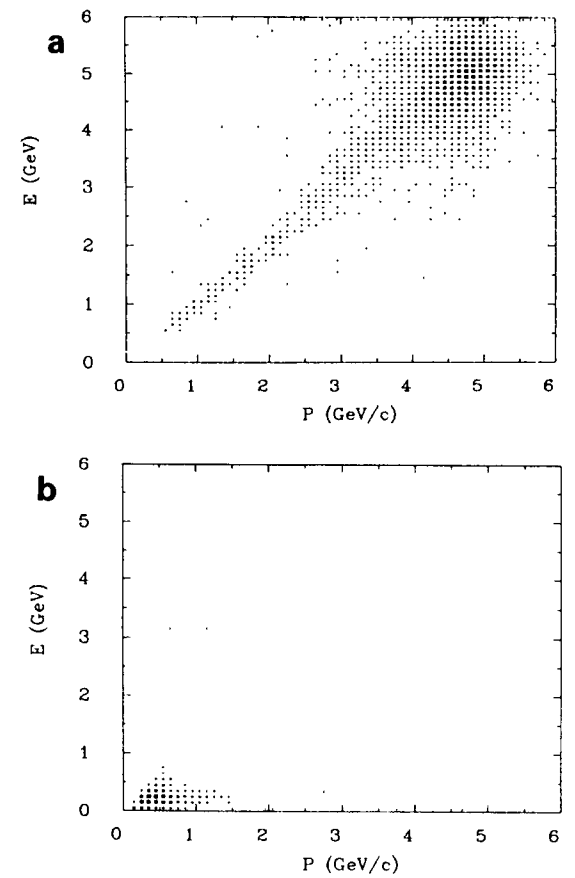

Fig. 31. Energy deposition in the shower counters vs momentum: (a) electrons, (b) hadrons.

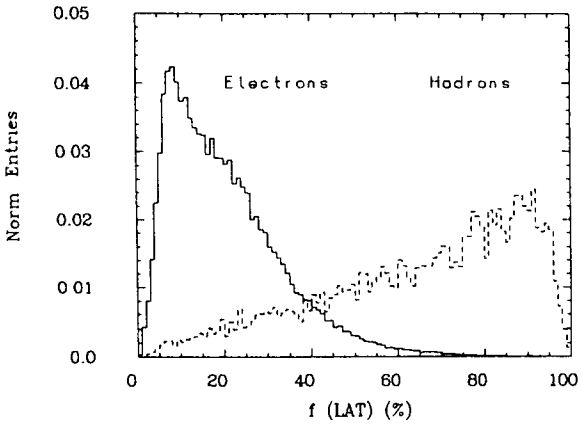

Fig. 32. Distribution of f_{lat} for electrons and hadrons with $E \geq 1$ GeV.

more uniformly [23]. Starting from this observation, an algorithm was developed which is used to separate electrons from interacting hadrons. The lateral width of the energy distribution for all showers with ≥ 3 counters hit is characterized by the variable

$$E_{\text{lat}} = \sum_{i=3}^{n} \frac{(r_i - r)^2 E_i}{\langle r \rangle^2}, \tag{13}$$

where

r_i = radius vector of counter i,

E_i = energy deposition in counter i (with $E_1 > E_2 > \ldots > E_n$),

$\langle r \rangle \approx 10$ cm is the average distance between the centres of two counters,

$r = \Sigma_1^n E_i r_i / \Sigma_1^n E_i$ is the radius vector of the shower (centre of gravity).

Note that the two counters with the highest energy deposit do not contribute to E_{lat}. The fractional lateral energy spread is defined by

$$f_{\text{lat}} = \frac{E_{\text{lat}}}{E_{\text{lat}} + E_1 + E_2}, \tag{14}$$

with $0 \leq f_{\text{lat}} \leq 1$.

As demonstrated by the results plotted in fig. 32, a cut on this variable allows the separation of electrons from hadrons. The particle identification capability based on the relative lateral size of a shower improves with increasing momentum. This method works only for energies greater than 0.6 GeV, because hadronic showers do not develop at lower energies.

Muons and noninteracting hadrons can be separated from interacting hadrons and from electrons because of the small number of counters set. In addition, the energy deposit per unit length is smaller for muons than for interacting hadrons (see fig. 33). Clearly this variable also provides a means of separating muons from electrons.

The differences in the patterns of energy deposit for electrons and hadrons described in this section can be combined with information from other particle identification devices of ARGUS. The algorithms for separating electrons from other charged particles are presented in section 6.4.2.

3.7. The muon chamber system

3.7.1. Chamber design

ARGUS is equipped with three layers of muon chambers (see fig. 1). One layer is installed inside the magnet yoke, separated by 3.3 absorption lengths of material from the interaction point, and covers 43% of the full solid angle in the barrel region of the detector. Two layers outside the yoke (a further 1.8 absorption lengths) cover 87% of the full solid angle. Their overlap, with crossed sense wires, is 93%. The momentum cutoff for muons due to the presence of the absorbing material is 700 MeV/c for the inner and 1100 MeV/c for the outer layer of muon chambers. The chambers are described in detail in ref. [27].

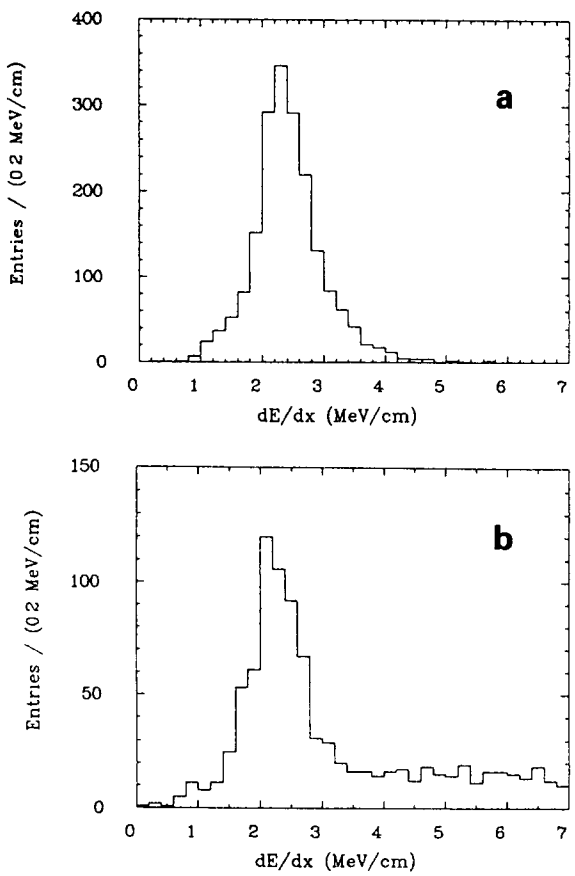

Fig. 33. Energy deposition per unit length for (a) muons and (b) hadrons.

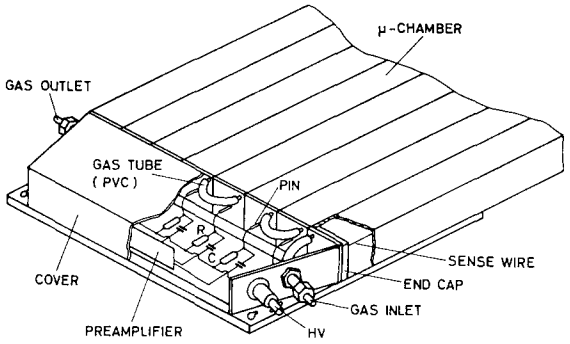

Fig. 34. Schematic view of a muon chamber.

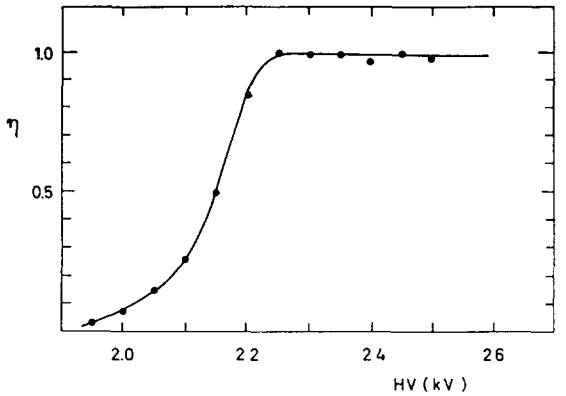

Fig. 35. Chamber efficiency as a function of the high voltage.

A single chamber consists of eight proportional tubes glued together and welded to aluminium bars at either end (see fig. 34). A high voltage connector and distribution board, a preamplifier connector, and a gas inlet and outlet are attached to the aluminium bar on one end of each chamber. The chambers have lengths in a range from 1 to 4 m according to their location.

Each counter was made from a rectangular extruded aluminium tube of an internal cross section of 56×56 mm^2 and 2 mm wall thickness. A 50 μm gold-plated tungsten wire stretched with a tension of 1.5 N ($\pm 10\%$) was positioned in the centre of the tube with an accuracy of ± 0.03 mm. The wire was crimped in a thin brass tube epoxied in the centre of the plastic end cap which also contained a gas inlet. These end caps were glued into the aluminium tubes with silicone rubber, thus providing a gas tight volume for each counter.

3.7.2. Testing procedure

Before installation at ARGUS, all chambers underwent a preliminary test of dark current and leakage. The dark current did not exceed 20 nA at a high voltage of 3 kV when the chambers were filled with nitrogen.

The leakage of a single chamber was less than 2×10^{-3} Torr/s at a pressure of about 10 mbar above atmospheric pressure. Thus the leakage for all chambers with a total volume of 20.5 m^3 was 0.15 l/min.

The chambers are operated with a nonflammable gas mixture of 92% argon and 8% propane. The counter detection efficiency and the drift velocity have been measured in a 2 GeV electron test beam at DESY. The typical efficiency dependence on high voltage for a single counter is shown in fig. 35. The total spread in the rising part of this curve was about 100 V for all counters, and a working voltage of 2.35 kV was chosen. The chamber efficiency dependence on the beam position is presented in fig. 36. The arrows in this figure indicate the boundaries of a single counter.

The efficiency along the wire was measured with cosmic muons to determine the effective longitudinal dimensions of the chambers. The efficiency drops to 50% at a distance of 1.4 cm from the edge of the counter.

3.7.3. Performance of the muon chambers

A total of 218 muon chambers (1744 tubes) of seven different lengths were mounted in ARGUS. The chambers have been operated in the ARGUS data taking runs since autumn 1982. The entire system has worked in a stable and reliable manner from the beginning. The average number of hits was 0.98/event, with a low background counting rate. A typical event of the type $e^+e^- \to \mu^+\mu^-$ at a centre-of-mass energy $\sqrt{s} = 10$ GeV is shown in fig. 37. Arrows and circles indicate track impact points in the muon chamber layers.

While running, careful attention was paid to controlling all chamber components since it is impossible to estimate the efficiency from on-line studies. Distributions of hits per trigger type and a wire map were systematically checked. The readout electronics were tested with a pulse generator controlled by a computer which measured a threshold distribution for all channels. The gas quality was checked with eight proportional counters irradiated by a ^{55}Fe source.

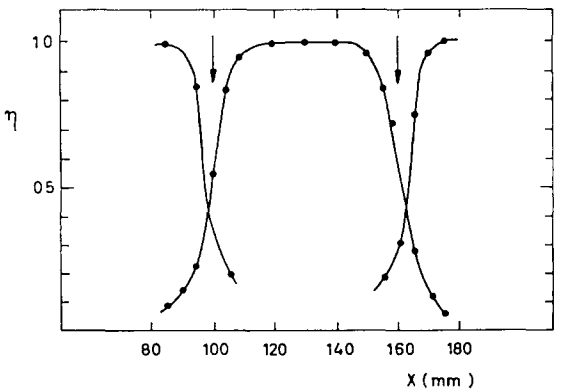

Fig. 36. Chamber efficiency as a function of the electron beam position.

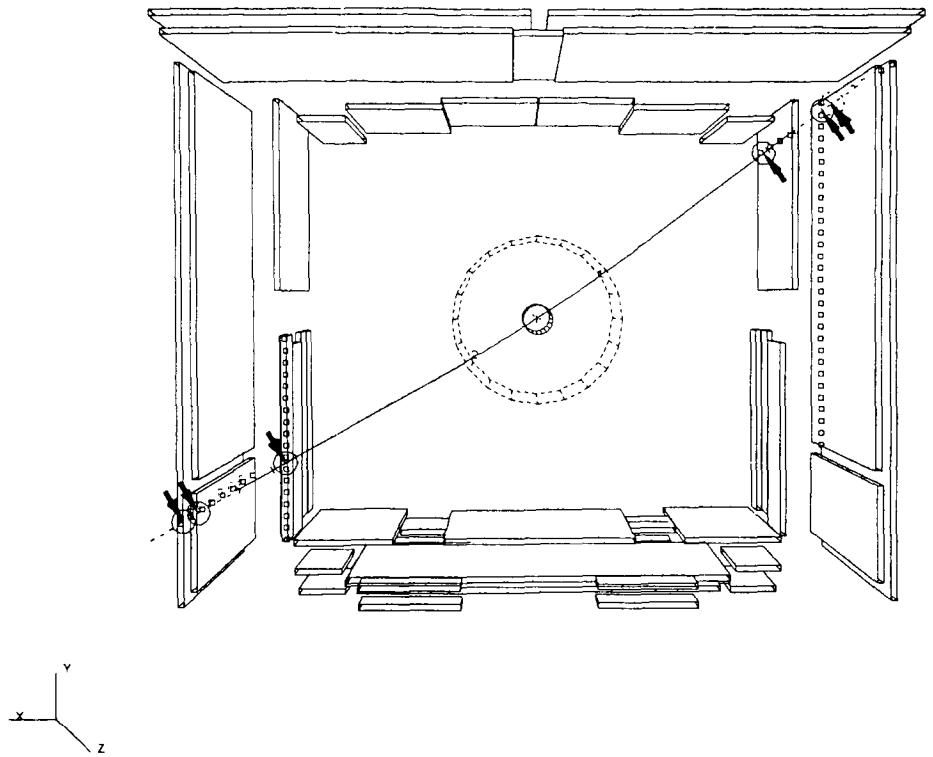

Fig. 37. A typical $e^+e^- \to \mu^+\mu^-$ event at 10 GeV centre of mass energy. Track impact points in the muon chambers are indicated by arrows and circles.

The efficiency of the muon chambers was finally determined from an off-line analysis of cosmic data where the tracks were traced from the central drift chamber to the muon detection system. The efficiency per layer, averaged over all chambers, is $\epsilon = 0.98 \pm 0.01$.

4. The ARGUS trigger system

The bunch crossing frequency of DORIS II is 1 MHz, leaving the experimenter with 1 μs time to decide whether to accept the event or not. In the case of ARGUS, this decision is broken down into two steps: A fast pretrigger discriminates between background and "good" event candidates within 300 ns, while a slower second stage trigger, the "Little Track Finder", looks at the "good" candidates and makes the final decision.

4.1. The fast pretrigger

The fast pretrigger relies entirely on the time-of-flight and shower counters. The spatial segmentation and solid angle coverage of TOF and shower counters are nearly the same. Hence, a basic trigger unit made up of a few TOF counters, can easily be combined with basic trigger units made up of a few shower counters. For the definition of trigger conditions it is convenient to divide the TOF and shower counter systems into two hemispheres, separated by the plane at $z = 0$.

The flexibility of the trigger is enhanced by creating different subtriggers. Before discussing these in detail, we describe the structure of shower and TOF counter units from which the trigger information is derived.

The shower counters are read out by photomultipliers whose output signals are summed by Split–De-

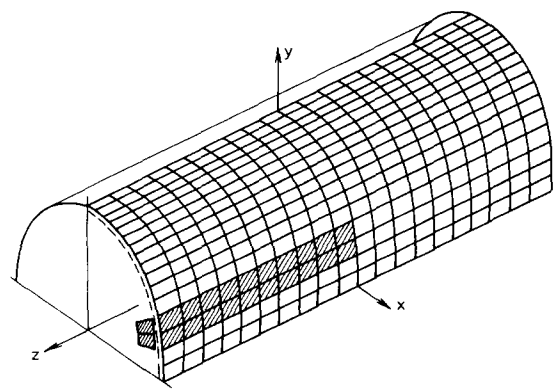

Fig. 38. Basic trigger unit (hatched) in the barrel shower counter.

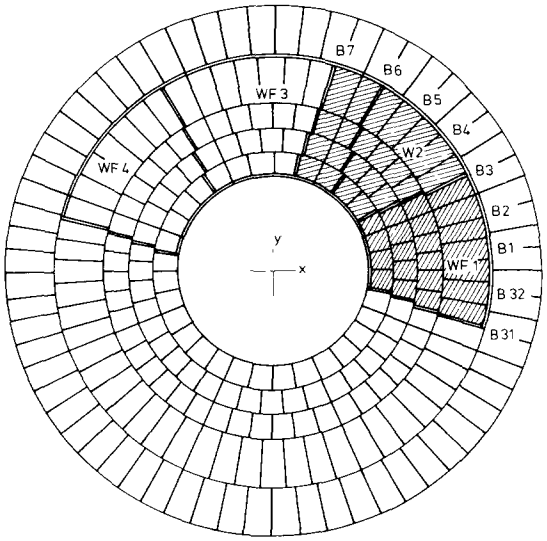

Fig. 39. Basic trigger units in the end cap shower counter (W = wedge, F = filler).

lay–Summing (SDS) units (see section 3.6.2). Each SDS unit is connected to 22 counters. In the barrel, one SDS unit covers two neighbouring rows of counters along z in one hemisphere, and the two counters of the outer ring of the adjacent end cap (see fig. 38). Each end cap is divided into 16 sectors. There are 8 "wedge" sectors with 14 counters, and 8 "filler" sectors with 8 counters each (see fig. 39). The end cap signals are used only for the total energy trigger and the online Bhabha scattering luminosity monitor. For all other triggers only the barrel signals are used. The inclusion of the end caps would lead to unacceptably high trigger rates.

The barrel TOF counters are read out by a phototube at each end. To suppress background, the coincidence of both signals from a barrel counter is required. The end cap TOF counters are each read out by one phototube. They are only used for luminosity monitoring (see section 4.3).

4.1.1. The total energy trigger

The total energy trigger (ETOT) is designed to detect events with balanced energy deposition in the shower counters (e.g. events from Bhabha scattering or $e^+e^- \rightarrow \gamma\gamma$). Only the shower counters are used (barrel and end cap). The shower energies of both detector hemispheres are summed separately. The linear sum in either hemisphere must exceed a threshold corresponding to a deposited energy of 700 MeV.

The added linear sums from both hemispheres are used for on-line measurement of the background. The rate of this signal, correlated with the bunch crossing, provides a good criterion for the running condition of the storage ring.

4.1.2. The high energy shower trigger

The purpose of the high energy shower trigger (HESH) is to detect events with single particles carrying a large portion of the total energy. It uses only the barrel shower counters. In order to find an energy deposit in a limited detector region, the signals of the SDS units are summed up in smaller groups than in the ETOT trigger. A HESH trigger group is made up of five SDS units, including one unit overlap with each neighbouring group. In total there are 16 HESH trigger groups, each covering about 70° in the azimuth. A trigger signal is generated if the signal from one HESH group exceeds a preset threshold corresponding to roughly 1 GeV.

4.1.3. The charged particle pretrigger

The charged particle pretrigger (CPPT) is designed to detect events with charged particles. It requires at least one track in each hemisphere. No azimuthal angular correlation between the tracks is required. A track is defined by the coincidence of a TOF counter group and a shower counter group which cover one another. Three SDS units, i.e. six rows of shower counters, form one shower counter CPPT group, while four TOF counters form a TOF CPPT group (see fig. 40). The shower counter group overlaps the TOF group by one row of counters on each side. This means that there is an overlap of two rows of shower counters for adjacent CPPT groups. The TOF groups have no overlap. In total, there are 16 CPPT groups per hemisphere. The shower counter CPPT group signal is preamplified and then sent to a discriminator. The threshold corresponds to an energy deposit of 50 MeV. The energy deposited by a minimum ionizing particle is approximately 160–200 MeV, ensuring an efficiency of more than 95% for these particles. The coincidence of signals from TOF

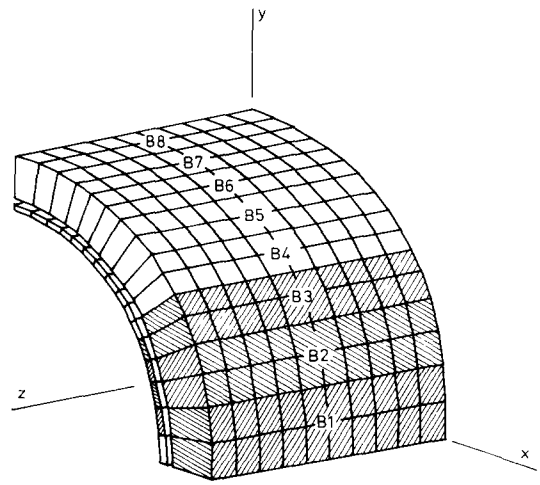

Fig. 40. CPPT group in the barrel.

and shower counters of all CPPT groups are transferred to the central CPPT unit which forms an OR of all signals from one hemisphere, and makes a final AND between both hemispheres.

4.1.4. The coincidence matrix trigger

The coincidence matrix trigger (CMT) was designed to detect tracks opposite in ϕ, but not necessarily in z, i.e. both tracks may go into the same hemisphere. Tracks are again defined by coincidences of TOF and shower counter CPPT groups in the barrel. This is an important trigger for events from $\gamma\gamma$ interactions, which, although being boosted along the z-axis, often have balanced transverse momentum.

Since it is not necessary that tracks originate in different hemispheres, CPPT groups at the same azimuthal angle ϕ are OR − ed. This leads to a set of 16 channels, each channel containing the information as to whether there is a track in a certain ϕ region, regardless of the z-coordinate. These 16 channels are fed to the "rows" and "columns" of a 16×16 coincidence matrix unit whose elements can be "programmed" in hardware in such a way that coincidences between a column and an arbitrarily selected group of three, five, seven, or nine rows are established. Typically, the CMT is programmed to require a track in one out of seven CPPT groups opposite in ϕ with respect to a given group. The flexibility of the CMT allows for changes in the trigger conditions without making major hardware changes.

4.1.5. The test triggers

In order to test and calibrate various detector components when the storage ring is not operated, a cosmic trigger was installed. It uses only the information from the barrel TOF counters. To trigger on cosmic muons which travel close to the beam line, a coincidence is required between two opposite groups of four TOF counters. The information from these eight combinations is provided to an OR which delivers the trigger signal.

Another test trigger gives a random gate with a rate of 0.1 Hz to all electronics. It has been installed to estimate the random noise contribution to ARGUS events.

4.1.6. The pretrigger collector

All pretrigger signals, except the one from the cosmic trigger, must be in coincidence with the bunch crossing signal delivered by the storage ring. In addition, a so-called "trigger ready" signal must be present. This signal is removed as soon as a pretrigger is accepted, thus inhibiting the pretrigger logic during event processing. The "trigger ready" signal is restored either by the second state trigger if the minimal trigger requirements are not fulfilled (see section 4.2), or by the online computer after all processors have been read out and reset.

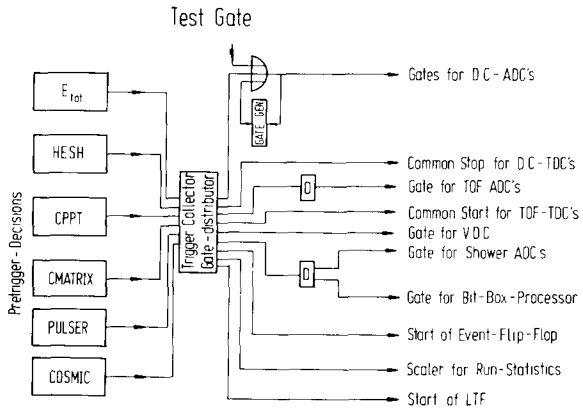

Fig. 41. Diagram of the fast trigger logic.

The trigger collector comprises a switchable OR of all pretriggers and a fan-out to all digitization components, providing START/STOP signals for TDCs and ADC gates (see fig. 41). The exact timing is determined by the bunch crossing which has a time jitter of less than 50 ps. There are timing differences introduced by the fan-out of the bunch crossing signal to the different pretriggers. The correction of these is discussed in section 3.5.2.

4.1.7. The trigger monitor and trigger tester

At all levels, the digital trigger signals are fed to input registers which are read out with each event. This allows a proper monitoring of all digital trigger components, and a software calibration of all thresholds.

The proper operation of all trigger components is checked periodically (< 8 h) by programmable test signals with adjustable pulse heights to all SDS units and to all split-and-delay units of the TOF system.

4.2. The slow trigger ("Little Track Finder")

The slow trigger or "Little Track Finder" (LTF) is the second stage of the ARGUS trigger system. It is an electronic device which is started by the pretrigger. It is capable of finding and counting circular tracks passing through the interaction point in the r–ϕ-plane of the detector, by examining data from the main drift chamber and the TOF counters. If the number of such tracks exceeds a preset threshold, which may depend on the pretrigger type, the event is selected for readout by the online computer. Otherwise the detector is reset so as to be ready for a new event. A detailed description is given in ref. [28].

The design of the LTF is largely determined by deadtime considerations. The operation time of the LTF must not introduce more than a few percent deadtime into the data taking process. With a mean pretrigger rate of 100 Hz and allowance for 1% deadtime

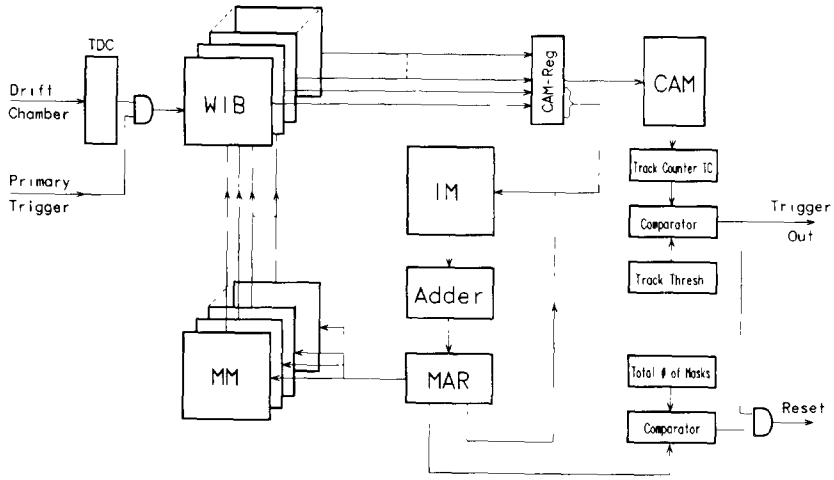

Fig. 42. Layout of the second stage trigger ("Little Track Finder"). The abbreviations are explained in the text.

an acceptable processing time would be 100 μs. This ruled out a pure microprocessor application, but a pure hardware solution was also rejected because of its inflexibility and clumsiness. To compromise between the speed of a hardwired system and the flexibility of a programmable processor, the LTF was built as a table driven ECL device connected to the on-line computer for software support. The tables that control the operation of the LTF are prepared by running a FORTRAN program on the on-line computer, once for each major data taking period. The program requires simple physical input information, and is flexible enough to cope with different experimental requirements. The lookup tables are loaded into memories of the LTF by the online computer which is now able to perform high speed operations without the further intervention of the computer. In this way the flexibility of a software solution and the speed of a hardware device could be combined.

Drift chamber and TOF cells in the detector ARGUS are organised in cylindrical layers. In the r–ϕ-plane of the detector a good track is, then, characterized by a well defined sequence of drift chamber and TOF cell hits, with at least one entry per layer. The loaded memories of the LTF contain a complete list of all possible "roads" (or masks) of good tracks in the detector. The LTF sequentially scans this list, compares its entries to the actual contents of the detector cells, and counts coincidences as found tracks.

The layout of the LTF is shown schematically in fig. 42. There are four types of internal memories:

(1) There is one wire input board (WIB) for each drift chamber layer and one for the TOF layer. The wire input boards are connected to hit-registers within the TDC modules of the drift chamber and TOF layers, and hold the hit information of the actual event. The drift time information is not used because of the small size of the drift cells (18.0×18.8 mm^2).

(2) The mask memory (MM) is loaded from the online computer with precalculated information. It may contain up to 2000 masks. Each mask consists of a sequence of words, as many as there are layers connected to the LTF. These words contain the addresses of wires in the wire input boards, computed so that together they constitute a road for possible good tracks in the detector.

(3) The content addressable memory (CAM) of 64 words is preset with fixed information from the on-line computer, and contains acceptable hit patterns for good tracks. To account for drift chamber inefficiencies there may also be good tracks with one or two hits missing.

(4) The increment memory (IM) is loaded with calculated information from the computer.

The sequence of operations is as follows: Each primary trigger initializes the LTF and strobes the contents of the hit registers into the wire input boards. Then a series of mask cycles is executed. The words belonging to one mask are used in parallel to address wires in the wire input boards, and the hit pattern is compared to the content addressable memory. If there is a match, the track counter is incremented. If it exceeds a preset value, the event is accepted. The preset values depend on the pretrigger type. The standard setting requires two LTF tracks for the CPPT and CMT trigger, one for the HESH and none for the ETOT trigger. If the track counter does not exceed the threshold and the end of the mask memory is reached, a reset signal is sent to the detector electronics, and after some delay the "trigger ready" signal is restored.

One mask cycle, consisting of 8 subcycles, takes 170 ns. Going through 2000 masks sequentially would mean an operation time of 350 μs. This time can be substan-

tially reduced by a simple trick. One single wire (or group of wires) participates in many masks. Once it is determined that this wire has not been hit, there is no point in checking the rest of the masks containing this wire. With a suitable ordering of masks, it is possible to skip useless cycles by letting the mask address incrementation depend on the result of the previous mask cycle. The incrementation control is affected by the contents of the increment memory. The operation time of the LTF then depends on the number of hits in the drift chamber. For an empty drift chamber the operation time is 12 μs. Each track element encountered adds another 4 μs to this time. The measured mean operation time of the LTF during normal detector running is 20 μs, more than an order of magnitude less than in the strictly sequential mode.

The information about an event, obtained by the LTF, is stored in one of its memory blocks. This contains the total number of tracks observed and the bending radius, ϕ-angle and hit pattern of each track. If the event is accepted, this data block is read by the on-line computer and added to the event record for further use in fast software filter routines.

Compared to the primary trigger, the LTF reduces the trigger rate of ARGUS by an order of magnitude, if two tracks are required in the drift chamber. In doing this it introduces less than 0.2% deadtime into the detector operation. Its track finding efficiency has been measured to be 97%, mainly determined by the drift chamber efficiency. Double counting of a single track is reduced to 3% by ignoring the second one of two consecutive matches in the track finding process. The LTF can be tested easily and thoroughly by online computer programs, since all of its registers can be accessed via CAMAC.

4.3. Luminosity monitoring

Luminosity determination in electron positron colliding beam experiments is usually performed by counting Bhabha scattering events within a certain polar angle interval. Since the cross section for this pure QED process is well known, the luminosity can be determined from the relationship

$$\mathrm{d}N_{\mathrm{Bhabha}}/\mathrm{d}t = L\sigma_{\mathrm{Bhabha}}. \tag{15}$$

ARGUS has an on-line luminosity monitor which allows the operator on shift to estimate the amount of data being taken. Moreover, a quick luminosity measurement provides valuable information on the machine performance and allows for a fast feedback to the machine personnel.

The ARGUS on-line luminosity is determined from the fast trigger electronics. In each end cap, 16 overlapping groups of shower counters are defined by combining each "wedge" sector with either of its neighbouring "filler" sectors (see section 4.1). The linear sum from such a group must exceed a threshold corresponding to an energy deposit of ≈ 1 GeV. The 48 TOF counters covering an end cap calorimeter are divided into 16 groups of three counters each. The TOF group signal is the logical OR of the three counter signals. The signal from a shower counter group must be in coincidence with the signal from the TOF group in front of it. A Bhabha count is recorded if there are coincident signals from one group and its "diagonal" counterpart in the opposite end cap, i.e. the azimuthal difference of these two groups is required to be 180°.

The TOF counters define the acceptance for Bhabha events. Since one sector is defined by three TOF counters, a hit in one counter of one sector must match a hit in one out of the three counters defining the opposite sector. The solid angle coverage of the end cap TOF counters results in a Bhabha scattering cross section of

$$\sigma_{\mathrm{Bhabha}} = 58\ \mathrm{nb}\frac{100\ \mathrm{GeV}^2}{E_{\mathrm{CM}}^2}.$$

Under normal running conditions this corresponds to a rate of 1–2 Hz. The Bhabha counts are delivered to the online computer and converted into events/nb for the operator's convenience. Long-term systematic variations due to changing hardware efficiencies and background conditions are of the order of 5–10%.

The off-line luminosity determination is based on fully reconstructed Bhabha scattering events recorded in the barrel region of the detector ($|\cos\theta| \leq 0.748$). A track is accepted if its momentum exceeds 1 GeV/c, and the energy deposited in the calorimeter exceeds 0.6 GeV. The two tracks in a Bhabha event must have an opening angle larger than 165°.

The total cross section for Bhabha scattering, including initial and final state radiation effects, depends on the experimental cuts. It can be calculated by means of Monte Carlo techniques [29]. For the above cuts it turns out to be [30]

$$\sigma_{\mathrm{Bhabha}} = 11.8\ \mathrm{nb}\frac{100\ \mathrm{GeV}^2}{E_{\mathrm{CM}}^2}.$$

With this value the number of observed Bhabha scattering events can be converted into an integrated luminosity. The systematic uncertainty on the luminosity determined according to this procedure is about 3%.

Recently, the algorithm for luminosity determination has been improved by decreasing its dependence on the drift chamber track efficiency which deteriorates slowly with time [7]. In addition, the Bhabha scattering cross section on the Υ resonances was studied in more detail. The cross section for the new algorithm is

$$\sigma_{\mathrm{Bhabha}} = 11.38\ \mathrm{nb}\frac{100\ \mathrm{GeV}^2}{E_{\mathrm{CM}}^2}.$$

The systematic error of this luminosity is 1.8%, except in the region of the $\Upsilon(1S)$ resonance (9460 ± 15 MeV) where it is $^{+1.8}_{-2.5}$%. This luminosity will be used for future analyses.

5. On-line data acquisition

5.1. Electronic readout and data transfer by the PDP computer

5.1.1. General hardware configuration

The hardware for the on-line data acquisition system consists of the four major components shown schematically in fig. 43.

The various detector components of ARGUS deliver their data and control signals to digitization and storage modules in a CAMAC system. The readout of data from these modules and the construction of the complete event record is performed by a fast microprocessor ("CAMAC booster" or CAB), coupled via CAMAC to the on-line computer, a DEC PDP 11/45. The PDP receives the data on an event-by-event basis and transfers them to the VAX 11/780 which sends them, after extracting monitoring information, to the IBM main computer. There is a second IBM channel from the PDP which is used only if the VAX transfer system is out of operation. The PDP controls all calibration procedures for the hardware components of the detector, and allows an operator, through a set of menus on the terminal, to manually steer and manipulate the on-line process. In addition, the PDP monitors the most important operating parameters during data taking. Hence an immediate check of the raw data quality is possible, either automatically or by the shift operator.

5.1.2. The CAMAC system

Data collection from the various detector components in ARGUS is performed by CAMAC modules (ADCs, TDCs, registers, etc.). The large number of data channels requires the readout of many CAMAC crates. To facilitate this the CAMAC system is coupled to the online computer by a so-called system crate interface *. The system crate (see fig. 44) contains the interface modules which establish the connection to the PDP via UNIBUS, and the system crate controller **. The system crate controller controls all of the normal modules in the crate according to commands received via the system dataway. It allocates usage of the system dataway to requesting program units, selects branch couplers, and controls branch operation timing when a program unit requests a branch operation.

Interrupt requests from the CAMAC system are handled by an interrupt vector generator ***. This unit encodes the LAM pattern and the branch code, forming an interrupt vector which is trapped and passed to the host computer. In this way it is possible to activate PDP programs from a multitasking wait state directly by interrupts from various CAMAC modules. This is also done by the direct memory access (DMA) module + at the end of a data block transfer. This module is capable of transferring 16- or 24-bit words up to a block size of 4 K words at a rate depending on the memory cycle time of the UNIBUS and the CAMAC operation time in the system crate (in our case roughly 3 μs).

The entire CAMAC crate system is interfaced to the system crate by a branch coupler ++. The branch highway of the system crate ends in an "intelligent" crate controller (CAB, see next section) and is distributed via programmable CAMAC branch drivers +++ to the final three branches which accommodate the CAMAC modules for the detector components (see fig. 44). This configuration is necessary because the CAB is designed to operate not only as a transparent crate controller, but also as an independent processor that performs the data readout. The latter requires that it be able to address all crates. Hence, the branch fan-out must be located after the CAB, and cannot be placed within the system crate.

* GEC–Elliott Process Automation Ltd.
** GEC Model MX-CTR-3.
*** GEC Model IVG 2404.
\+ GEC Model AMC-11.
++ GEC Model BR-CPR-3.
+++ Kinetic Systems Model 3991.

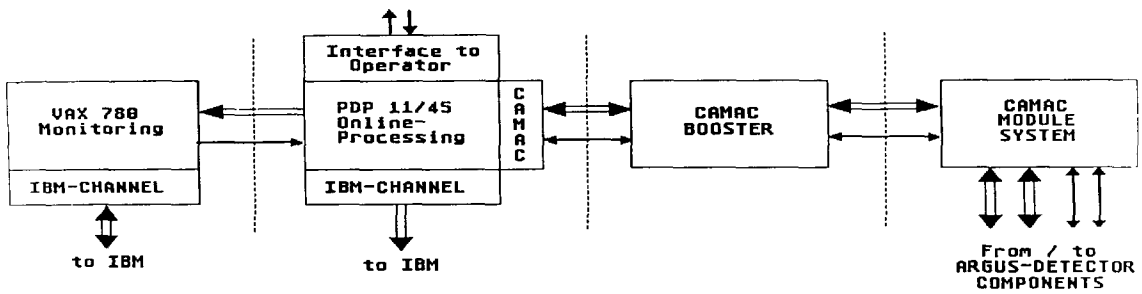

Fig. 43. Schematic diagram of the data acquisition hardware structure.

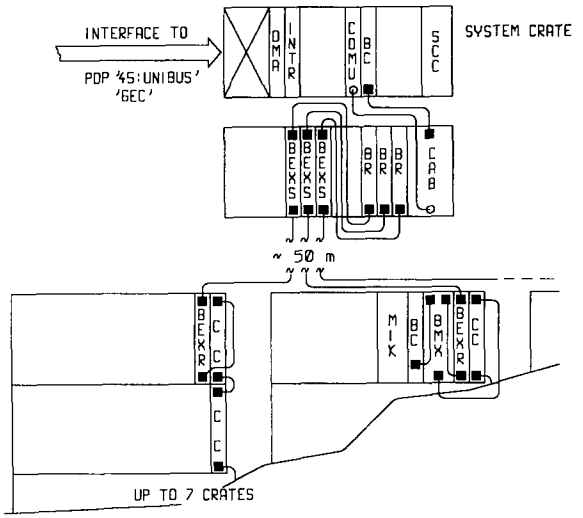

Fig. 44. CAMAC system crate configuration. SCC: system crate controller, BC: branch coupler, COMU: communication module, INTR: interrupt vector generator, DMA: direct memory access module, CAB: CAMAC booster, BR: branch driver, BEXS/BEXR: branch extenders, CC: CAMAC crate controller.

Thus, the host computer can address the entire CAMAC system, while the CAB can address the system on the level below the system crate. In order to synchronize the CAMAC activities of host computer and CAB, a communication module was installed in the system crate. The CAB requests CAMAC access by sending a signal to the communication module, which generates an interrupt in the PDP.

The system crate and CAB crate are located close to the PDP, while the crates comprising the branch system are about 50 m away. It is therefore necessary to amplify the branch highway signals using differential branch extenders *. Two such extenders are required for a single link. Both modules transmit data in both directions, but for control signals one acts as a transmitter and the other one as a receiver (see fig. 44).

5.1.3. The CAMAC booster

Deadtime is the keyword for data acquisition systems. There are, in principle, two ways of keeping the deadtime small: reduction of the event input rate, and reduction of the read-in time for the event by the online computer. For ARGUS we have followed both ways: The event input rate is considerably reduced by the Little Track Finder (see section 4.2), while the CAMAC booster efficiently reduces the event read-in time.

The CAMAC booster ** (CAB) is a fast 16-bit bit-slice processor configured to be a CAMAC crate controller. It has an instruction execution time of 200 ns, 4 k of 16-bit RAM data memory, 4 k of 24-bit instruction memory, 16 internal registers, and a large instruction set.

The CAB is responsible for the complete readout procedure from 16 data sources. It can perform this job in 1.2 ms. After that time the complete event is in its final format, and checks have been performed on the format of all data words.

Each CAMAC command must pass through the CAB and must specify the destination address in the branch driver before a data transfer can take place. Commands with station number $N = 31$ act directly with the CAB, commands with other station numbers are transferred via interrupts to special entries in the CAB program memory. The CAMAC activities of host computer and CAB are synchronized by means of a communication module (see section 5.1.2).

A cross-assembler, linker/loader and debugger/tester for the CAB software was adapted for the PDP system software. A download procedure for the CAB software is included in the boot file of the PDP operating system and in the user task system. The CAB software includes a transparency program and several special routines. One of these routines is the task responsible for the data readout. This task is triggered from the host computer by a CAMAC command and performs the complete event readout and formatting. Between two CAMAC commands, there is time to perform 2 to 3 CAB instructions. This time is used to perform checks on the format of each data word. The event is formatted into its final structure and stored in the CAB memory so that one DMA transfer can send it to the host computer.

The implementation of the CAMAC booster system reduced the processing time per event (one event has on average one thousand 16-bit words) from about 40 ms to about 3 ms (1.2 ms for the CAB, the remainder for DMA transfers to the host and VAX computers, and for synchronization). Under these conditions, the detector can be run with input rates around 5 Hz with a deadtime of less than 5%.

5.1.4. The on-line computer

The on-line computer that runs the ARGUS data acquisition software is a DEC PDP 11/45 with a 128 k words of memory, a memory management unit, and a hardware floating point unit. External storage is available on two 5.2 Mbyte disks and two CDC 3400 disks with 67Mbyte capacity. The input/output devices for IBM, VAX, and CAMAC connections are connected to the UNIBUS. The PDP runs under the multiuser/multitasking operation system RSX-11-M V3.2.

The on-line software consists of different autonomous programs which are synchronized to the incoming raw data flow from the various detector components.

* GEC Model DBE 65701.

** Model 4801 CABC using AMD 2901 arithmetic logic unit, LeCroy, Geneva, Switzerland.

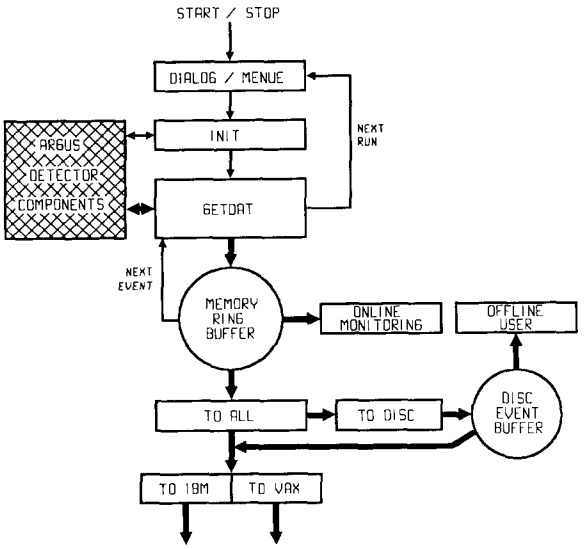

Fig. 45. Flow chart of the on-line data taking program.

The synchronization is done by a supervisor program which is responsible for servicing, scheduling and dispatching all software activities of programs that operate the detector. Each program has access to a permanent memory region which contains a set of readable and writeable parameter lists that control the different online tasks. All parameters can be examined and modified by the operator via a set of menus.

The complete events, prepared by the CAB (see section 5.1.3) in their final format, are stored in the PDP in a dynamically created ring buffer. From this buffer, the events are distributed to disk, to the IBM, or – as is the normal case – to the VAX. The ring buffer is used as fast storage to buffer peak input rates and to synchronize the outgoing event flow to the VAX.

In addition to setting the parameters for processing the data flow (see the flow diagram in fig. 45), the menu task is used to call and control all on-line calibration procedures during breaks of data taking. These include TOF and shower counter calibration (see section 3.5.3 and 3.6.3), drift chamber ADC and TDC calibration, and test procedures for the trigger and track finder electronics.

5.2. On-line monitoring and data transfer by the VAX computer

5.2.1. General description

For an experiment with the complexity of ARGUS, comprehensive on-line monitoring of all detector ele-

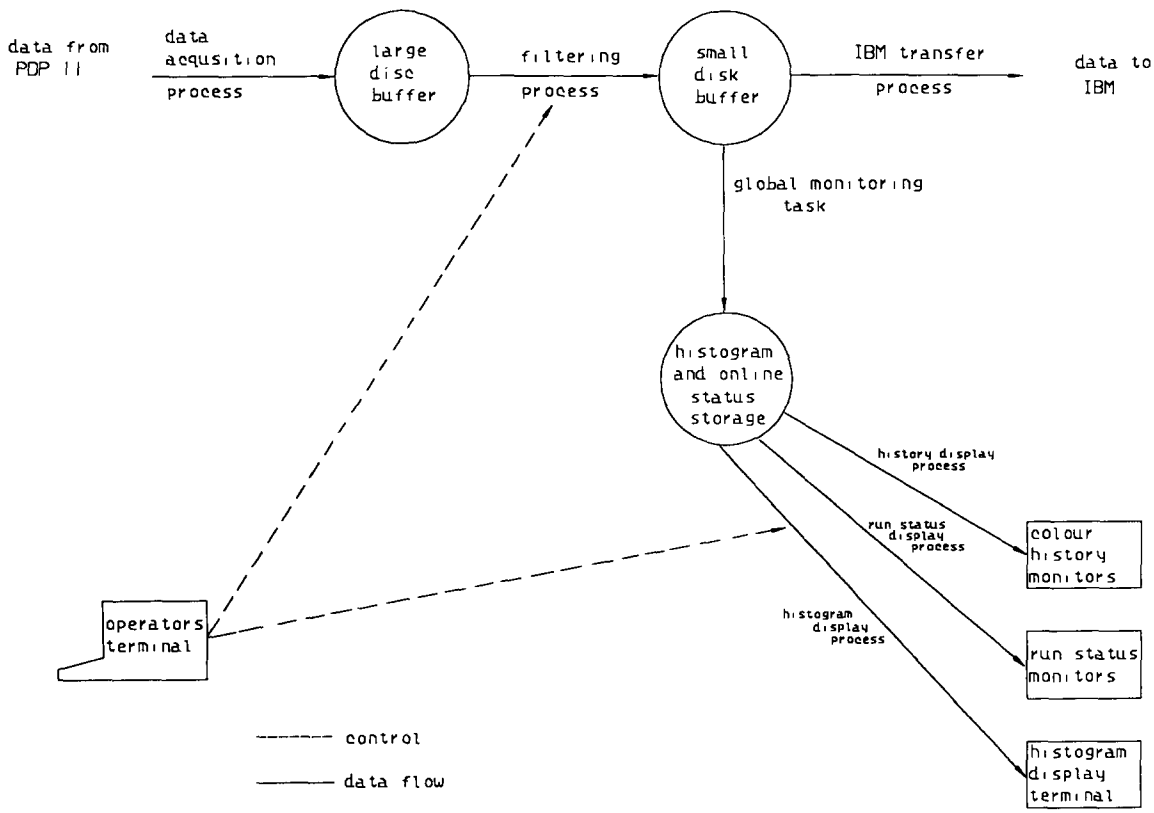

Fig. 46. Flow chart of the VAX monitoring software.

ments is extremely important in order to maintain the quality of the data collected. This requirement can be satisfied by accumulating, in real time, histograms describing the performance of the detector. Human observation of the histograms allows possible variations in, or failures of the experimental apparatus to be detected and compensated for. The limited memory and processing power of the PDP 11/45 led to the decision to use a VAX 11/780 as the computer for on-line monitoring.

The organization of the software for on-line monitoring on the VAX is in terms of multiple detached processes, under the control of a master process (see fig. 46). The code is written almost entirely in FORTRAN, and includes only a small amount of assembly language.

The VAX runs the DEC VMS operating system which provides the essential features for interprocess communication. This communication occurs primarily through the use of "common event flags" and "global sections". Common event flags are flags which may be set and tested by different processes and serve to provide synchronization. As an example, if a certain process A must wait until another process B has completed some task, it might enter a wait state until a common event flag is set by process B, it would then reset the flag, carry out its function, and re-enter a wait state. Global sections are areas of memory which are shared among processes. They provide a method of transferring data between processes. The most important global sections in the ARGUS on-line monitoring system are a ring buffer (a buffer with the first and last bytes identified) which contains data from the PDP to be studied and then sent to the IBM mainframe, a histogram section which contains all the histograms collected to monitor detector performance, and a run status section which contains continuously updated information on trigger rates, numbers of events transferred, integrated luminosity, etc.

The master controlling process creates the global sections, performs initialization tasks, and creates the detached processes. Some of these processes are responsible for handling the transfer of data from the PDP and to the IBM, while others are principally concerned with the accumulation of real time information about the detector. A menu is presented which allows the operator to display histograms and events, to obtain hard copies, to clear histograms, and to influence various aspects of the histogram collection. The detached processes, once created, are capable of running without user intervention, and in fact, the master controlling process can be stopped to allow other actions, and then resumed with no interference with the data transfer or monitoring.

5.2.2. Data flow

The events read from CAMAC are stored in the PDP 11/45 computer and sent to the VAX via two back-to-back DR11-W parallel links. Each event has a fixed length of 8 kbytes and is sent from the PDP to the VAX by a direct memory access transfer. This mode of operation allows transfer rates of about 0.6 Mbytes/s and easily handles the typical ARGUS trigger rate of about 5 Hz. In the VAX, the event format is changed from fixed to variable length records. These are stored in a large disk buffer which can contain about 4 h of data. It is also possible to save data on another disk in the event of a prolonged failure of the IBM, which, though, must eventually receive all data. The connection to the IBM is via the DESY PADAC system which consists of fast serial links. The IBM communicates with several experiments, via PADAC, one at a time in a time-sharing fashion, so it is important to transfer as much data as possible whenever the link is available. In the ARGUS experiment, data is sent in blocks, each of about 20 events. This leads to high effective transfer rates with essentially no deadtime.

5.2.3. Monitoring

Recall that events are stored on the VAX in a ring buffer which is a global section, accessible to several processes. It is the job of a "global monitoring task" to read events from this buffer, unpack the data, and accumulate histograms in another global section to be made available to the user of the monitoring system. Another task is responsible for gathering data for the run status section, referred to above.

Many histograms are accumulated, the following should be considered as merely a brief summary. For the drift chamber, histograms consist mainly of wire maps with hit frequency, mean pulse height, and mean drift time for all sense wires. These make it possible to rapidly identify the failure of any group of ADCs or TDCs. More detailed histograms which are not normally accumulated due to time and space constraints may be requested by the operator. Mean values are available to facilitate the detection of changes in overall chamber operation. The vertex drift chamber is handled in a similar fashion. The shower counters are monitored with hit frequency and pulse height recorded for each counter. Hit maps, mean pulse height maps, and mean time maps are accumulated for the time-of-flight counters, and hit frequency maps are accumulated for the muon chambers. A histogram is accumulated to record errors in the unpacking of data. The Little Track Finder is monitored, and a frequency distribution of the found masks is kept which is useful in indicating possible failures. There is, in addition, a high resolution colour display of drift chamber hits, TOF hits, and LTF masks found, which provides a useful diagnostic tool. The trigger is monitored in some detail, providing a sensitive on-line picture of the storage ring background conditions.

The run status section contains information about event transfers, trigger rates, and other useful data. This information, together with warnings in the event of online process failures or filling up of the event buffer in the VAX, is displayed on a separate terminal reserved for this purpose. The high resolution colour monitor provides a history over the last 24 h of the rates of the charged particle pretrigger, the total energy trigger, and of the specific luminosity. Information about the failure of critical VAX processes will also appear on this monitor.

5.3. Data storage at the IBM main computer

The data are transferred from the VAX to the IBM and are written to a disk data set. This data set can store about 40000 events. When the disk fills up, the data are automatically dumped onto a tape. During the dump job the final record format is created, and some monitoring is done for the drift chamber, the shower counters, and the muon chambers. Finally, every two of these tapes are copied together to EXDATA tapes. The laser and pulser events are copied onto the MONITOR file, and new entries in the RUNFILE, which contains information on individual runs, are made. The raw data EXDATA tapes are stored permanently and serve as input for the off-line data analysis which also uses the MONITOR file and RUNFILE. The analysed events are written onto data summary tapes, the EXPDST tapes. These events must have at least two tracks pointing to the vertex region, or they must be recognized as of the type $e^+e^- \to e^+e^-$, $e^+e^- \to \gamma\gamma$, or $e^+e^- \to \gamma\gamma\gamma$ (see also section 6.1.3). In the same step the RUNFILE is updated.

5.4. Static monitoring

In order to determine the behaviour of the detector during data taking, a static monitoring system was installed to watch those components which are expected to work continuously, e.g. magnet current, high voltages and electronics supply voltages.

This task is performed by a system of data collection and control modules which is supervised by a minicomputer MIK 11/2S. During data taking all quantities of interest are continuously measured. The actual values are compared to nominal values. Any deviation larger than some specified tolerance causes an alarm to occur. Depending on the alarm level, data taking is either stopped, or a warning is issued.

An alarm is communicated to the operator visually and acoustically by a main alarm panel, which also indicates roughly the reason for the alarm. In addition the defective component is indicated on the screen of the monitoring computer. In most cases the problem can be quickly localized and cured.

The following quantities are continuously watched by this monitoring system:

- The high voltages of the vertex drift chamber, main drift chamber, shower and TOF counters, and muon chambers;
- the currents drawn by the vertex drift chamber, the main drift chamber and muon chambers;
- the low voltage supplies of CAMAC and NIM crates, and of preamplifiers;
- the temperatures at various points of the magnet, the compensation coils, the main drift chamber, and the vertex drift chamber;
- the current in the ARGUS magnet and in the compensation coils;
- the main drift chamber gas pressure; and
- the drift chamber gas quality.

6. Data analysis and Monte Carlo simulation

6.1. Pattern recognition strategy

The aim of pattern recognition is to determine the number of charged particle tracks and their approximate geometrical parameters. In a second step a track fit is performed. In the procedure used by ARGUS, each hit wire is uniquely associated with a track, or declared background. The pattern recognition strategy optimizes the track finding efficiency, while satisfying the requirements essential for the physics aim of the ARGUS experiment. The most important of these are:

(1) In many physical processes, e.g. in D* decays, particles with extremely low momenta are produced. The program must be well tuned for tracks which curl up in the magnetic field within the drift chamber.

(2) Secondary particles from the decays of K^0's and Λ's, or from the conversion of photons, must be reconstructed with the same efficiency as particles originating from the interaction vertex. In contrast to many other pattern recognition procedures, the ARGUS procedure is isotropic in the plane perpendicular to the beam axis (which is referred to as the x–y-plane), i.e. it does not prefer those tracks pointing to the symmetry axis of the drift chamber, to the cost of tracks which do not.

(3) The ARGUS pattern recognition program is used as an efficient and reliable event filter: The number of tracks pointing to the interaction region must exceed a certain limit (normally: two) for an event to be accepted. Almost all events are processed by this program, and minimum time consumption is imperative.

These requirements are fulfilled by taking advantage of the following features of the ARGUS detector and its drift chamber:

(1) The magnetic field is approximately homogeneous. The inhomogeneity is taken into account in the last step of the drift chamber analysis only, in the track fit.
(2) The chamber is homogeneous in the x–y-plane, i.e. the density of wires and the shape of the drift cells is the same everywhere, and there is no empty space. As a consequence, the average distance between two adjacent wires on a track does not depend on the track's angle. This seemingly peripheral feature turns out to be a most important one upon which almost every part of the analysis depends. As an example, this homogeneity is a necessary precondition for the efficient reconstruction of particles coming from decay vertices. The sequence of paraxial and stereo wires, described in section 3.3.1, should be kept in mind when considering the procedure sketched below.
(3) The lines of equal drift time around each wire, the isochrones, are, to a very good approximation circles. This feature is one aspect of the homogeneity mentioned above. It allows for very simple formulae in geometrical calculations, and thus saves computer time.

6.1.1. The parameter set

A particle travelling with constant velocity in a homogeneous magnetic field parallel to the z-axis follows a helix which is described by specifying five parameters at a uniquely defined reference point. The reference point is usually chosen to be the track point which, projected into the x–y-plane, is closest to the origin. A convenient set of parameters is:

κ = curvature of the helix or the inverse of its bending radius R, multiplied by a sign factor described below;
d_0 = distance between the origin and the reference point defined above, measured in the x–y-plane, also multiplied by a sign factor described below;
ϕ_0 = azimuthal angle of the track tangent at the reference point defined above;
z_0 = z-coordinate of the reference point defined above;
cot θ = cotangent of the angle the track makes with respect to the z-axis.

The first three parameters describe a circle which is the projection of the helix onto the x–y-plane. Information about these parameters comes from paraxial as well as stereo wires, whereas information regarding z_0 and cos θ can be obtained from stereo wires only. Note that the parameters commonly used for circles, x_{centre}, y_{centre}, and R, are less appropriate due to their discontinuous behaviour for approximately straight tracks. The relation between the two parameters sets is:

$$\kappa = Q/R, \tag{16}$$

$$d_0 = Q\left(R - \sqrt{x_{\text{centre}}^2 + y_{\text{centre}}^2}\right), \tag{17}$$

$$\tan \phi_0 = \frac{x_{\text{centre}}}{-y_{\text{centre}}}. \tag{18}$$

The sign factor $Q = \pm 1$ can be conveniently chosen as the particle's charge. It must reverse its sign whenever the magnetic field or the particle's movement reverse their direction.

6.1.2. Search for track candidates in the x–y-plane

Track reconstruction consists of two steps: (a) the search for tracks in the x–y-plane, and (b) the completion of the reconstruction by adding the cos θ and z information. The first step of the pattern recognition strategy, the search for tracks in the x–y-plane, will now be described in some detail. The main features of this strategy are the same in the second step, the three-dimensional reconstruction.

At this stage, only paraxial wires are used. This is the only part of the program designed to recognize and establish new tracks. Each reconstructable track candidate must be considered, leaving it to subsequent program parts to perform rejection of background tracks.

The drift time information is used from the very beginning in the track reconstruction procedure. Most of this procedure can, however, be explained more easily assuming that drift times are not measured. In this simplified case, the only information available consists of points in the x–y-plane defined by the positions of the hit wires. The patterns that are searched for are circle segments going through these points.

The minimal element defining a circle and hence a possible segment of a track is a triplet of hits. The procedure of the pattern recognition program is based on combining and extending sequences of these basic elements until a complete track is reconstructed. For each triplet, the curvature κ is determined and stored together with information on the geometrical positions of the contributing wires.

A single triplet does not yet contain any information on whether its hits actually form a track candidate or not. As a minimum requirement a matching fourth hit must be found. For this, two of the initial three hits and a new one are combined, and the curvature of the newly formed triplet is calculated. If the difference in κ between the initial and the new triplet is sufficiently small, the two triplets are assumed to belong together and to form a track candidate. The average of the two curvatures is calculated and stored. In a similar way, a fifth and any following hit can be assigned to a track candidate. In these cases, a new triplet is formed by combining the new hit with two hits that were assigned earlier to the track candidate, and the new value κ is compared to the average value calculated before.

In other words: The ARGUS pattern recognition procedure performs a projection of the two-dimensional

problem (geometrical space) or, more accurately, of the three-dimensional problem (space of the circle's three parameters), into the one-dimensional space of the parameter κ upon which all decisions in this step of the program depend. The remaining parameters ϕ_0 and d_0 are ignored in this stage. A continuous behaviour with respect to them is automatically maintained by the method described above, which links subsequent triplets of a track candidate, while requiring them to have always two hits in common.

Not all combinations of any three hits within the drift chamber must be analysed. The selection of real track candidates is achieved mainly by using a so-called local pattern recognition strategy which, for the ARGUS program, means that an attempt to combine hits is made only if they are sufficiently close to one another. A gap of empty or non-useful drift cells between two neighbouring hits is allowed, but this gap must not be larger than a certain limit (normally: three cells).

Let us now consider the real case where the drift times and hence the distances between wires and track candidates are taken into account. The particle trajectory is a segment of a large circle which is tangent to many small circles, representing the isochrones around the hit wires. It is a priori not known whether the track passes a wire on the left or right side and, consequently, two possibilities per wire must be taken into account. Each ambiguity gives rise to a different value of κ all of which must be calculated. Most of the wrong choices of the left–right ambiguity can be rejected immediately, because they lead to curvatures which do not fit to the rest of the track, a consequence of the homogeneity of the ARGUS drift chamber. In other cases, both curvatures must be stored.

A substantial improvement in rejecting wrong track candidates is achieved by cutting on χ^2-like quantities rather than simply comparing values of κ. The decision about whether a new wire is to be assigned to a track candidate or not, is made on the basis of the quantity

$$\chi'^2 = \frac{(\kappa_{\text{new}} - \kappa_{\text{old}})^2}{\sigma_{\text{new}}^2 + \sigma_{\text{old}}^2}, \tag{19}$$

which is required to be less than 25. The indices "new" and "old" refer to the triplet containing the new wire and to the average values obtained from all previous triplets. The error in the curvature, σ, depends on the relative position of the three wires and on the errors on the measured drift times which, in turn, are functions of the drift times themselves. For different configurations, these errors may vary by as much as one order of magnitude.

The pattern recognition strategy described so far has the advantage that it allows for a program which, in general, handles each wire only once, or, in terms of computer language, which consists of a single loop over all hit wires. This fact minimizes the time consumption of the ARGUS pattern recognition program.

The program starts in the outermost layer where the conditions are expected to be cleanest, and ends at the innermost layer. Within each layer, the hit wires are stored according to their azimuth. For each wire processed in this sequence, an attempt is made to associate the wire with tracks which have already been established. By using the strategy described above, this is done by trying to find a triplet which consists of the new wire and two wires already associated with the track.

After trying to extend tracks, the program looks for new tracks by trying to establish further initial triplets. In order to avoid unnecessary work, initial triplets are constructed only if at most one of its three wires is already assigned to an extending triplet.

Up to this point a wire may be associated with more than one track. In this case, the following procedure is used: Tracks sharing wires are sorted according to the number of associated wires. If there are two tracks with the same number of wires, the shared wires are assigned to the track with the best χ'^2. Multiply assigned wires are used only for the "best" track, they are discarded for the other tracks. This procedure is repeated until no questionable track with more than four hits is left.

Only after a track is completley reconstructed, the parameters ϕ_0 and d_0 are determined. Using the final curvature κ, the track projection, described as a circle, must match two pairs of points far from one another. From this last parametrization the quantities ϕ_0 and d_0 are determined. A cut on d_0 is used to accept or reject events. There must be at least two tracks with $d_0 < 1.5$ cm to accept an event.

6.1.3. The three-dimensional pattern recognition

After the completion of pattern recognition in the x–y-plane, the parameters z_0 and cot θ remain to be found. This is done by associating hit stereo wires with tracks in the x–y-plane.

The x–y pattern recognition constrains the track to the surface of a cylinder parallel to the z-axis. Again neglecting the drift times, the intersection points of a sequence of stereo wires with this cylinder define a sequence of z values. In the z–s-projection, where s is the distance along the track in the x–y-projection, measured from the reference point defined in section 6.1.1, these points form a straight line. This line, made up of at least three points, is reconstructed according to an algorithm similar to the one described above. When drift times are included, the left–right ambiguity is encountered again, and is removed in a manner similar to the previous case.

To accept an event the requirement is made that there must be at least two tracks with $z_0 < 8$ cm in addition to having $d_0 < 1.5$ cm, as mentioned above.

After the pattern recognition, all wires are uniquely assigned to tracks, or declared to be background. Approximate values for all five track parameters are determined. Their values are improved in a subsequent step, the track fit.

6.2. Track reconstruction

6.2.1. Least-squares fit

The purpose of the track fit is to find the set of track parameters $\boldsymbol{q}$ which minimizes the quadratic form

$$\chi^2 = (\boldsymbol{d}_{\text{meas}} - \boldsymbol{d}(\boldsymbol{q}))^{\mathrm{T}} \mathbf{W} (\boldsymbol{d}_{\text{meas}} - \boldsymbol{d}(\boldsymbol{q})), \tag{20}$$

where

$\boldsymbol{q}$ = 5-dimensional vector of track parameters as described in section 6.1.1,

$\boldsymbol{d}_{\text{meas}}$ = N-dimensional vector of measured drift distances (N wires hit),

$\boldsymbol{d}(\boldsymbol{q})$ = N-dimensional vector of distances of closest approach of a track to the hit wires, calculated for the track parameter set $\boldsymbol{q}$,

$\mathbf{W}$ = weight matrix, the inverse of the covariance matrix of the measured drift distances, $\mathbf{V}(\boldsymbol{d}_{\text{meas}})$

Since the drift distance measurements are independent, the $N \times N$ covariance matrix $\mathbf{V}(\boldsymbol{d}_{\text{meas}})$ has only diagonal elements σ_i^2, and eq. (20) results in the familiar expression

$$\chi^2 = \sum_{i=1}^{N} \frac{(d_{\text{meas},i} - d_i(\boldsymbol{q}))^2}{\sigma_i^2}. \tag{21}$$

Minimizing χ^2 as a function of $\boldsymbol{q}$ is equivalent to finding a solution of the system of equations

$$\frac{\partial \chi^2}{\partial q_\mu} = 0 \text{ for } \mu = 1, \ldots, 5. \tag{22}$$

If the vector $\boldsymbol{d}(\boldsymbol{q})$ depends linearly on the tracks parameters $\boldsymbol{q}$,

$$\boldsymbol{d}(\boldsymbol{q}) = \mathbf{A}\boldsymbol{q} + \boldsymbol{b} \text{ with } \mathbf{A} = (A_{i\mu})_{\substack{i=1,\ldots,N \\ \mu=1,\ldots,5}}, \tag{23}$$

eq. (22) yields a system of linear equations for the parameter vector $\boldsymbol{q}$:

$$\mathbf{A}^{\mathrm{T}}\mathbf{W}\mathbf{A}\boldsymbol{q} = \mathbf{A}^{\mathrm{T}}\mathbf{W}(\boldsymbol{d}_{\text{meas}} - \boldsymbol{b}). \tag{24}$$

From the covariance matrix transformation rule

$$\mathbf{V}(\boldsymbol{y}) = \mathbf{Z}\mathbf{V}(\boldsymbol{x})\mathbf{Z}^{\mathrm{T}} \text{ for } \boldsymbol{y} = \mathbf{Z}\boldsymbol{x} + \boldsymbol{c}, \tag{25}$$

with the replacements

$$\boldsymbol{x} \equiv \boldsymbol{d}_{\text{meas}},\ \mathbf{V}(\boldsymbol{x}) \equiv \mathbf{W}^{-1},$$

$$\boldsymbol{y} \equiv \boldsymbol{q},\ \mathbf{Z} \equiv (\mathbf{A}^{\mathrm{T}}\mathbf{W}\mathbf{A})^{-1}\mathbf{A}^{\mathrm{T}}\mathbf{W},$$

it follows that $(\mathbf{A}^{\mathrm{T}}\mathbf{W}\mathbf{A})^{-1}$ is the covariance matrix for the parameters $\boldsymbol{q}$.

In the case described here, the system of eqs. (22) is nonlinear because the function $\boldsymbol{d}(\boldsymbol{q})$ is nonlinear, and an iterative procedure has to be used to solve for $\boldsymbol{q}$. In order to linearize $\boldsymbol{d}(\boldsymbol{q})$ and to obtain the true solution $\boldsymbol{q}_{\mathrm{T}}$, the Taylor expansion around an approximate solution $\boldsymbol{q}_n$ is used. Neglecting higher order terms, one obtains

$$\begin{aligned} \boldsymbol{d}(\boldsymbol{q}_{\mathrm{T}}) &\approx \boldsymbol{d}(\boldsymbol{q}_n) + \sum_{\mu=1}^{5} \left.\frac{\partial \boldsymbol{d}}{\partial q_\mu}\right|_{\boldsymbol{q}=\boldsymbol{q}_n} (q_{\mathrm{T}} - q_n)_\mu \\ &= \mathbf{A}\boldsymbol{q}_{\mathrm{T}} + [\boldsymbol{d}(\boldsymbol{q}_n) - \mathbf{A}\boldsymbol{q}_n]. \end{aligned} \tag{26}$$

$\mathbf{A}$ is the Jacobian matrix of $\boldsymbol{d}(\boldsymbol{q})$ evaluated at $\boldsymbol{q} = \boldsymbol{q}_n$:

$$\mathbf{A} = \left.\frac{\partial \boldsymbol{d}}{\partial \boldsymbol{q}}\right|_{\boldsymbol{q}=\boldsymbol{q}_n} = (A_{i\mu}) = \left(\frac{\partial d_i}{\partial q_\mu}\right)_{\substack{i=1,\ldots,N \\ \mu=1,\ldots,5}}. \tag{27}$$

Eq. (26) is a linear equation of type (23) with $\boldsymbol{b} \equiv \boldsymbol{d}(\boldsymbol{q}_n) - \mathbf{A}\boldsymbol{q}_n$. Inserting eq. (26) into eq. (24) yields the linear system

$$\mathbf{A}^{\mathrm{T}}\mathbf{W}\mathbf{A}(\boldsymbol{q}_{\mathrm{T}} - \boldsymbol{q}_n) = \mathbf{A}^{\mathrm{T}}\mathbf{W}[\boldsymbol{d}_{\text{meas}} - \boldsymbol{d}(\boldsymbol{q}_n)], \tag{28}$$

which can be solved for the parameter correction $\Delta\boldsymbol{q} \equiv \boldsymbol{q}_{\mathrm{T}} - \boldsymbol{q}_n$. With this correction one gets a new approximation

$$\boldsymbol{q}_{n+1} = \boldsymbol{q}_n + \Delta\boldsymbol{q}. \tag{29}$$

Eqs. (28) and (29) define the iterative procedure. After a few iterations one usually obtains a solution close to $\boldsymbol{q}_{\mathrm{T}}$, provided one starts with a good first approximation $\boldsymbol{q}_0$. This is given by the pattern recognition procedure.

6.2.2. The particle trajectory

For the calculation of the distances of closest approach $\boldsymbol{d}(\boldsymbol{q})$ one needs an analytical expression for the trajectory of a charged particle moving in a magnetic field. First, we consider the case of a homogeneous magnetic field in the z-direction $\boldsymbol{H} = (0, 0, H)$ and assume that the track starts at

$$\boldsymbol{x}_0 = \begin{pmatrix} 0 \\ 0 \\ 0 \end{pmatrix},$$

with a momentum

$$\boldsymbol{p}_0 = p\boldsymbol{t}_0 = p \begin{pmatrix} 0 \\ \sin\theta \\ \cos\theta \end{pmatrix}, \tag{30}$$

where $\boldsymbol{t}_0$ denotes the initial tangent unit vector and θ is the polar angle with respect to the z-axis. The particle moves on a helix with its axis parallel to $\boldsymbol{H}$. As shown in fig. 47, the helix is conveniently parametrized by the turning angle Θ in the x–y-plane:

$$\boldsymbol{x}(\Theta) = \rho \begin{pmatrix} 1 - \cos\Theta \\ \sin\Theta \\ \Theta\cot\theta \end{pmatrix}. \tag{31}$$

The angle Θ is related to the track length s, which would be an equally good choice for the independent trace parameter:

$$\Theta = \frac{s\sin\theta}{\rho}. \tag{32}$$

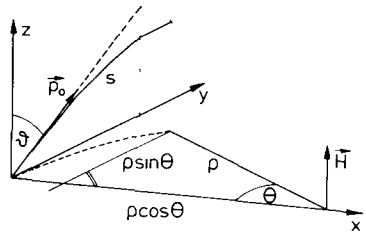

Fig. 47. Tracing step for the track fit.

The projection of the particle trajectory into the plane perpendicular to the field is a circle with radius

$$\rho = \frac{p \sin\theta}{QH} = \frac{p_T}{QH}, \tag{33}$$

where Q is the charge of the particle. In the ARGUS reconstruction program, the variable

$$K \equiv \frac{Q}{p_T} = \frac{1}{\rho H} \tag{34}$$

is generally preferred to ρ, because it is numerically better behaved. One should be aware of the slight differences in the definition of Q, ρ, and K as compared to the quantities Q, R, and κ which are used in the pattern recognition procedure (see section 6.1.1).

p, p_T, and H are treated as unsigned variables, whereas s, Q, ρ, K, and Θ have a sign. H can be considered as unsigned because the tracing procedure described in the next section uses a local coordinate system with its z-axis always pointing in the direction of $\boldsymbol{H}$. The step length s is positive if one steps in the direction of the particle's momentum $\boldsymbol{p} = p\boldsymbol{t}$, and negative otherwise. The sign of Θ follows from the sign of s by means of eq. (32). ρ and K have the sign of the particle's charge Q.

Differentiation of eq. (31) together with eq. (32) yields an expression for the track tangent as a function of s:

$$\frac{\mathrm{d}\boldsymbol{x}(s)}{\mathrm{d}s} = \boldsymbol{t}(s) = \sin\theta \begin{pmatrix} \sin\Theta \\ \cos\Theta \\ \cot\theta \end{pmatrix}. \tag{35}$$

6.2.3. Tracing in a varying field

For an arbitrary magnetic field $\boldsymbol{H}(\boldsymbol{x})$, the particle trajectory can be described by linked helical segments. This is done in the ARGUS track fit. A particle is traced from a point $\boldsymbol{x}_i$ with tangent vector $\boldsymbol{t}_i$ and magnetic field $\boldsymbol{H}(\boldsymbol{x}_i)$ to point $\boldsymbol{x}_{i+1}$ with tangent vector $\boldsymbol{t}_{i+1}$. If the distance between $\boldsymbol{x}_i$ and $\boldsymbol{x}_{i+1}$ is sufficiently small, the magnetic field in between can be assumed to be constant. In the ARGUS case, this condition is almost always fulfilled by tracing in steps from one hit wire to the next one. Only for low momentum tracks it may be necessary to use step sizes smaller than the distance between adjacent hit wires.

For the tracing procedure it is useful to define a local coordinate system which varies along the particle's trajectory. At the point $\boldsymbol{x}_i$ it is given by the following unit vectors:

$$\begin{aligned} \boldsymbol{h}_i &= \frac{\boldsymbol{H}(\boldsymbol{x}_i)}{|\boldsymbol{H}(\boldsymbol{x}_i)|}, \\ \boldsymbol{n}_i &= \frac{\boldsymbol{t}_i \times \boldsymbol{h}_i}{|\boldsymbol{t}_i \times \boldsymbol{h}_i|}, \\ \boldsymbol{b}_i &= \boldsymbol{h}_i \times \boldsymbol{n}_i. \end{aligned} \tag{36}$$

The ordered vector triplet $(\boldsymbol{n}_i, \boldsymbol{b}_i, \boldsymbol{h}_i)$ defines an orthonormal right-handed coordinate system. As shown in fig. 48, the orientations of the initial momentum and the magnetic field in this system satisfy the initial conditions (30). Hence one can immediately adopt the results (31) for the orbit and (35) for the track tangent. As a distinction from the fixed coordinate system, defined by the unit vector triplet $(\boldsymbol{e}_x, \boldsymbol{e}_y, \boldsymbol{e}_z)$, we do not use the polar angle θ with respect to the z-axis, but the dip angle λ, defined in the local system by

$$\sin\lambda_i = \boldsymbol{t}_i \cdot \boldsymbol{h}_i. \tag{37}$$

If, in the fixed system, $\boldsymbol{H}$ points in the z-direction, λ and θ are related by

$$\lambda = \frac{\pi}{2} - \theta. \tag{38}$$

For a tracing step from $\boldsymbol{x}_i$ to $\boldsymbol{x}_{i+1}$, the new point is obtained using eq. (31):

$$\begin{aligned} \boldsymbol{x}_{i+1} = \boldsymbol{x}_i + \rho\big[&(1 - \cos\Theta_i)\cdot\boldsymbol{n}_i + \sin\Theta_i \cdot \boldsymbol{b}_i \\ &+ \Theta_i \tan\lambda_i \cdot \boldsymbol{h}_i\big]. \end{aligned} \tag{39}$$

The new tangent direction is given by eq. (35):

$$\boldsymbol{t}_{i+1} = \cos\lambda_i(\sin\Theta_i \cdot \boldsymbol{n}_i + \cos\Theta_i \cdot \boldsymbol{b}_i + \tan\lambda_i \cdot \boldsymbol{h}_i). \tag{40}$$

Starting from a track point $\boldsymbol{x}_0$ with tangent $\boldsymbol{t}_0$, these formulae allow for the calculation of the particle trajectory in an arbitrary magnetic field. The point $\boldsymbol{x}_0$ is chosen to be the point of closest approach to the innermost hit wire. The accuracy of the method of linked helical segments depends on the step sizes $|\boldsymbol{x}_{i+1} - \boldsymbol{x}_i|$ and on the homogeneity of the field. Deviations from the true particle trajectory can easily be kept small compared to the spatial resolution of the drift chamber.

An approximate value for the step length s along the track between the points of closest approach to two

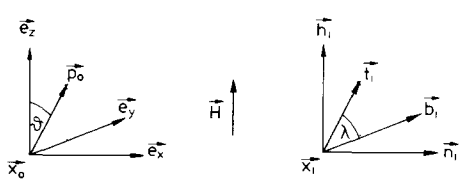

Fig. 48. Fixed and local coordinate system for the track fit.

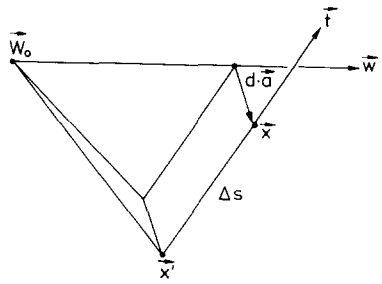

Fig. 49. Step length correction and distance of closest approach.

neighbouring hit wires is given by pattern recognition or by the previous fit iteration. For the current parameter set q_n, sometimes a correction Δs is necessary. The situation is described in fig. 49, where x' is the approximate point of closest approach, and x is the true point. W_0 is the wire coordinate in the plane $z = 0$ and w is the unit vector in the wire direction. Then the step length correction Δs is given by

$$\Delta s = \frac{(W_0 - x') \cdot (t - (w \cdot t) \cdot w)}{1 - (w \cdot t)^2}. \tag{41}$$

6.2.4. Distance of closest approach

The ultimate purpose of tracing is the determination of the distances of closest approach $d(q)$ of a track to the hit wires. As the track can pass on either side of a wire, the distance of closest approach d_i must be a signed quantity. The axis along which d_i is measured must have its origin at the position of the ith wire, and its direction defined by a unit vector perpendicular to w_i and t_i (see fig. 49):

$$a_i = \frac{w_i \times t_i}{|w_i \times t_i|}. \tag{42}$$

The distance of closest approach is given by the projection of $x_i - W_{0i}$ onto this axis (see fig. 49):

$$d_i = (x_i - W_{0i}) \cdot a_i. \tag{43}$$

The sign convention for d_i becomes clear in the view against w_i (see fig. 50). Following the particle along t_i, passing a wire on the left (right) side gives $d_i > 0$ ($d_i < 0$). The same signs must be applied to the measured drift distances.

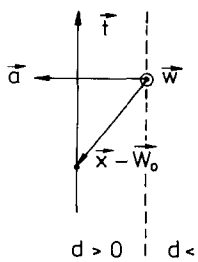

Fig. 50. Sign convention for the distance of closest approach.

6.2.5. Derivatives

As was shown in section 6.2.1, an iterative track fit requires the calculation of the derivatives $\partial d/\partial q$. Before discussing these it is useful to investigate how the relations derived in the local coordinate system transform to the fixed system.

The reference point x_0, the point of closest approach to the innermost hit wire, measured in the x–y-plane, is specified by two coordinates d_0 and z_0 (see section 6.1.1). The distance d_0 is measured in the x–y-plane along the axis defined by the unit vector

$$e_{xy} = \frac{e_z \times t_0}{|e_z \times t_0|}. \tag{44}$$

The distance z_0 is measured along the z-axis. The transformation of the local base vectors (36) at x_0 to the fixed system is as follows:

$$h_0 = e_z, \tag{45}$$

$$n_0 = \frac{t_0 \times h_0}{|t_0 \times h_0|} = -\frac{e_z \times t_0}{|e_z \times t_0|} = -e_{xy}, \tag{46}$$

$$b_0 = h_0 \times n_0 = e_{xy} \times e_z. \tag{47}$$

The local dip angle λ and the polar angle θ are related by eq. (38). The azimuthal angle ϕ_0 enters via the unit vectors b_0 and n_0:

$$b_0 = \begin{pmatrix} \cos\phi_0 \\ \sin\phi_0 \\ 0 \end{pmatrix}, \quad n_0 = \begin{pmatrix} \sin\phi_0 \\ -\cos\phi_0 \\ 0 \end{pmatrix}. \tag{48}$$

Expression (39) for an arbitrary track point x can now be rewritten to contain the track parameters d_0, z_0, K, cot θ, and ϕ_0:

$$\begin{aligned} x &= x_0 + \Delta x \\ &= d_0 e_{xy} + z_0 e_z \\ &\quad + \frac{1}{HK}\big[(\sin\Theta\cos\phi_0 + (1-\cos\Theta)\sin\phi_0)\cdot e_x \\ &\quad + (\sin\Theta\sin\phi_0 - (1-\cos\Theta)\cos\phi_0)\cdot e_y \\ &\quad + \Theta\cot\theta\cdot e_z\big]. \end{aligned} \tag{49}$$

For the calculation of the derivatives $\partial d/\partial q_\mu$ at any track point x one has to insert eq. (49) into eq. (43) and to differentiate with respect to all track parameters. This yields the following results:

$$\frac{\partial d}{\partial d_0} = e_{xy} \cdot a, \tag{50}$$

$$\frac{\partial d}{\partial z_0} = e_z \cdot a = a_z, \tag{51}$$

$$\frac{\partial d}{\partial K} = \frac{1}{K}(\boldsymbol{x}_0 - \boldsymbol{x}) \cdot \boldsymbol{a}, \tag{52}$$

$$\frac{\partial d}{\partial \cot \theta} = s \sin \theta \cdot a_z, \tag{53}$$

$$\frac{\partial d}{\partial \phi_0} = [(\boldsymbol{x} - \boldsymbol{x}_0) \times \boldsymbol{a}]_z. \tag{54}$$

6.2.6. The track fit procedure

The distances of closest approach (43) and the derivatives (50)–(54) are the necessary input for the iterative track fit, defined by eqs. (28) and (29). For the determination of the distances of closest approach the inhomogeneities of the magnetic field are fully taken into account. For the calculation of the derivatives it turns out that the assumption (45) of a homogeneous field along the z-axis is fully satisfactory. Using this approximation, the iterative track fit leads to the correct solution for the track parameters $\boldsymbol{q}$. The covariance matrix is affected at a level as large as the variation of the magnetic field along the particle trajectory, which is in the order of a few percent. Taking parts of the inhomogeneities into account also for the calculation of the derivatives, does not improve the results.

The whole fitting procedure consists of several passes in order to take more information into account and thus to improve the resolution. After the initial fit it is checked whether the χ^2 is improved by flipping the sign of the measured drift distance for any of the contributing wires. If no sign leads to a satisfactory χ^2, a wire is discarded. As the input from pattern recognition is already very reliable, this procedure causes only minor changes in the track parameters. An attempt is also made to assign new wires to the track which are not yet associated with another one. These steps are repeated after each of the following steps.

For a low momentum particle, the energy loss inside the drift chamber volume causes substantial deviations from the predicted trajectory. In order to take this effect into account, already at this stage the particle mass is determined in the $\mathrm{d}E/\mathrm{d}x$ part of the reconstruction program. The mass determination is sufficiently reliable for particles with high energy loss. After each tracing step (see section 6.2.3) the momentum loss corresponding to the track length is subtracted from the initial momentum.

Multiple scattering is taken into account by dividing the particle trajectory into segments, and allowing for kinks between any two consecutive segments. The segment length is determined by requiring that the expected spatial deviation due to multiple scattering inside a segment is small compared to the resolution of the drift chamber. In the ARGUS drift chamber it is sufficient to consider only the projections of the kink angles into the x–y-plane, δ_i. They are treated as additional parameters in the track fit. This is done by adding a term to the χ^2 (eq. (20)), which takes into account that the kink angles are expected to be small:

$$\chi^2 \to \chi^2 + \sum_i \frac{\delta_i^2}{\sigma_{\mathrm{MS},i}^2}, \tag{55}$$

with

$$\sigma_{\mathrm{MS}} = \frac{14.1\ \mathrm{MeV}/c}{p\beta} \sqrt{\frac{L}{L_{\mathrm{R}}}}. \tag{56}$$

L/L_{R} is the thickness of the traversed material in radiation lengths. Minimizing this kind of χ^2 provides a solution for the particle trajectory even for a large number of kink angles. For practical reasons this number is restricted to be smaller than the number of hit wires.

Finally, the whole procedure starting with the pattern recognition is repeated two times for those wires which were previously declared to be background, or which are assigned to short tracks or to tracks with large χ^2. With each repetition of this procedure, the requirements for accepting a track are more and more loosened.

After the track reconstruction in the main drift chamber has been completed, the tracks are traced back into the vertex drift chamber (VDC), and hits on these "roads" are assigned to the tracks. There is no attempt to find new tracks in the VDC because z-information is not available. Then a track fit is performed, using only the VDC hits, by minimizing the following χ^2:

$$\chi^2 = \sum_{\substack{i=1 \\ \mathrm{VDC}}}^{N} \frac{(d_{\mathrm{meas},i} - d_i(\boldsymbol{q}))^2}{\sigma_i^2} + (\boldsymbol{q} - \boldsymbol{q}_{\mathrm{DC}})^{\mathrm{T}} \mathbf{W}_{\mathrm{DC}} (\boldsymbol{q} - \boldsymbol{q}_{\mathrm{DC}}). \tag{57}$$

The second term contains the results from the track fit in the main drift chamber, the parameters $\boldsymbol{q}_{\mathrm{DC}}$ and the inverse covariance matrix $\mathbf{W}_{\mathrm{DC}}$. It imposes a constraint on the track fit in the VDC.

Pattern recognition and track fit in the main drift chamber are the by far most time consuming parts of the event reconstruction. For a randomly picked sample of 100 hadronic event candidates with a mean charged multiplicity of 6.7 the mean total reconstruction time on an IBM 3084 Q was 1.7 s/event. About 80% of this time was used for the track reconstruction in the main drift chamber, and another 10% for the track reconstruction in the VDC. The remaining 10% are enough for the vertex fit, TOF, shower counter, and muon chamber analysis to be performed.

6.3. Vertex reconstruction strategy

The vertex finding procedure used within the ARGUS reconstruction program is designed primarily

for quickly identifying possible interaction vertices and vertices of neutral decays that produce reconstructable tracks, both in the drift chamber and in the vertex drift chamber. Similar to the track fit, an iterative least squares fit procedure is used to find the coordinates of a vertex.

Prior to the vertex fit the tracks (i.e. parameters and errors) are extrapolated close to the beam line. The extrapolation of the parameters uses the same tracing formulae as the track fit, the only difference being that the tracing direction is now backwards, i.e. opposite to the particle's momentum. For the extrapolation of the covariance matrix the following formula is used:

$$\sigma(q'_\rho, q'_\sigma) = \sum_{\mu,\nu} \frac{\partial q'_\rho}{\partial q_\mu} \frac{\partial q'_\sigma}{\partial q_\nu} \sigma(q_\mu, q_\nu). \tag{58}$$

Errors due to Coulomb scattering from crossing the beam tube and the drift chamber wall are included where appropriate. For each track the parameter K (eq. (34)) is adjusted according to the mean value of the $\mathrm{d}E/\mathrm{d}x$ change across any boundaries which fall between the vertex point and the point in the drift chamber where the track parameters are defined. For this purpose, the mass of the particle associated with a track is chosen based on the drift chamber $\mathrm{d}E/\mathrm{d}x$ measurements, and if this is ambiguous, is taken to be the mass of the lightest hadron, from the set $\{\pi, \mathrm{K}, p\}$, for which the normalized likelihood exceeds 5% (see section 6.4.1).

The vertex fit procedure defines several variables. $d_{r,i}(\boldsymbol{v})$ is the perpendicular distance in the r–ϕ-plane from the trajectory of track i to the space point $\boldsymbol{v}$, the nominal vertex. Similarly, $d_{z,i}(\boldsymbol{v})$ is the z-distance from the same point of track i to $\boldsymbol{v}$. The covariance matrix for track i, at this point, can be calculated and then inverted to give the approximate weight matrix $\mathbf{W}_i(\boldsymbol{v})$.

For a track inclined at a polar angle θ in the vicinity of a nominal vertex $\boldsymbol{v}$, the minimum distance from the track to $\boldsymbol{v}$ is $d = \sqrt{d_r^2 + d_z^2/\sin^2\theta}$. It is not useful, however, to include this quantity into the χ^2 function to be minimized. The error on z is much larger than that on r, and so will be the dominant source of the error in d. Instead a column vector of distances $\boldsymbol{d}$, and an overall weight matrix $\mathbf{W}$, are defined to be

$$\boldsymbol{d} = \begin{pmatrix} d_{r,1} \\ d_{z,1} \\ \cdots \\ d_{r,n} \\ d_{z,n} \end{pmatrix},$$

$$\mathbf{W} = \begin{pmatrix} \mathbf{W}_1 & \cdots & 0 \\ \vdots & \ddots & \vdots \\ 0 & \cdots & \mathbf{W}_n \end{pmatrix}, \tag{59}$$

where n is the maximum number of tracks for a particular vertex. $\mathbf{W}_i$ denotes the 2×2 submatrix of the full weight matrix of track i, concerning the track parameters d_0 and z_0. The function to be minimized with respect to $\boldsymbol{v}$ is given by

$$\chi^2 = \boldsymbol{d}^{\mathrm{T}} \mathbf{W} \boldsymbol{d}. \tag{60}$$

The appropriate sum to be minimized could be formed by replacing $d_{z,i}$ by $d_{z,i}/\sin\theta_i$ and using the appropriate weight matrix in the above equation. However, the results are little different from the simpler case and this replacement is not used.

The χ^2 minimization is performed iteratively, using the same equations as developed for the track fit in section 6.2.1. The conditions for χ^2 to have a minimum are

$$\partial_{v_k} \chi^2 = 2(\partial_{v_k} \boldsymbol{d})^{\mathrm{T}} \mathbf{W} \boldsymbol{d} = 0 \quad k = \{x, y, z\}, \tag{61}$$

where ∂_{vk} denotes the partial derivative with respect to v_k. The $3 \times 2n$ matrix of derivatives is

$$\mathbf{A}^{\mathrm{T}} \equiv (\partial_{\boldsymbol{v}} \boldsymbol{d})^{\mathrm{T}} = \begin{pmatrix} \partial_{v_x} d_{r,1} & \partial_{v_x} d_{z,1} & \cdots & \partial_{v_x} d_{r,n} & \partial_{v_x} d_{z,n} \\ \partial_{v_y} d_{r,1} & \partial_{v_y} d_{z,1} & \cdots & \partial_{v_y} d_{r,n} & \partial_{v_y} d_{z,n} \\ \partial_{v_z} d_{r,1} & \partial_{v_z} d_{z,1} & \cdots & \partial_{v_z} d_{r,n} & \partial_{v_z} d_{z,n} \end{pmatrix}. \tag{62}$$

The expansion of $\boldsymbol{d}$ in a Taylor series about $\boldsymbol{v}$, close to the minimum, can be expressed as

$$\boldsymbol{d}(\boldsymbol{v}') = \boldsymbol{d}(\boldsymbol{v}) + \mathbf{A}(\boldsymbol{v}' - \boldsymbol{v}), \tag{63}$$

which yields the minimization equation

$$\mathbf{A}^{\mathrm{T}} \mathbf{W} [\boldsymbol{d}(\boldsymbol{v}) + \mathbf{A}(\boldsymbol{v}' - \boldsymbol{v})] = 0, \tag{64}$$

and the corrected value

$$\boldsymbol{v}' = -(\mathbf{A}^{\mathrm{T}} \mathbf{W} \mathbf{A})^{-1} \mathbf{A}^{\mathrm{T}} \mathbf{W} \boldsymbol{d}(\boldsymbol{v}) + \boldsymbol{v}, \tag{65}$$

which is used as vertex position in the next iteration. The quantities $\mathbf{A}(\boldsymbol{v})$, $\boldsymbol{d}(\boldsymbol{v})$, and $\mathbf{W}(\boldsymbol{v})$ are recalculated numerically for each newly iterated value of $\boldsymbol{v}$.

The iteration stops when the weighted change in the vertex position is smaller than some predetermined value. Using eq. (25) with

$$\boldsymbol{x} \equiv \boldsymbol{d}, \quad \mathbf{V}(\boldsymbol{x}) \equiv \mathbf{W}^{-1}, \quad \boldsymbol{y} \equiv \boldsymbol{v},$$

$$\mathbf{Z} \equiv (\mathbf{A}^{\mathrm{T}} \mathbf{W} \mathbf{A})^{-1} \mathbf{A}^{\mathrm{T}} \mathbf{W},$$

the covariance matrix for the vertex point $\boldsymbol{v}^*$ which minimizes χ^2 follows from equation (65):

$$\mathbf{V}(\boldsymbol{v}^*) = (\mathbf{A}^{\mathrm{T}} \mathbf{W} \mathbf{A})^{-1}. \tag{66}$$

Following convergence of the minimization procedure, the contribution of each track to the χ^2 is examined, and if no single contribution exceeds a predetermined value, which is itself determined from the data, the vertex $\boldsymbol{v}^*$ which minimizes χ^2 is retained. All track parameters are then recalculated with respect to this point. If the above condition is not met, the track

with the largest contribution is discarded, and the process is repeated until either the condition is met with a smaller number of tracks, or there are less than two tracks left.

Every track is considered for at least one vertex. To reduce computation time due to the large number of possible combinations, the sets of tracks to be tried are chosen in a manner consistent with the normal arrangement expected in a multihadron event. The first set of tracks are those which originate close to the beam interaction point. Following successful identification of this first vertex, which is normally the main vertex, all remaining unassociated track pairs are considered for separate vertices. This is first done in an approximate calculation in which both tracks are required to pass close to the same point. Then, they proceed through the same minimization procedure as is used for the main vertex. At this stage, the set of tracks proposed for a particular vertex always includes the original pair, plus any other unassociated tracks, which satisfy a loose cut on the minimum distance to the approximate value of the new vertex. Vertices in which the initial guess and the final value are widely separated can lead to a loss of those tracks which would have satisfied a loose cut based on the final value, but not on the initial one. On the other hand, inclusion of tracks which are too distant degrades the performance of the minimization procedure, therefore these cuts are a compromise.

Finally, a last pass is made over all pairs of tracks in order to improve the efficiency for identifying potential K_S^0 and Λ vertices. An extra condition is applied in that no track may already belong to the same vertex as its partner. This procedure was found to be necessary because of the relatively high probability that one track from a secondary vertex was lost due to its association with the main vertex. For two prong secondary vertices charge balance is required. In order to further reduce the combinatorial background, a loose cut is applied on the transverse momentum with respect to the momentum of the neutral. This requirement is chosen so as not to affect the K_S^0 or Λ acceptance.

6.4. Particle identification strategy

ARGUS provides two independent methods for charged particle identification, namely, the measurement of the specific energy loss due to ionization in the drift chamber gas, and the measurement of the time-of-flight which, together with the information on momentum from the drift chamber, allows the reconstruction of a particle's mass. Details of these measurements have been discussed in section 3.3.6 and 3.5.5.

There are, in addition, independent methods for lepton identification. Electrons can be detected in the electromagnetic calorimeter (see section 3.6.5), and muons, with momenta greater than the cutoff momentum of 700 MeV/c, hit the muon chamber system surrounding the detector (see section 3.7).

In addition, the shower counters can be used to identify charged antibaryons by the observation of their enormous energy deposit produced by the strong annihilation process. This helps in unambiguously tagging rare particles such as antideuterons [31].

6.4.1. Charged particle identification with dE/dx and TOF

The specific ionization loss of a charged particle in a given medium depends entirely on its velocity. In combination with the information regarding its momentum, supplied by the track reconstruction, the measurement of its specific ionization loss allows for the identification of the particle by its rest mass. The procedure applied in the ARGUS reconstruction software compares a particle's dE/dx measured in the drift chamber, with the dE/dx values theoretically expected for electrons, muons, pions, kaons, and protons. Formally, this comparison results in a χ^2 for each particle hypothesis:

$$\chi_i^2(dE/dx) = \frac{\left(dE/dx - dE/dx_i^{\text{th}}\right)^2}{\sigma_{dE/dx}^2 + \sigma_{\text{th}}^2}$$

$$(i = e, \mu, \pi, K, p). \tag{67}$$

Here dE/dx is the measured specific ionization loss, and dE/dx_i^{th} is the specific ionization loss expected theoretically for the ith particle hypothesis. σ_{th} is the uncertainty of the theoretical dE/dx value introduced by the momentum uncertainty, and $\sigma_{dE/dx}$ the uncertainty of the specific ionization measurement. Details on the theoretical parametrization of the dE/dx curve, and on the determination of the experimentally observed ionization loss can be found in ref. [32].

A similar procedure is used for the TOF information by comparing the measured velocity with that expected for the above mentioned particle hypotheses. This results in a χ^2 of the form

$$\chi_i^2(\text{TOF}) = \frac{\left(1/\beta - 1/\beta_i^{\text{th}}\right)^2}{\sigma_{\text{TOF}}^2 + \sigma_{\text{th}}^2}, \tag{68}$$

where β is the particle's velocity measured by the time-of-flight system, β_i^{th} is the velocity expected for the ith particle hypothesis calculated from the momentum, and σ_{TOF} and σ_{th} are the uncertainties of the measured and expected velocities, the latter also coming from the momentum uncertainty.

Since dE/dx and TOF measurements are independent, the two χ^2's can be added to give a single charged particle identification χ^2

$$\chi_i^2 = \chi_i^2(dE/dx) + \chi_i^2(\text{TOF}), \tag{69}$$

which in turn can be used to form a likelihood function

$$L_\iota = \exp\left(-\chi_\iota^2/2\right), \tag{70}$$

where the index ι again runs over the five particle hypotheses considered. From the likelihood functions normalized likelihoods λ_ι are constructed

$$\lambda_\iota = \frac{w^\iota L_\iota}{\sum_{k=e,\mu,\pi,K,p} w^k L_k}. \tag{71}$$

The w^ι are relative production rates introduced from an a priori knowledge of the particle abundances. Because the χ^2's are supplied with every track on the data summary tapes, the user can define the criteria for accepting or rejecting a certain particle hypothesis. Roughly 80% of all measured charged particles can be uniquely identified by the dE/dx and TOF measurements.

6.4.2. Electron identification

Electrons are identified by the independent means of dE/dx and TOF measurements, and by using shower counter information. None of these components, however, is capable of providing particle identification over the entire momentum range of interest. In a diagram of dE/dx vs momentum (see fig. 13), the curves for muons, pions, kaons, and protons all eventually cross the electron curve, and for higher momenta all the curves approach the electron line. The TOF separation, on the other hand, is based on particles' different velocities. Electrons, being already highly relativistic at low momenta, can be separated from muons and pions only up to approximately 230 MeV/c. A wider range is finally offered by the electromagnetic calorimeter. An electron separation based on the shower counters alone is described in ref. [23].

It is therefore desirable to combine all available information about electrons into a universal likelihood function similar to that described above for hadrons using dE/dx and TOF. It is described in detail in ref. [33]. The normalized likelihood has the form

$$\lambda^e = \frac{w^e \prod_{\iota=dE/dx,TOF,SC} p_\iota^e(x)}{\sum_{k=e,\mu,\pi,K,p} w^k \prod_{\iota=dE/dx,TOF,SC} p_\iota^k(x)}, \tag{72}$$

where $p_i^k(x)$ are the probabilities for a track with measured parameters x to be identified as particle type k by device i, and the w^k are again relative production rates derived from an a priori knowledge of the particle abundances. The electron hypothesis is accepted if λ^e exceeds some specific value. A single cut in this multidimensional space achieves an electron selection efficiency well above 90% for all momenta above 0.5 GeV/c, with a hadron rejection of better than 1 : 200.

It should be noted that the method of normalized likelihoods is superior to any application of cuts in the variables on which the likelihood function depends.

6.4.3. Muon identification

A similar procedure is applied for muon identification. Here, a condition to be met is that tracks reconstructed in the drift chamber can be traced through the electromagnetic calorimeter, magnet coils and iron yoke and can be assigned to hits in the muon chambers. During tracking, multiple Coulomb scattering, magnetic field, and energy loss are taken into account. After successful tracking, another likelihood function is formed based on information from dE/dx, TOF, shower counters, and the muon chambers. The latter takes into account the information from three layers of muon chambers, including the number of hits associated with the track, the distance between the calculated position of the track impact point and the closest hit, and the resulting χ^2, and the probability for a hit assuming the muon hypothesis. The normalized likelihood then reads

$$\lambda^\mu = \frac{w^\mu \prod_{\iota=dE/dx,TOF,SC,\mu} p_\iota^\mu(x)}{\sum_{k=\mu,\pi,K,p} w^k \prod_{\iota=dE/dx,TOF,SC,\mu} p_\iota^k(x)}, \tag{73}$$

with the symbols defined similarly to those in eq. (72).

The lepton–hadron misidentification probabilities were determined using data samples of $\tau^- \to \nu_\tau \pi^+ \pi^- \pi^- + n\pi^0$ ($n = 0, 1$) and $D^{*+} \to D^0 \pi^+$, $D^0 \to K^- \pi^+$ decays which provide clean sources of high energy pions and kaons. Decay-in-flight and punchthrough together result in a μ–π misidentification probability of $(2.2 \pm 0.2)\%$ per pion. For μ–K misidentification the fake rate is $(1.9 \pm 0.5)\%$ per kaon. The fake rates due to e–π and e–K misidentification are both $(0.5 \pm 0.1)\%$. The lepton–hadron misidentification rates have also been determined using hadronic decays of the $\Upsilon(1S)$ where the number of leptons produced is negligible. The results obtained agree well with the quoted values.

6.5. The ARGUS detector simulation strategy

The program for the detector simulation is built upon the program GEANT [34] which constitutes a general framework for handling geometry and tracking. The details of the tracking as well as the physical processes that take place when particles interact with various detector media, must be supplied by the user. Details of the ARGUS simulation program, SIMARG, can be found in ref. [35].

The essential steps of the full simulation are:

(1) Generate an event.

(2) (a) Fill the particle stack with the the generated particles (tracks).

(b) Track each particle through the detector and record eventual energy deposit in the TOF and shower counters as well as coordinates along the track.
(c) Use the track coordinates to determine the intersection of the particle trajectories with various detector components and store the resulting points.
(d) Calculate, from the intersection points, which wires have been hit in the vertex chamber, drift chamber, and the muon chambers.
(e) Create an event record with the same format as a real data record.

(3) Process the event through the normal reconstruction program, applying efficiencies and smearing according to the resolution of the various detector components.

SIMARG comprises point (2) above, although some simple event generators can also be linked with the program. At initialization, SIMARG reads a so-called "title file" containing the specification of the geometry of the different detector components. General constants as well as a description of the chemical composition of the different parts of the detector are contained in FORTRAN BLOCK DATA statements. The latter constants are used to calculate the macroscopic cross sections for the relevant physical processes.

The physical processes modelled in this simulation consist of electromagnetic and hadronic interactions. The treatment of the former follows closely the procedure of the EGS program [36] although parts of it follow other prescriptions such as the Migdal treatment of bremsstrahlung according to Messel and Crawford [37]. The energy cutoffs upon which tracking ends are 1.5 MeV for electrons/positrons and 0.8 MeV for photons. This is quite sufficient to give a small error ($< 1\%$) on the simulated energy deposit in the shower counters.

The simulation of hadronic processes is performed by routines from the program GHEISHA [38] which is linked as a callable package. GHEISHA is only used to generate hadronic interactions while its tracking part has been suppressed. Whenever new particles are generated (as a result of an interaction, decay etc.), they are appended to the SIMARG particle stack, and the last one generated will be the next one to be tracked.

In all, this means that electromagnetic and hadronic showers are fully simulated. Some speed could have been gained by using a set of prefabricated showers. Due to leakage, especially at the edges of the shower counters, as well as to backscattering into the TOF system, the latter procedure was abandoned. Showers are also allowed to develop in the chamber walls and in other materials in the central part of the detector (as well as in the regions in front of the muon chambers). In regions of no interest, tracking is stopped if the particle is unlikely to reach any of the active detector components (punch through into the muon chambers is still allowed for). To further speed up the development of showers inside the shower counters, an analytic tracking method is used, see ref. [36] for details.

For the drift chamber a separate $\mathrm{d}E/\mathrm{d}x$ simulation is made (the energy loss employed during tracking cannot be used since the length of a track in a given cell is not known at that stage). It uses energy loss spectra measured in a smaller test prototype of the real chamber. This makes the simulation independent of theoretical models for the energy loss spectrum, and is necessary to give a proper simulation of the effects of selection criteria based on the $\mathrm{d}E/\mathrm{d}x$ information and applied at the analysis stage. The $\mathrm{d}E/\mathrm{d}x$ values are finally converted into ADC channels, and ADC thresholds are applied at the reconstruction stage as for real data.

During tracking, continuous energy loss of particles is randomized according to a truncated Landau distribution (with width depending on step length as was done by Rossi [11]), plus δ-electron generation for hadrons (energy transfer larger than 1 MeV). For electrons and positrons elastic scattering processes with energy transfers smaller than 0.225 MeV are included in the continuous energy loss.

For unstable particles, a decay length is generated at the time it is filled into the particle stack. This decay length is continuously updated during tracking, and account is taken of the effects of energy loss on this length. When the decay length becomes zero, the particle is allowed to decay according to a randomly chosen decay mode, a list of which is provided for the most common particles in the title file.

The simulation of drift times in the chambers is made according to measured drift time–space relations, and the final result is given in TDC units. For a given track, the closest distance to each wire is calculated using the results of step (2(c)) and then turned into the corresponding drift time.

The information written to disk or tape not only contains the simulated "raw" data but also information on the generated tracks. Some of the items stored are: A list of wires hit by the track as well as information on shower counters hit, energy deposit in relevant detector modules etc. This information is very useful in testing the reconstruction program, testing algorithms for track selection etc. This is also true for testing the simulation program itself. The program has been thoroughly tested and compared to real data. No significant discrepancies have been found. As an example, the proper matching of reconstructed and generated tracks has been studied for charged kaons from φ meson decays [30]. The matching probability was found to be $(99.6 \pm 0.1)\%$ in this case.

6.6. The simulation of the ARGUS trigger

Accurate simulation of the trigger is essential for analysis of events with low multiplicity, asymmetric topology, or low visible energy. Examples are τ-pair production and two photon collisions. A program, TRIGGR, has been developed which processes the reconstructed SIMARG output and simulates the ARGUS trigger.

The ARGUS experimental history is divided into trigger periods with different thresholds, logics, and LTF efficiencies. Initially, TRIGGR calculates the luminosity for each of these periods, given user specified requirements on the data quality, centre-of-mass energy and trigger restrictions. In the next step, which is repeated for each Monte Carlo event, the shower counter pulse heights are summed for each trigger element, and the LTF masks are determined from the drift chamber TDC hits. As the LTF algorithm is time consuming this step if often run independently and saved for input to TRIGGR.

Next, TRIGGR loops over all trigger periods, determining which triggers are set in each. To minimize fluctuations, this step is repeated several times and the average fraction of luminosity in those periods with a trigger set is used as an event weight. TRIGGR can also be instructed to return a weight equal to the number of events expected from a theoretical cross section supplied by the user. In this mode each trigger period's contribution to the event weight can be scaled to adjust for the center-of-mass energy dependence of the cross section and the distribution of center-of-mass energies of each trigger period.

The integrated pulse height seen by a trigger element in Monte Carlo is proportional to the deposited energy. Experimentally, the pulse height seen by a discriminator is distorted by single counter variations of photomultiplier amplification, light guide transfer functions, and pedestal subtractions. The effect is to distort the shape of the trigger thresholds, in terms of real deposited energy, away from a step function. The shower fluctuations add to the distortion as the discriminators operate on the instantaneous pulse amplitude while deposited energy depends on the time integral of the pulse.

The trigger thresholds were determined from experimental data from each trigger period and type by using the trigger information and calibrated pulse heights. Minimum bias data were used, for example the CPPT thresholds were determined from all events with an ETOT trigger set. A smearing of about 2% is introduced in the derived threshold shapes as the deposited energy cannot be determined exactly. As the incident energy distributions are steeply decreasing, a shift in the position of the threshold of the same order is expected. This effect is not of the same magnitude as the shower counter resolution as it is only that portion introduced by calibration that is relevant, the effects of sampling, structure, and leakage are simulated by SIMARG when it calculates the deposited energy.

For dimuon events from the data the measured thresholds imply a CPPT element efficiency of about 95%. This agrees to within 1% with the results of the trigger simulation program using Monte Carlo μ-pairs. The systematic error on the trigger efficiency is estimated conservatively by shifting all thresholds in each trigger period simultaneously by $\pm 10\%$. For two photon collisions this translates into a systematic error from the pretrigger of about 4%.

The LTF efficiency is defined as the probability for a charged particle to be assigned one or more LTF tracks if it hits a TOF counter. This was determined from Bhabha scattering events with the ETOT trigger set (which does not require a LTF signal). The Monte Carlo SIMARG events are reconstructed with a fixed average drift chamber cell efficiency, as small variations in this efficiency do not influence the track finding efficiency. The LTF mask finding algorithm uses a drift chamber efficiency of 100% which is corrected in TRIGGR by discarding masks randomly to get the experimentally observed LTF efficiency. There is some particle type and azimuthal angle dependence of the LTF efficiency which is at present ignored in the simulation, but is included in the systematic error estimate.

The LTF efficiency is overestimated for particles with low transverse momenta because of extra hits in the drift chamber produced by SIMARG. To correct for this, a separate simplified simulation is done assigning a maximum of one LTF track per particle, which underestimates the LTF efficiency. The average of the two results is used as the efficiency and the difference as the systematic error. This error is 15% at the geometric limit of transverse momenta of 125 MeV/c. It decreases rapidly with increasing transverse momenta and reaches 3% at 300 MeV/c. As examples, the systematic errors for the two photon collisions with the final states $\pi^+\pi^-\gamma$ and $2\pi^+2\pi^-\pi^0$ are 7% and 5%, respectively.

The TRIGGR simulated efficiencies have been compared with trigger efficiencies deduced directly from the data. An example is the transition $\Upsilon(2S) \to \Upsilon(1S)\pi^+\pi^-$ followed by $\Upsilon(1S) \to e^+e^-$. Here events were selected where the electron or positron had set the ETOT trigger. The fraction of those events where the pions alone had also set a trigger was found and compared with Monte Carlo generated events of the same transition but where $\Upsilon(1S)$ decays to noninteracting particles. The two trigger efficiencies were identical.

7. Summary

During its first four years of operation, ARGUS has proven to be a reliable detector deserving the name

"universal". The solid angle coverage for charged and neutral particle detection is close to 4π. The charged track reconstruction efficiency and the momentum resolution, as well as the energy resolution of electromagnetically showering particles are all very good. Muons

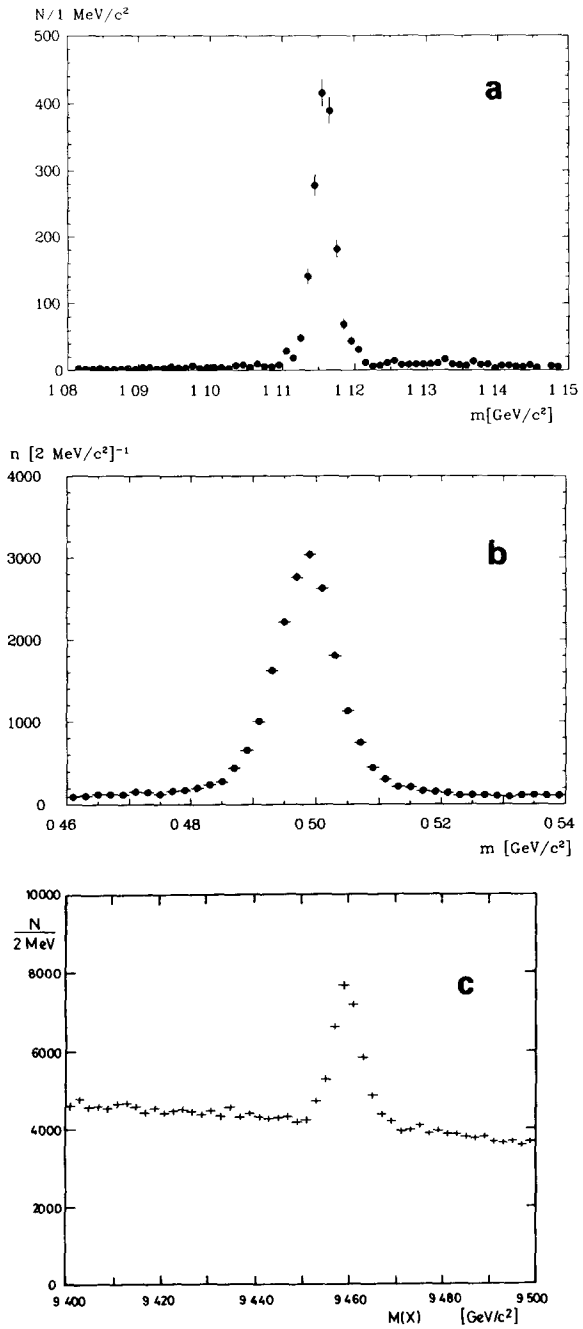

Fig. 51. Invariant mass spectra for (a) Λ particles, (b) K^0_S particles, (c) $\Upsilon(1S)$ in the process $\Upsilon(2S) \to \Upsilon(1S)\pi^+\pi^-$.

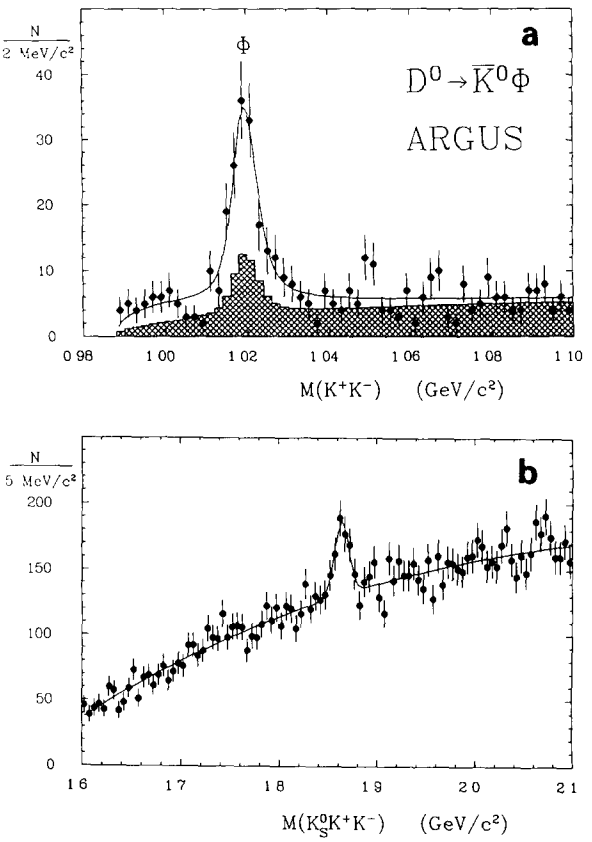

Fig. 52. Invariant mass spectra in the decay $D^0 \to \overline{K}^0_s\phi$: (a) ϕ mass, (b) D^0 mass.

traversing the iron yoke are detected with good efficiency over a large fraction of the full solid angle.

The coherent use of the information from all detector components results in the detector's main virtue, its excellent particle identification capability for both charged hadrons and leptons. This high separating power is the main ingredient of the physics results obtained up to now. We conclude this paper by indicating how the performance of the detector components shows up in selected recent physics results.

The track and vertex finding capability of the main and vertex drift chambers determines the detection efficiency for Λ and K^0_S particles, while the achieved momentum resolution is reflected in their invariant mass resolution. Another example of the good mass resolution is the distribution of the $\Upsilon(1S)$ mass, reconstructed from the decay

$$\Upsilon(2S) \to \Upsilon(1S)\pi^+\pi^-,$$

where the $\Upsilon(1S)$ mass is calculated from the beam energy and the pion four-momenta [40]. The mass spectra for Λ, K^0_S, and $\Upsilon(1S)$ are shown in fig. 51.

Good particle identification, as supplied by dE/dx and TOF measurements, allows for the reconstruction

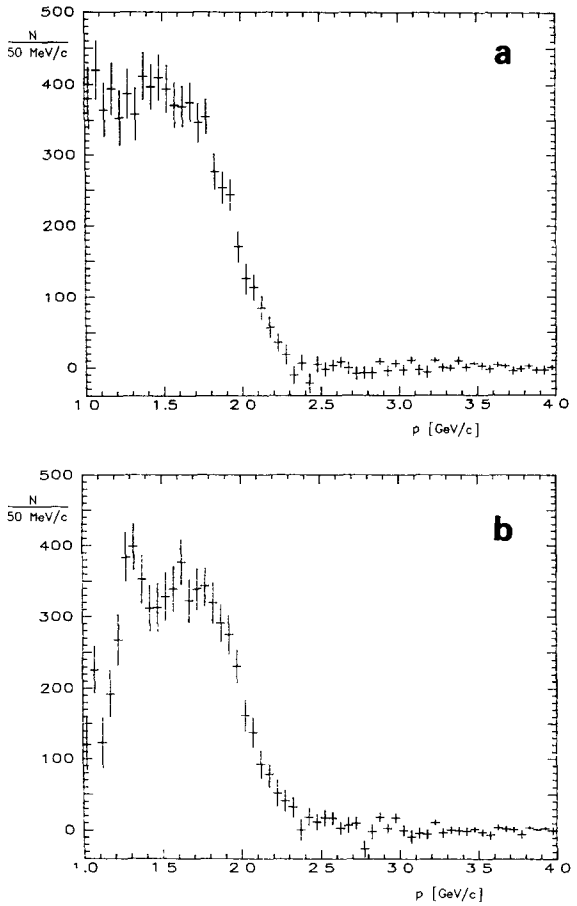

Fig. 53. Lepton momentum spectra from B^0 decays. (a) Electrons, (b) muons.

of the decays of charmed particles with low combinatorial background. An illustrative example is the decay $D^0 \to \overline{K}{}^0_S \phi$ where a neutral kaon has to be reconstructed from its decay pions, and a ϕ from identified charged kaons [41]. The D^0 signal as well as the overall ϕ signal is shown in fig. 52. Another example is the detection of antideuterons in hadronic events, using the combined information of dE/dx, TOF, and shower counters [31].

The good photon energy re of the electromagnetic calorimeter shows up in the mass distribution of η mesons, reconstructed from two photons detected in the calorimeter [42] (see fig. 26).

Finally, we mention the result on $B^0 - \overline{B}{}^0$ mixing which essentially relies on good lepton identification over a wide momentum range [43]. Lepton identification involves all active components of the detector. The lepton momentum spectra from B^0 decays are shown in fig. 53.

In summary, the design of ARGUS described in the proposal [1] has been successfully converted into a working detector. All components have achieved the conceptual design specifications and some have even surpassed them.

Acknowledgements

The construction and running of ARGUS would have been impossible without the cooperation and support from various sides. The collaboration would like to thank all engineers and technicians in the mechanical and electronic workshop at their institutions, for their enthusiasm in constructing a new detector. Particular gratitude is expressed to:

- G. Bialek, F. Hübler, V. Nedič, R. Pforte, E. Schuld, M. Swars and K. Valett from DESY-F51 for substantial contributions to the detector electronics and the static monitoring system;
- U. Dretzler, G. Ernst, H.J. Gerwing, H. Höper, G. Metze and K. Schmitz from Universität Dortmund;
- J. Heyde, J. Krause and the late Dr. M. Vysočanský from Universität Heidelberg for many contributions to the TOF high voltage and data acquisition systems;
- Yu. Gorodkov, G. Divulskij and A. Mileshkin from ITEP, Moscow;
- A.A. Raffler and A. Peter (Carleton University, Ottawa), A. Kiang and T. Wenaus (University of Toronto), and F. Jarvis (University of York) for many contributions during design and construction of the vertex drift chamber.

The collaboration would like to thank Dr. F. Schwickert and the DESY Hallendienst for their support in the construction phase of ARGUS, and Dr. H. Nesemann, B. Sarau, Dr. K. Wille and the DORIS machine group for their cooperation and constant effort to optimize the running conditions.

The collaboration is deeply indebted to the DESY directorate for their constant encouragement and support, and the hospitality extended to the outside groups.

References

[1] H. Hasemann et al., DESY Internal Report F15/Pro 148 (October 1978).
[2] H. Nesemann and K. Wille, IEEE Trans. Nucl. Sci. NS-30 (1983) 1998.
[3] R.L. Childers and Y. Oku, DESY Internal Report F15-83-01 (August 1983).
[4] M. Danilov et al., Nucl. Instr. and Meth. 217 (1983) 153.
[5] H. Hasemann, Proc. Int. Conf. on Instrumentation for Colliding Beam Physics, Stanford (1982) SLAC-250, p. 80.
[6] L. Malter, Phys. Rev. 50 (1936) 48.
[7] C.W. Hast, Diplomarbeit, Dortmund University (1988).
[8] M. Danilov et al., Nucl. Instr. and Meth. A274 (1989) 189.
[9] G. Harder, Diplomarbeit, DESY Internal Report F15-84/01 (November 1984).

[10] R.L. Gluckstern, Nucl. Instr. and Meth. 24 (1963) 381.
[11] B. Rossi, High Energy Particles (Prentice-Hall, 1952) section 23.
[12] R.M. Sternheimer and R.F. Peierls, Phys. Rev. B3 (1971) 3681.
[13] K.W. Edwards et al., Nucl. Instr. and Meth. A252 (1986) 384.
[14] J.C. Yun, M. Sc. Thesis, Carleton University, Ottawa (1984)
[15] B.P. Padley, Ph. D. Thesis, University of Toronto (1987); H. Albrecht et al., Phys. Lett. B199 (1987) 580.
[16] R. Heller et al., Nucl. Instr. and Meth. A235 (1985) 26.
[17] Th. Massam, Nucl. Instr. and Meth. 141 (1977) 251.
[18] W. Braunschweig et al., Nucl. Instr. and Meth. 134 (1976) 261.
[19] R. Heller, N. Kwak, K.R. Schubert, J. Stiewe and R. Waldi, Proc. 3rd Int. Conf. on Instrumentation for Colliding Beam Physics, Novosibirsk (1984) p. 153.
[20] R. Salomon, Diplomarbeit, Heidelberg University IHEP-HD/83-3 (May 1983)
[21] A. Drescher et al., Nucl. Instr. and Meth. 205 (1983) 125.
[22] A. Drescher et al., Nucl. Instr. and Meth. 216 (1983) 35.
[23] A. Drescher et al., Nucl. Instr. and Meth. A237 (1985) 464.
[24] A. Drescher et al., Nucl. Instr. and Meth. A249 (1986) 277.
[25] U. Kaiser, Diplomarbeit, Dortmund University (1986).
[26] M. Dvorak, Diplomarbeit, Dortmund University (1986).
[27] A. Arefiev et al., DESY 83-025 and Instr. Exp. Tech. 29 (1986) 333
[28] H.D. Schulz and H.J. Stuckenberg, Proc. Topical Conf. on the Application of Microprocessors in High Energy Physics Experiments, CERN, Geneva (1981) CERN 81-07, p. 194.
[29] F.A. Berends et al., Nucl. Phys B68 (1974) 541, B228 (1983) 537;
R. Kleiss, Ph. D. Thesis, Leiden University (1982).
[30] G. Braunshausen, Dipolomarbeit, Heidelberg University IHEP-HD/84-05 (April 1984).
[31] H. Albrecht et al., Phys. Lett. B157 (1985) 326.
[32] Y. Oku, Ph. D Thesis, Lund University LUNFD6/(NFFL-7024) (1985).
[33] S. Weseler, Dissertation, Heidelberg University IHEP-HD/86-2 (April 1986).
[34] R. Brun et al, CERN-DD/78/2 (1978).
[35] H. Gennow, DESY Internal Report F15-85-02 (August 1985).
[36] R.L. Ford and W.R. Nelson, The EGS Code System, Version 3, SLAC-210, UC-32 (1978).
[37] H. Messel and D.F. Crawford, Electron-Photon Shower Distribution Functions (Pergamon, Oxford, 1970).
[38] H. Fesefeldt, RWTH Aachen Report PITHA 85/02 (1985).
[39] U. Matthiesen, Dissertation, Dortmund University (1987).
[40] H. Albrecht et al., Phys. Lett. B134 (1984) 137.
[41] H. Albrecht et al., Z. Phys. C33 (1987) 359.
[42] A. Drescher, Dissertation, Dortmund University (1987).
[43] H Albrecht et al., Phys. Lett. B192 (1987) 245.